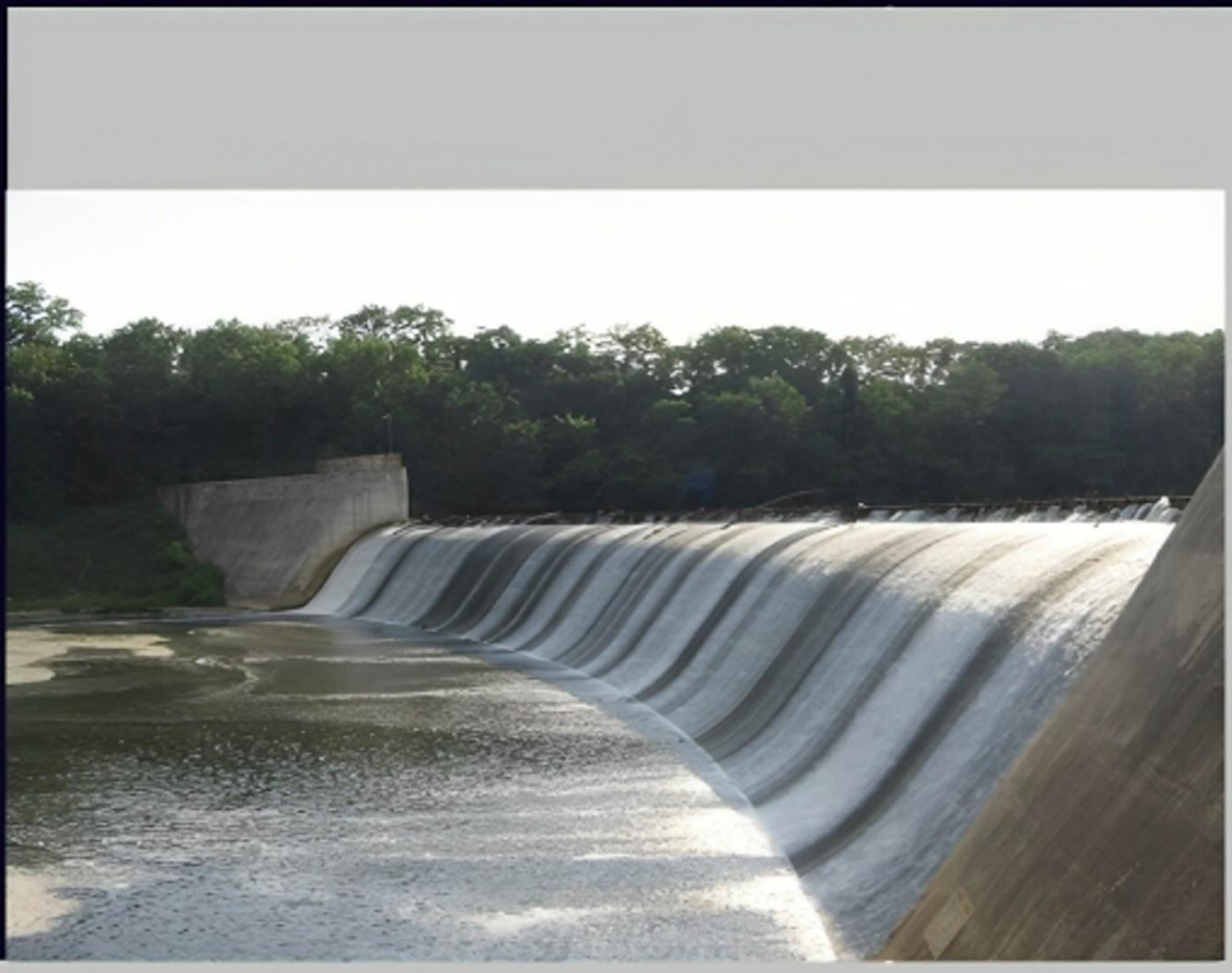
Iranian Hydraulic Association

Shahid Chamran University of Ahvaz

Journal of Hydraulic Structures

Scientific Professional Journal



January 2025
Volume 11, Issue 1

ISSN (Online): 2345-4156
https://jhs.scu.ac.ir/

Aims and Scope

Journal of Hydraulic Structures is an interdisciplinary journal which publishes high-quality peer-reviewed articles addressing the latest developments and applied methods in analysis and design, construction, maintenance, management, and operation policy of Hydraulic Structures.

The Journal aims at providing an efficient route to fast-track publication, within 10-12 weeks after manuscript submission.

The general areas covered by the Journal include:

- Advances in numerical and analytical methods applicable to hydraulic structures
- Hydro informatics and soft computing
- Hydraulic aspects of hydraulic structures
- Applied surface and subsurface hydrology and hydrometeorology
- Forecasting approaches in water resources engineering
- Economic and social aspects of hydraulic structures
- Uncertainty analysis and risk management in hydraulics and water resources engineering
- Application of Nanotechnology in hydraulic structures
- Geotechnics of hydraulic structures
- Damage detection techniques
- Technical and methodological advances in application, design/selection, production, construction materials of hydraulic structures.
- Application of Artificial Intelligence techniques in all aspects of hydraulic structures.

General Information:

Title: Journal of Hydraulic Structures

Publisher: Shahid Chamran University of Ahvaz

ISSN (Print): 2345-413X

ISSN (Online): 2345-4156

Website: https://jhs.scu.ac.ir/

Address: Faculty of Civil Engineering and Architecture, Shahid Chamran University of Ahvaz, Ahvaz, Iran

Email: jhs@scu.ac.ir

Journal of

Hydraulic Structures

Shahid Chamran University of Ahvaz

Director-in-Charge: Prof. Ali Haghighi

Editor-in-Chief: Prof. Hamid R. Ghafouri

Managing Editor: Dr. Amir H. Shafiee

Contents:

01

Optimizing the urban runoff collecting network using Harris Hawks single-objective optimization algorithm (a case study of the flood network in West Tehran)

Seyed Masoud Majidi; Hamed Reza Zarif Sanayei; Ali Raeisi Isa-Abadi

20

Enhancing the seismic performance of platforms in intermediate water depth using shape memory alloy dampers

Mohammad Jafari; Hamid Bayesteh; Reza Rasti Ardakani

41

Spiral Flow Measurement at Vertical Intakes Using PTV Method

ShahWali Hamidi; Hamed Sarkardeh; Ali Bashtani

51

Dimensionless Equations for Hydraulic Jump Stilling Basins Downstream of Gabion Stepped Chutes

André Luiz Andrade Simões; Thaise Ithana de Souza França; Luciano Matos Queiroz; Iran Eduardo Lima Neto; Harry Edmar Schulz; Daniel Castro Hora Fontes; Rodrigo de Melo Porto

65

Numerical Study of Permanent Deformations of Embankment dams under Seismic Loading, A case study of Kheyrabad Dam

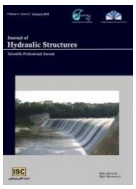
Masoud Oulapour; Hossein Samani; Mohammad Amjadzadeh

89

Integrating Fuzzy Logic and Numerical Modeling for Analyzing Wave Patterns: A Study of the Makran Coastline

Maryam Rahbani; Danial Ghaderi

Journal of Hydraulic Structures
J. Hydraul. Struct., 2025;11(1):1-19
DOI: 10.22055/jhs.2024.47664.1317



OPEN ACCESS

Optimizing the urban runoff collecting network using Harris Hawks single-objective optimization algorithm (a case study of the flood network in West Tehran)

Seyed Masoud Majidi [1]
Hamed Reza Zarif Sanayei [*1]
Ali Raeisi Isa-Abadi [2]

Abstract

Today, optimization is very important and necessary in engineering works and it seems necessary in the field of urban runoff and flood management. In this research, a case study of Darakeh River in Tehran as an important links in flood management and runoff conveying is used to reduce the costs of constructing flood conveying routs and water leakage. In the next step, rainfall values are obtained in return periods of 20, 25, 35, 50, 75 and 100 years by using hydrological relationships. Then, the output runoff is extracted by modeling the network in numerical software and the output hydrographs of the created model are entered into SWMM software. In order to present the output results of the SWMM model in a better format, the SWMM results are entered into SSA software. The SSA results are linked into the Harris Hawks Optimization (HHO) algorithm and finally, the construction cost and water leakage functions are optimized. Eventually, the results of HHO are compared with the Particle Swarm Optimization (PSO) algorithm to check the accuracy of HHO. The value of changes for width and height in bridges and channels are compared in two algorithms. As a result, the HHO algorithm reduces the volume of flood and water leakage in different return periods by presenting less cost as compared to the PSO algorithm.

Keywords: Harris Hawks Optimization, Rainfall, Surface Water, Runoff Collecting Network, Flood Management.

Received: 04 October 2024; Accepted: 07 September 2024

[*] E-mail: Zarif@sku.ac.ir
[1] Department of Civil Engineering, Shahrekord University, Shahrekord, Iran.
[2] Department of Water Engineering, Shahrekord University, Shahrekord, Iran.

CC BY

1. Introduction

The conveying of runoff and its collection is one of main problems of engineering community. Surface runoff collection networks are always expensive projects in every area. Therefore, reducing the construction cost of these projects is very important in the urban management. In other words, the lower construction cost of surface runoff collection projects will be created the better economic justification for implementation at the urban management level. Consequently, using new optimization methods for the optimal design of these networks with lower construction costs can be a very suitable idea. Many researches have been done on the simulation and modeling of the urban runoff collection network which are based on models such as MIKE 21, SWMM, SSA and etc. Researches on optimization issue of the urban runoff collection network are very limited in the literature.

Reddy and Kumar [1] presented multi-objective type of differential evolution (DE) algorithm. This method was called multi-objective differential evolution (MODE) and performed on a study model of a reservoir system. The results showed that the MODE algorithm provided better performance in optimizing the reservoir system compared to nondominated sorting genetic algorithm (NSGA).

Pan and Cao [2] used a combination of genetic algorithm and quadratic programming in the MATLAB software to optimize the cost function for a flood harvesting system. They compared the results of their work with the done previous works on the flood collection system and concluded that there is suitable alternative to the proposed previous works. Moghaddam et al. [3] worked on the optimal design of water distribution network using simple modified particle swarm optimization (SMPSO) algorithm. In their work, SMPSO algorithm was connected with EPANET 2.0 software. Their researches compared with the results of past studies including genetic algorithm (GA), simulated annealing (SA), shuffled frog leaping algorithm (SFLA), harmony search (HS) and scatter search algorithm (SS). The results showed that the SMPSO algorithm could be found the best solution in the shortest time compared to other algorithms. Azari and Tabesh [4] investigated studies on the optimal design of flood collection networks with considering hydraulic performance and best management practices (BMP). In their research, genetic multi-objective optimization algorithm (NSGA) was used. The results presented that using NSGA can be increased the system reliability up to 100% and the costs due to damages can be reduced to a surprising value. Abdy Sayyed et al. [5] investigated research with combined flow and pressure deficit in genetic algorithm for optimal design of water distribution network. Their study was on minimizing the cost function of constructing a water distribution network with sufficient pressure constraints at all points. They proposed a self-organizing penalty based on pressure heads to increase the effectiveness of numerical calculations and observe better solutions. In this research, it was observed that the modified penalty method was 4.2% cheaper than other researches in literature. Tanyimboh and Seyoum [6] presented an optimal design of water distribution network using multi-objective genetic algorithm without penalty function based on pressure simulation. They performed their studies on a real world study model with hundreds of variables. It was observed that the highest speed occurs at a distance of one meter from the water distribution network connections. Also, the cost function in this algorithm was reduced to 48.3% compared to previous algorithms. Ezzeldin and Djebedjian [7] worked on the optimal design of the water distribution network using the whale optimization algorithm (WOA). They used this new algorithm to optimize the cost function of pipe networks. This algorithm was implemented for 3 pipe networks and its results were compared with implemented previous algorithms on these networks. The results showed that the whale optimization algorithm (WOA) has the lowest design cost of the water distribution

network compared to other tested optimization algorithms on this network such as genetic algorithm, frog jump and etc. Heydari Mofrad and Yazdi [8] studied on a multi-objective evolutionary algorithm for the reconstruction of urban drainage systems. They found a hybrid simulation-optimization model in the area of Tehran's main drainage network. Also, they used a combination of an EPA SWMM and a new improved evolutionary algorithm called Non-Dominated Enhanced Differential Evolution (NSDE) to optimize the walls of dams and detention basins. The optimized strategies reduced the retrofitting cost and network flooding up to 61.7% and 37.5%, respectively. Diao et al. [9] applied the improved particle swarm optimization (SAPSO) algorithm to optimize the flood control in the cascade reservoirs. By using the SAPSO algorithm, the maximum outputs of Tianzhuang and Bashan reservoirs were reduced up to 8.6% and 18.5%, respectively.

Cemiloglu et al. [10] worked on the enhancement of the urban surface runoff conveyance system through optimization using non-dominated cases of the meta-heuristic algorithm of sorting differential evolution (NSDE). They followed an innovative approach by combining NSDE meta-heuristic algorithm with SWMM software. In their research, the objective functions were minimizing costs and reducing water leakage from the network. Results showed that the water leakage was decreased up to 95.26% by using this algorithm. It should be noted that other studies have been performed in the field of the optimal design for Surface runoff collection networks and water distribution networks over the years [11-15].

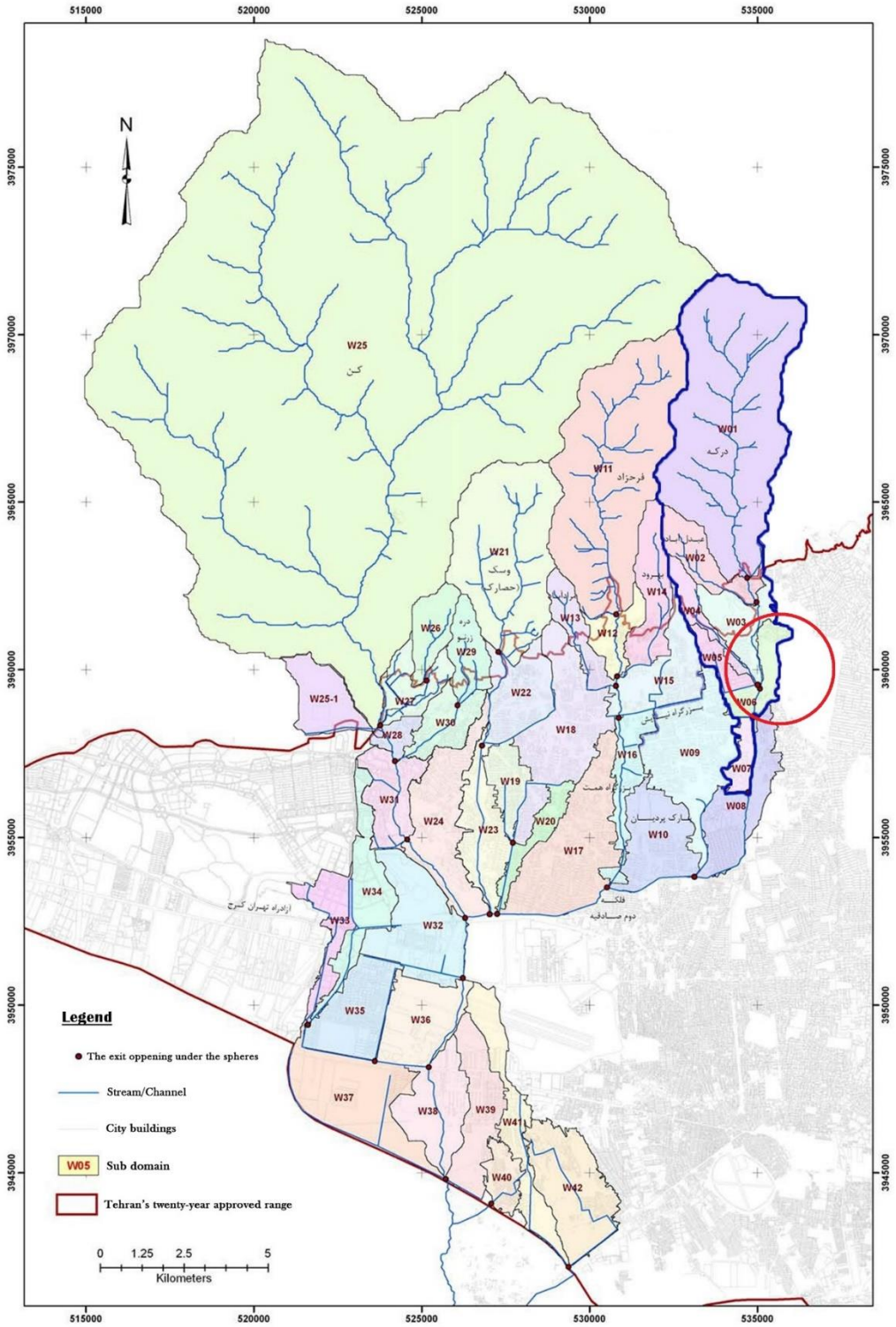
The Harris Hawks Optimization (HHO) algorithm is a meta-heuristic algorithm that has been published by Heidari et al. [16] focusing on the mass hunting strategy of Harris hawks. This algorithm has been seriously considered in recent years to solve various problems. For example, Abbasi et al. [17] worked on the performance of the HHO algorithm on the design of microchannel heat sinks. The results showed that the HHO algorithm has an excellent performance in reducing the entropy generation of the microchannel. Elgamal et al. [18] also studied the simulation of annealing with the improved algorithm of Harris Hawks to select features in the medical field. They proved the superiority of CHHO algorithm by comparing the results of HHO algorithm with algorithms such as GOA, BOA, PSO and ALO. As another research, Wang et al. [19] used the HHO algorithm to solve industrial engineering optimization problems. They proposed a combination of two algorithms, AO and HHO, along with a non-linear escape energy parameter and a learning strategy based on random opposition, i.e. IHAOHHO, to improve the search process. They evaluated that the results were satisfactory by confirming the performance of this algorithm on 23 benchmarks. In another research, Nematollahi and Zarif Sanayei [20] presented an optimal model for predicting the exploitation of groundwater based on the HHO algorithm for the simultaneous use of the surface and groundwater resources. They performed a numerical simulation of the Mahabad aquifer at first step and then, investigated the optimization model using the HHO algorithm for a period of 20 years. In the following, they created seven scenarios to predict the optimized groundwater exploitation (OGE) by using the results of HHO data and combining with artificial neural network (ANN). The results showed the superior performance of the ANN-HHO model when it includes all the input variables.

The HHO method has not been used seriously in the literature to optimize the design and construction costs of the surface runoff collection networks. In this research, the HHO method is used for optimal designing of these networks. In the current research, the rainfall of 20, 25, 35, 50, 75, 100 years of the West Tehran flood network is obtained in a number of sub-catchment. Then, the output runoff hydrograph is obtained from modeling the network in the HEC-HMS model. Next, the network flood is extracted by entering the runoff hydrograph into the SWMM

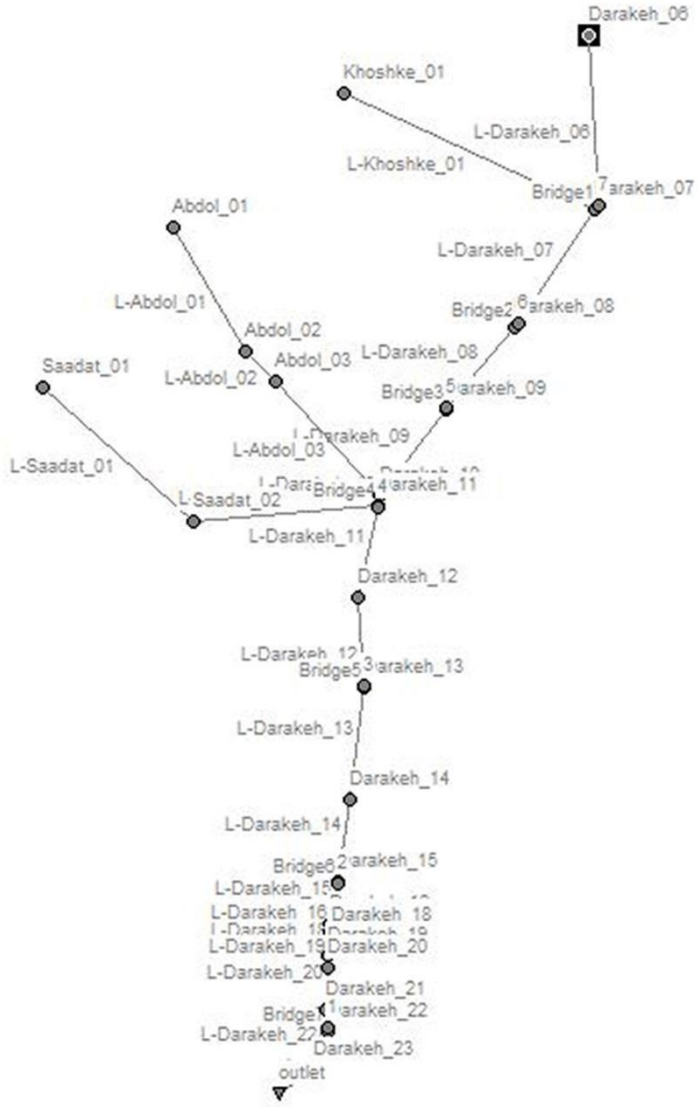
and SSA models. Finally, by coupling these results with the HHO algorithm, the cost optimization of the construction of the runoff collection network and the optimization of water seepage are done. The main assumptions for optimal design of surface runoff collection network are using the Manning equation as resistance equation and the Saint-Venant equations as one-dimensional flow equations for routing flow in the open channel.

2. Study area

Darakeh River is located in the area with coordinates 35°49'05.35"N 51°23'01.87"E in the coordinate system N39_Zone_UTM_1984_W (Figure 1). This river is one of Tehran's rivers, which originates from the southern slope of Tochal peak and flows into the main river with six branches. This river provides access to the southern slopes of Alborz in the northwest of Tehran. It should be noted that this river is not seasonal and flows throughout the year. In some of these sections of the studied channel, there is a lack of capacity to pass the incoming flood for the return period of 20, 25, 35, 50, 75, 100 years. Therefore, due to the basic and important conditions of this river, investigating the flooding of this channel is important and sensitive. West Tehran network includes 23 channels and 7 bridges, and according to the conducted studies in the water comprehensive plan for Tehran development, the rainfall time for this area is considered to 6 hours [21].


515000
520000
525000
530000
535000
3975000
3970000
3965000
3960000
3955000
3950000
3945000
N
W25
کن
W01
درکه
W11
فرحزاد
W21
وسک
حصارک
W02
W14
W04
W03
W13
W12
W26
W29
W05
W15
W25-1
W22
W27
W06
W30
W18
W28
W16
W09
W19
W07
W31
W24
W23
W20
W08
W17
W10
W34
W33
W32
W35
W36
W37
W38
W39
W41
W40
W42
Legend
The exit oppening under the spheres
Stream/Channel
City buildings
W05 Sub domain
Tehran's twenty-year approved range
0 1.25 2.5 5
Kilometers

(a)



(b)

Figure 1. (a) Study area (red circle); (b) The created network model in SWMM for red circle

3. Methodology

A flowchart of the performed method in this research is presented in Figure 2. First, the required data for simulation and optimization are prepared. These data include the geometric properties of the study area, weather properties such as rainfall value, properties and materials for the construction of channels and bridges. In the second stage, after determining the intensity of rainfall in different sub-catchments, the created runoff from rainfall in different sub-catchment and in different return periods is obtained by using HEC-HMS software. In the third step, the output hydrographs from HEC-HMS software are entered as time series input data to simulate runoff using SWMM and SSA models. In the fourth step, after running the done simulation in

SWMM, the channels outflow of the node location is determined.

In the fifth step, HHO and PSO algorithms are implemented in MATLAB software and the output flood from SWMM software is linked with MATLAB. In the sixth step, after implementing PSO and HHO algorithms in MATLAB software with the objective functions of reducing the cost and water leakage independently, the results are analyzed with comparison of PSO and HHO algorithms. In the seventh step, the results of HHO and PSO are evaluated.

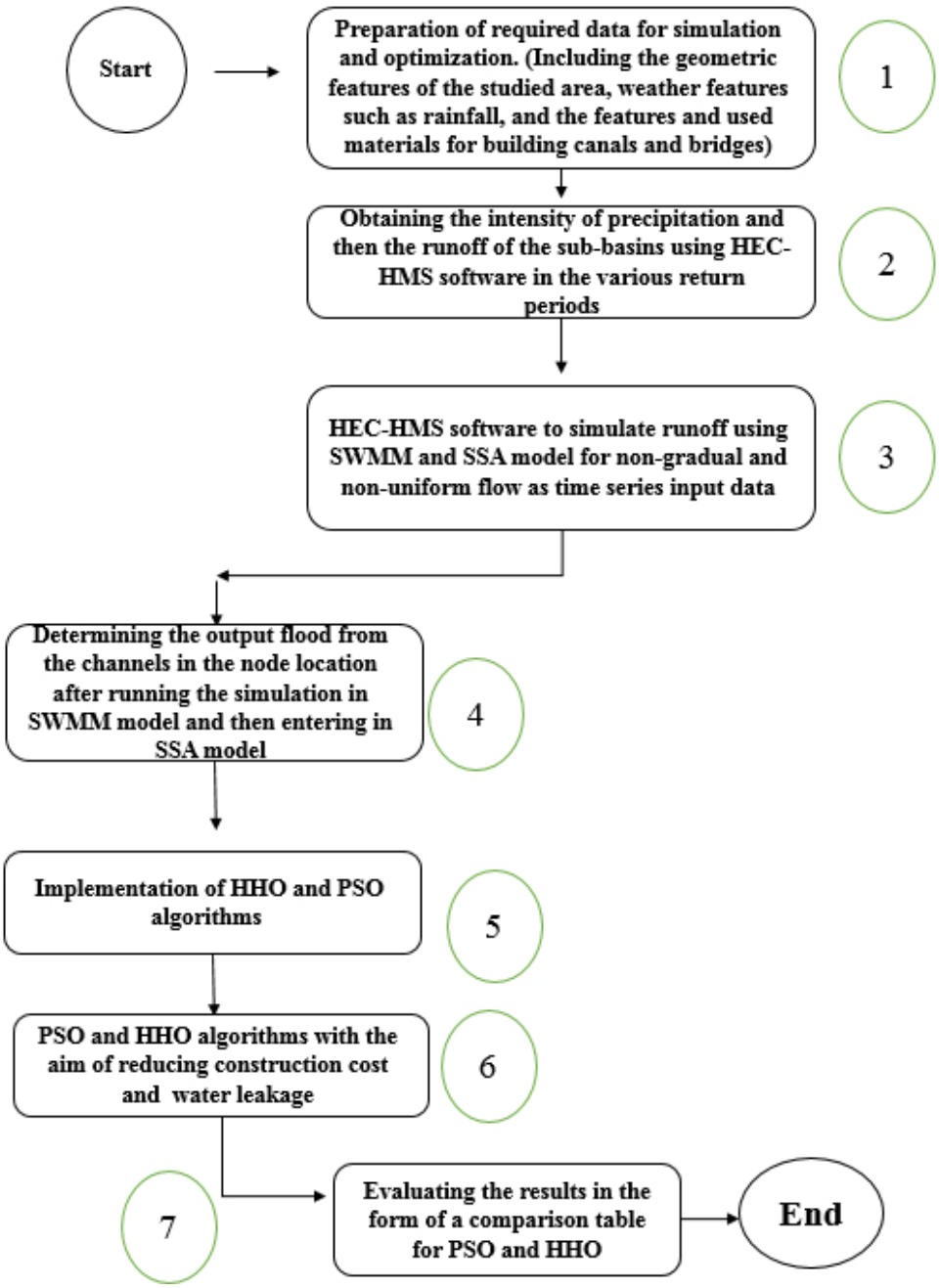


Figure 2. A flowchart of this research

4. Network simulation in HEC-HMS model

HEC-HMS model is used to obtain runoff from rainfall in the network. This software was presented in 1990 by the US Army Hydrologic Engineer Center under the name of HEC-1 model. In order to use this software, at first, the precipitation in all sub-basins including W01, W02,…., W07 should be obtained. To obtain the intensity of precipitation, the following relationships is used [22]:

$$i = C_{Alt.RP} D^{-0.645} \quad (1)$$

Where i is the intensity of rainfall (mm/hour), D is the duration of rainfall (minutes) and $C_{Alt,Rp}$ is a coefficient proportional to the design return period and the average height of basin. In addition, the temporal pattern of precipitation should be designed with the method of alternating blocks [23].

To enter other data into the HEC-HMS software for obtaining the rainfall-runoff hydrographs, the parameters of storage amount (S), initial abstraction (IA) and Lag time (LT) are entered and the SCS method is used [24]. Figure 3 shows the simulated network in the HEC-HMS. Also, the hydrographs of the output flood in the different return periods is shown in Figure 4. The negative flow values in the hydrographs of Figure 4 are the warm up time values for numerical methods in the initial times.

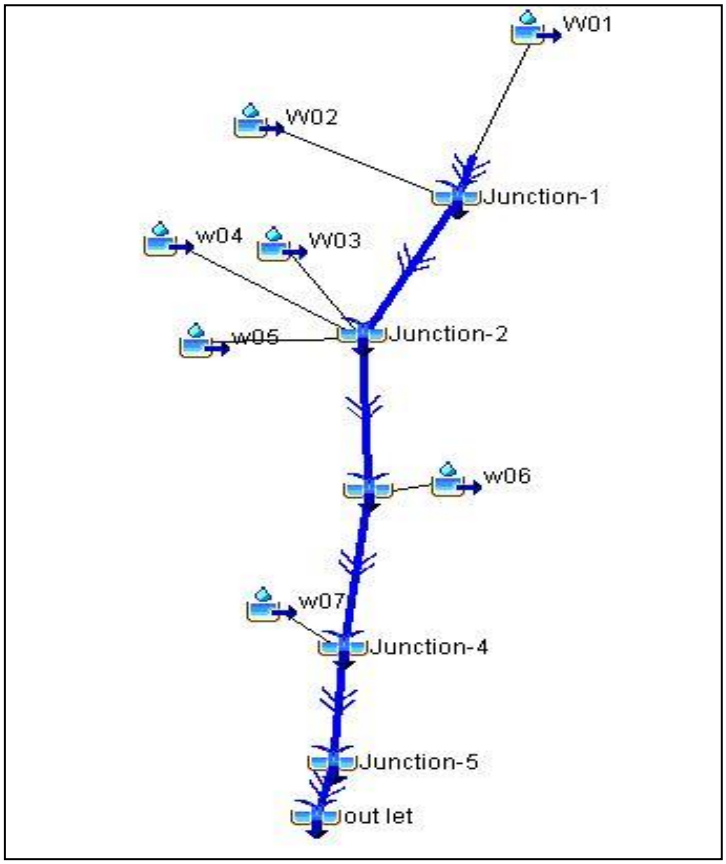


Figure 3. The simulated network in HEC-HMS.

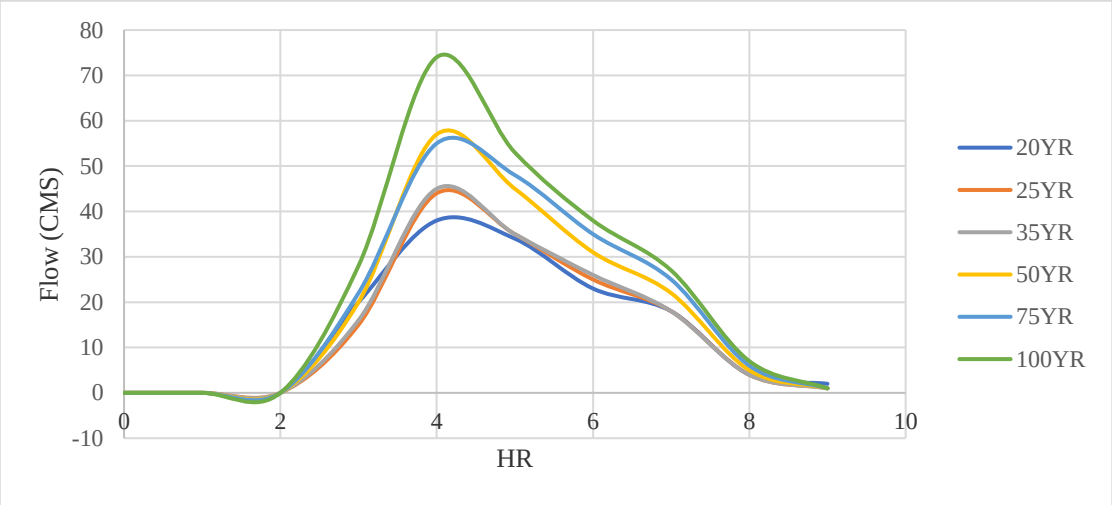


Figure 4. The hydrographs of the different return periods

5. Simulation with using SWMM and SSA

Hydrodynamic simulation in this research is performed with SWMM model. It was developed by the US Environmental Protection Agency (EPA). SWMM acts as a powerful hydrological simulation tool for analyzing and simulating storm runoff and drainage systems and their effects on urban systems [25]. SSA model is also a powerful hydrological simulation software developed by Autodesk and used for analyzing and simulating runoff and drainage systems with higher graphics than SWMM. Output hydrographs in HECHMS model is used to input time series data in SWMM model.

6. Using the optimizer model for network

6. 1. The objective functions

With the value of constant investment for flood management, it is possible to reduce the value of water leakage from the system with an optimal design. The water leakage is volume of runoff exceeding the capacity of channels and bridges. Consequently, further reduction requires an increase in the amount of investment in the project. Therefore, in this study, reducing the cost of building channels and bridges, as well as reducing network flood damage (the water leakage) are two independent functions. The objective functions are considered for the return periods of 20, 25, 35, 50, 75 and 100 years. Therefore, the objective functions are [26-28]:

$$\text{Function F1= Min Cost}_t = \sum_{i=1}^{n} Cost_i^B + \sum_{j=1}^{n} Cost_j^W = \sum_{i=1}^{n} f_1\left(H_i^B\right) + \sum_{j=1}^{m} f_2\left(H_j^W\right) \quad (2)$$

$$\text{Function F2= Min } \sum_{j=1}^{m}\left(V_{F,j}\right) \quad (3)$$

Therefore, F1 is a function of reducing the costs of building channels and bridges, and F2 is a function of reducing water leakage from the system. In functions, $Cost_i^B$ is the cost of building and repairing channels and bridges, $Cost_j^W$ is the cost of increasing the height of channels walls or bridges in the interval j, H_i^B is the height of channels, H_j^W is the height of the channel wall in the interval j, W_j^W is the bottom width of the channels, W_i^B is the width of bridges, m is the number of flood flow channel and n is the number of critical bottlenecks and $V_{F,j}$ is the network

flood and network water leakage volumes in the interval j. Considering the single objective, Harris Hawks algorithm is optimized by using the weighting method of both objective functions. The final objective function is presented in the following equation:

$$Z=0.5F1+0.5F2 \quad (4)$$

6.2. Constraints

The constraints in this optimization problem are equations 5, 6, 7 and 8 which are as follows:

$$V_{u\leq} V_{max} \quad (4)$$

$$H_i^B \epsilon \{H_1^B, H_2^B, \quad H_3^B, \dots, H_P^B\} \quad (5)$$

$$H_i^W \epsilon \{H_1^W, H_2^W, \quad H_3^W, \dots, H_q^W\} \quad (6)$$

$$\frac{\partial Q}{\partial x} + \frac{\partial A}{\partial t} = q \quad (7)$$

$$S_f = S_0 - \frac{\partial \upsilon}{\partial x} - \frac{\upsilon}{g}\frac{\partial y}{\partial x} - \frac{1}{g}\frac{\partial \upsilon}{\partial t} \quad (8)$$

where V_z is the flood velocity in the channels and bridge and V_{max} is the maximum flood velocity in the channels and bridges which is assumed to be equal to 6 m/s based on Iranian standards. *e* is the number of considered discrete values for the height and width of different bridges, r is number of considered discrete values for the height and width of channels, Q is the channel discharge, A is the area of the channel, S_f is the energy slope; S_0 is the bed slope, v is the channel velocity, y is the water depth and g is the acceleration of gravity. Saint-Venant's equations include the continuity equation (7) and the motion equation (8) as the hydraulic constraints of the problem, which are implicitly solved by implementing the SWMM model.

6.3. Harris Hawks optimization (HHO)

In this paper, a new algorithm called Harris Hawks Algorithm (HHO) is used to optimize the cost function in the construction of the runoff collection network and also minimize the water leakage of system. Heidari et al. [16], for the first time, presented the HHO algorithm. They proposed a nature-based population inspired model. The main idea of the Harris hawk algorithm is the collective behavior and hunting style of the Harris hawk in nature, which is known as surprise attack.

By confusing the prey during hunting, Hawks reduce the prey energy to escape and finally hunt it. The Harris Hawks algorithm has two main phases, discovery phase and exploitation phase. In the discovery phase of HHO, hawks are considered as candidate solutions and the best solution in each stage is considered as the target prey or an almost optimal solution. In HHO, hawks are randomly placed in different areas and waiting to identify a prey based on two strategies. The strategies are as follows:

$$X(t+1) = \begin{cases} X_{rand} \quad (t) - r_1 \left| X_{rand}(t) - 2r_2 X_{(t)} \right| & q \geq 0.5 \\ \left(X_{rabbit}(t) - X_m(t)\right) - r_3\left(LB + r_4(UB - LB)\right) & q \leq 0.5 \end{cases} \quad (9)$$

where X(t+1) is the location of the hawks in different iterations, which in this study is the width and height of channels and bridges which are randomly selected. The position of rabbit

($X_{rabbit}(t)$) in the iteration t is the amount of width and height channels and bridges in the iteration t. $X_{(t)}$ is the previous position of the hawks in the iteration t, $X_{rand}(t)$ is the random hawk position in the previous population, X_m is the average position of the hawks in the previous population. LB and UB respectively, are the lower and upper limits of variables that limits the amount of changes of width and height of channels and bridges. Rabbit energy in the HHO for this research is the building cost of channels and bridges for reducing flood. Also, E is the escape energy of the rabbit, which in this problem is the flood volume in the network in the iteration t. $\Delta X_{(t)}$ in the HHO algorithm in this research is the difference between the optimized widths and heights of the algorithm and random widths and heights. Also, Y and Z in this problem are the heights and widths of bridges and channels, which remain if they give a better answer, and otherwise the next iteration is done for comparison.

6.4. Optimized runoff exploration prediction

The effective parameters in the HHO and PSO algorithms such as the number of decision variables, the number of population and the number of iterations are listed in the Table 1:

Table 1. Number of input parameters for the HHO and PSO

Parameters	HHO	PSO
Number of decision variables	60	60
The number of repetitions	50	50
Number of populations	100	100

The maximum values of flooding in the network in the current state is shown in Table 2. This table shows how much flooding in the network will cause water leakage in different parts of the network in each return period.

Table 2. Maximum flood in the situation without network plan

Return period (year)	100	75	50	35	25	20
Flooding m^3/s	596.4	479.01	367	179.8	173.8	126

7. Discussion and results

7.1. The simulation results of the network

According to the range of necessary changes for each variable, increasing the height and width of the dam walls of Darakeh river, the height of existing bridges in the desired urban network, making the walls and bridges wider should be optimized. The optimization process in the region is performed for return periods of 20, 25, 35, 50, 75, 100 years. By using hydraulic modeling outputs, it has been observed that in some cases, the dimensions and size of existing bridges and channels in the region are inadequate for conveying of flood. Consequently, the channels and bridges are blocked and the water does not pass completely through the channels which causes over flooding and increases the costs and damages caused by flood. After implementing the SWMM and SSA models, the overflooding is observed. In order to observe the results of the model implementation in the return periods of 20, 25 and 50 years, Figures 5, 6 and 7 are shown. As shown in Figure 5, water leakage occurs at 3 points. The value of flooding in these three nodes is shown in Table 3.

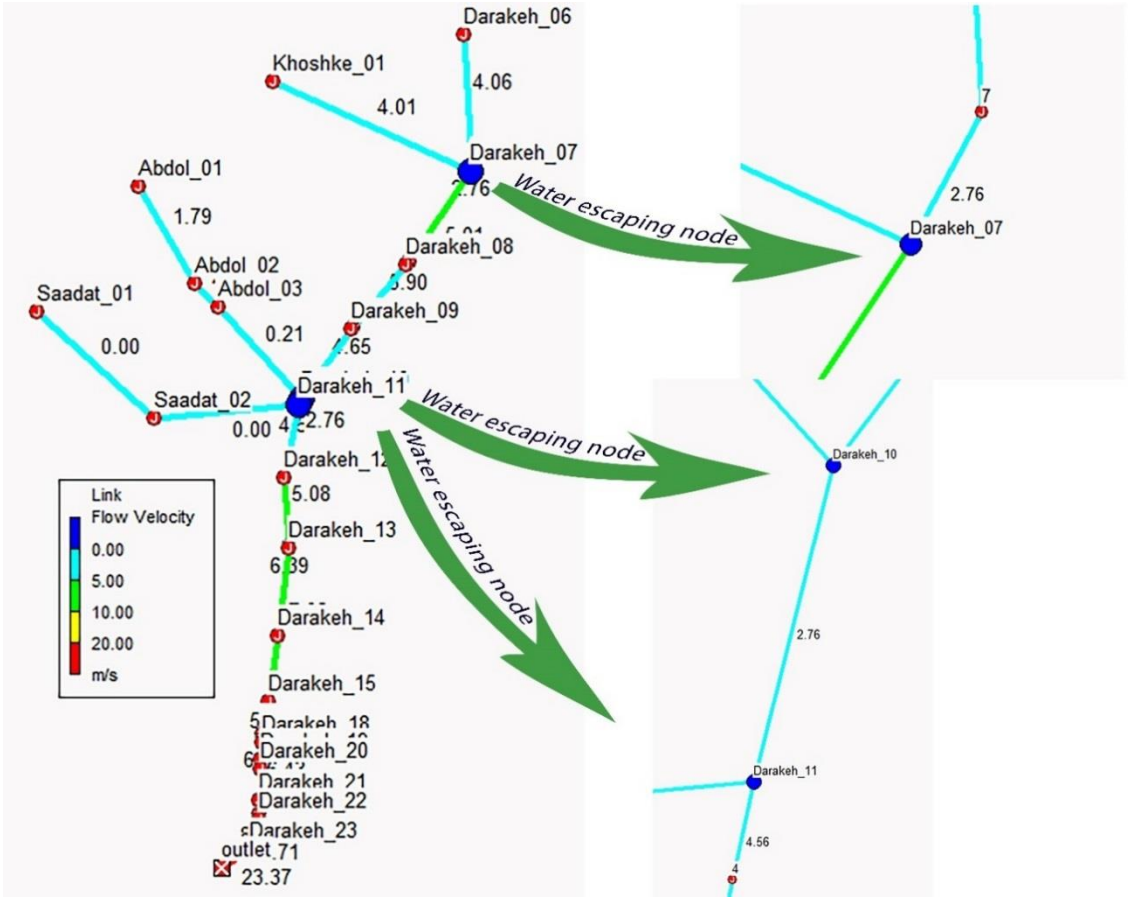


Figure 5. Network model in SSA in the return period 20 years

Table 3. Network flood volume for the return period of 20 years in the SSA and SWMM model

Node	Hours Flooded	Maximum Rate (CMS)	Day of Maximum Flooding	Hour of Maximum Flooding	Total Flood Volume (10^6 ltr)	Maximum Ponded Depth (m)
Darakeh_07	0.04	0.71	0	3:06	0.044	0.000
Darakeh_10	1.15	27.12	0	3:05	55.179	0.000
Darakeh_11	1.75	13.768	0	3:10	70.911	0.000

Figure 6 shows the points that experience water leakage during the return period of 25 years. Table 4 shows the flood volume at the location of these nodes.

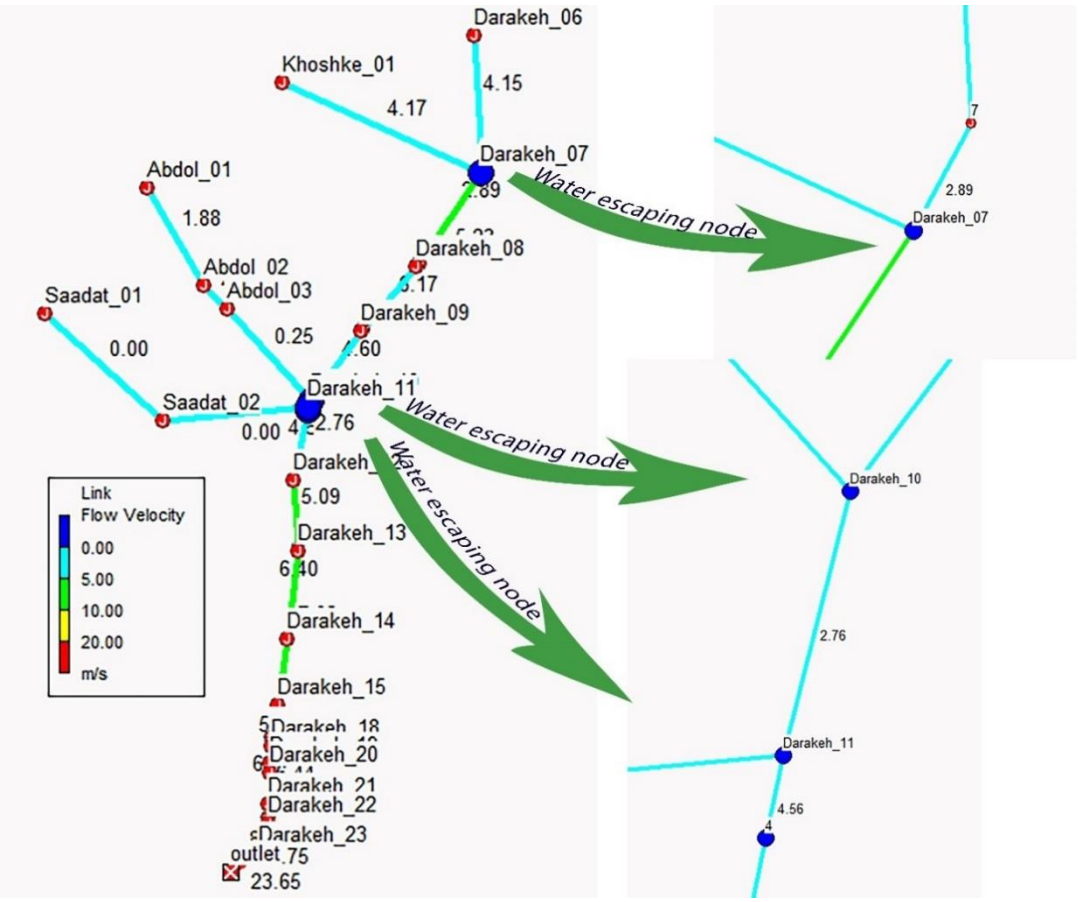


Figure 6. Network model in SSA in the return period of 25 years

Table 4. Network flood volume in the return period of 25year in the SSA and SWMM model

Node	Hours Flooded	Maximum Rate (CMS)	Day of Maximum Flooding	Hour of Maximum Flooding	Total Flood Volume (10^6 ltr)	Maximum Ponded Depth (m)
Darakeh_07	0.41	10.069	0	2:58	10.517	0.000
Darakeh_10	1.39	29.233	0	3:02	81.839	0.000
Darakeh_11	1.98	13.908	0	3:07	81.428	0.000

In the Figure 7 can be seen the points where water escape occurs during the return period of 50 years. Table 5 shows the flood values in each node.

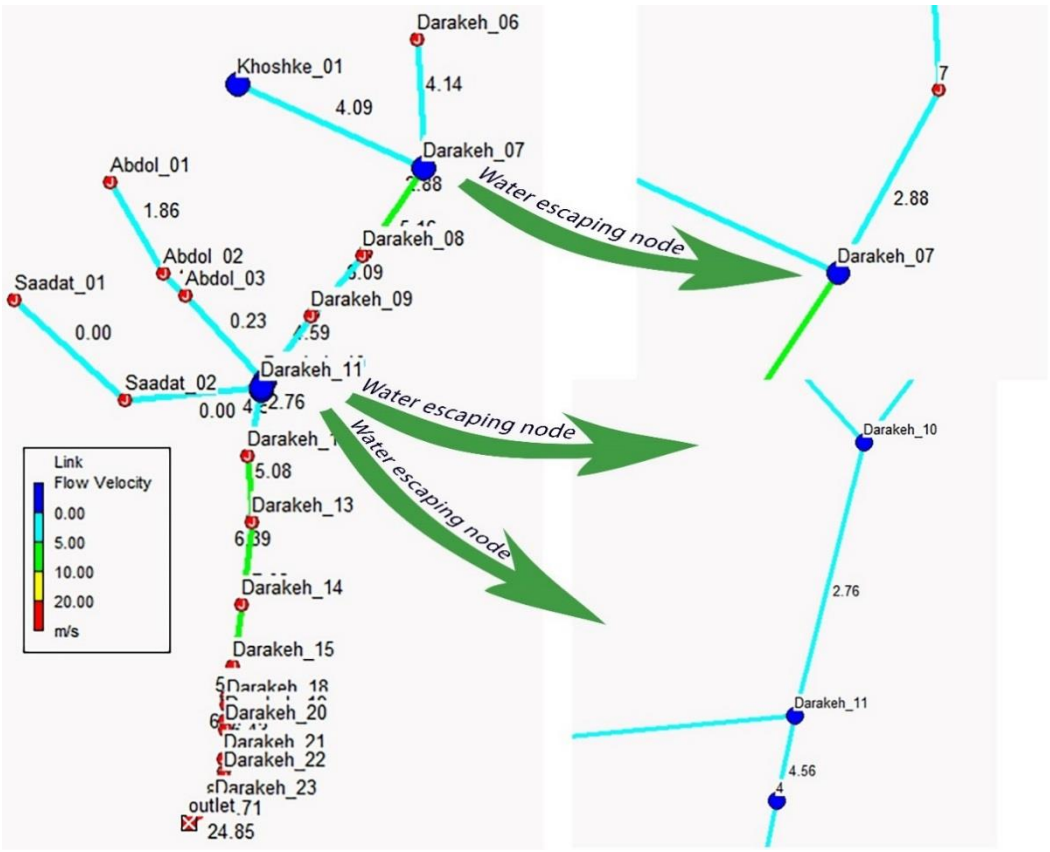


Figure 7. Network model in SSA in the return period of 50 years

Table 5. Network flood volume in the return period 50 years in the SSA and SWMM model

Node	Hours Flooded	Maximum Rate (CMS)	Day of Maximum Flooding	Hour of Maximum Flooding	Total Flood Volume (10^6 ltr)	Maximum Ponded Depth (m)
Darakeh_07	1.14	46.937	0	2:47	82.933	0.000
Darakeh_10	1.9	30.662	0	2:55	142.661	0.000
Darakeh_11	3.52	14.374	0	3:00	131.071	0.000
Khoshke_01	0.51	5.564	0	3:00	10.33	0.000

Figure 8 shows a comparison of the presented maximum rate values in tables 3, 4 and 5 for the return periods. As shown in this figure, as the return period increases, the maximum rate also increases.

According to the overflooding points in the simulation models in the SSA software, after implementing the optimization algorithms in the software, the results is checked in next section.

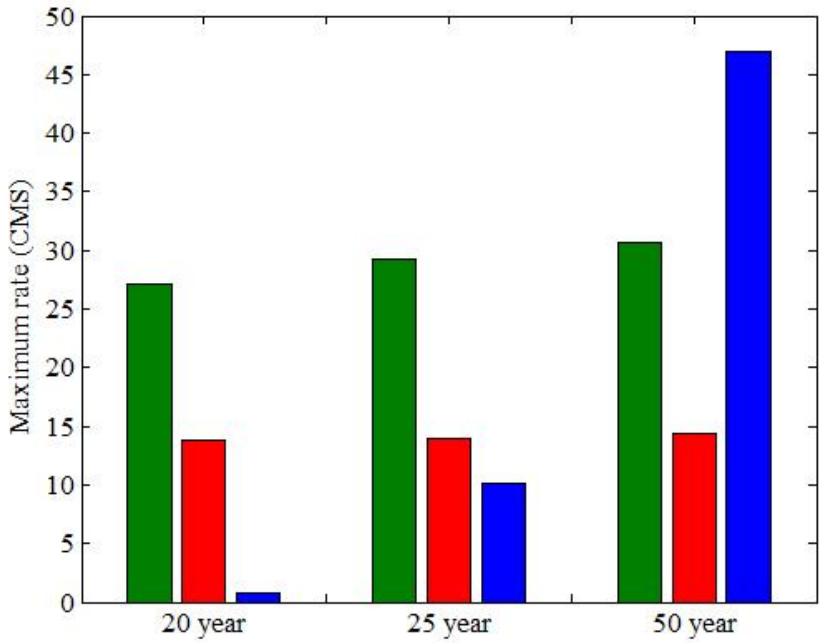


Figure 8. A comparison of the maximum rate values for different return periods (green: Darakeh_10; red: Darakeh_11; blue: Darakeh_7)

7.2. Results of HHO and PSO algorithms

Optimizer results for return periods of 20, 25, 35, 50, 75 and 100 years are obtained after implementing of single objective HHO algorithm. Also, this process is implemented with the PSO algorithm. The obtained results from these optimization models indicate the best solutions for different situations. At Table 6, the best answers of different return periods are given for comparison in HHO and PSO.

Table 6. The best solutions of optimal functions in different return periods for HHO and PSO

Optimizer	Function	Flood return periods					
		20 yr	25 yr	35 yr	50 yr	75 yr	100 yr
HHO	Cost (10^{10})	1.83	2.07	2.24	1.31	2.014	2.13
	Flooding (10^3 m^3)	0.002	0.002	0.002	0.779	0.786	0.107
PSO	Cost (10^{10})	3.96	2.74	2.55	2.48	2.63	2.71
	Flooding (10^3 m^3)	0.4	0.1	0.025	0.226	0.032	0.045

In the performed optimization model, the decision variables are defined in such a way that they have the ability to solve the objective functions of the studied problem. So that, the optimization model reduces the volume of flood output and the costs according to the implementation plan. Furthermore, the best optimal design for the channel dimensions is created with considering objective functions. It should be noted that the changes corresponding to each channel or bridge are in the simulator model according to the placement and definition of the

channel and the bridge. These changes are completely specific for any bridge or channel. The position of channels and bridges are shown in Figure 9. As shown in the Table 7, it is not necessary to change the dimensions and size of all channels or bridges. Therefore, after solving the optimizer problem for each design, it has been shown that in some bridges or channels that are critical in the optimizer model, changes in their dimensions and sizes should be applied. In the table 7, H_i^B is the height of bridges, W_i^B is the width of bridges, W_j^W is the channels width and H_j^W is the channels height. According to Table 7, it is clear that in most places, HHO algorithm reduces the construction costs and flooding by obtaining the least possible changes in the heights and widths of the channels. These changes reduce flood in the urban network, with regard to the reduction of operational costs.

It should be noted that achieving such the optimized plan may be impossible without optimization programs, which shows the efficiency of these models to carry out the optimal design of the surface water collection network in are urban areas.

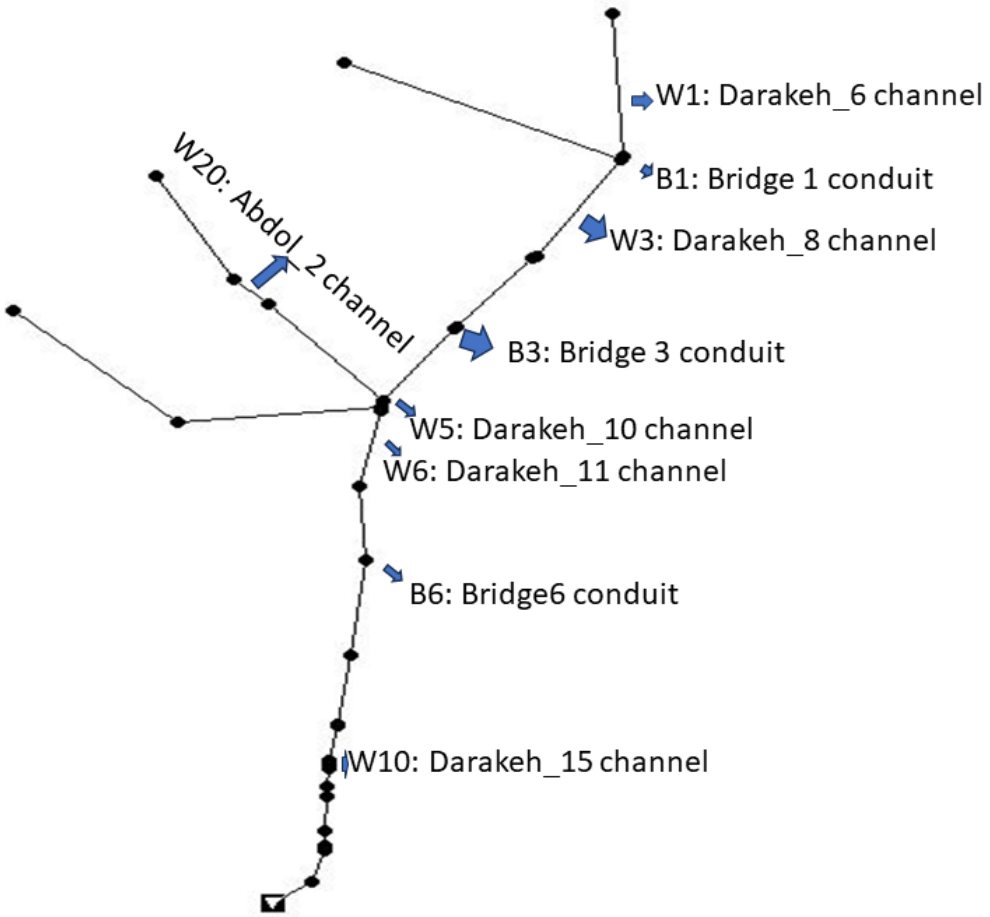


Figure 9. The location of some bridges and channels for comparison of HHO and PSO results

Table 7. Results and changes of some widths and heights of channels and bridges in HHO and PSO algorithms.

No	Variable	20	25	35	50	75	100	optmizer
1	H_3^B	0.04	0.2	1.5	0.64	4.53	0.4	HHO
		3.16	0.62	4.5	2.5	2.81	0.42	PSO
2	W_1^B	1.3	0.66	0.01	0	1.85	3.06	HHO
		2.78	1.33	2.1	2.14	5.44	3.29	PSO
3	H_3^W	0.32	0.45	0.67	0	1.53	0.02	HHO
		0	0.07	0.97	0.07	0	0.14	PSO
4	H_6^W	2.06	1.76	0.24	1.34	2.49	0.76	HHO
		1.29	0.59	1.76	1.57	0.06	0.82	PSO
5	H_{10}^W	0.04	1.31	2.31	1.34	0	0.15	HHO
		2.99	0.9	0.06	3.89	7.7	1.9	PSO
6	H_6^B	0.04	5.02	1.07	3.55	1.04	0.79	HHO
		6.99	3.3	6.16	7.44	2.77	0.78	PSO
7	W_5^W	1.41	1.93	3.83	7.54	5.97	9.99	HHO
		1.81	3.48	4.16	5.44	8.32	9.25	PSO
8	W_{10}^W	0.04	0.84	0.66	0	5.52	4.25	HHO
		0.8	7.36	0.75	2.58	9.36	1.62	PSO
9	W_{20}^W	0.46	2.33	1.34	1.12	1.57	5.25	HHO
		3.02	1.71	0.99	8.81	5.97	2.04	PSO

In this research, by comparing the best answers with PSO, the best design for the surface water collection network by HHO was selected. This research showed that the HHO algorithm has a better performance than the PSO algorithm in reducing costs. Also, with a better speed, the value of network flooding tends to zero.

8. Conclusion

In this research, the single-objective Harris Hawks optimization (HHO) algorithm was used to solve the optimizer problem and the particle swarm optimization (PSO) algorithm was used for comparison. HEC-HMS model has been used to determine the rainfall-runoff model. The hydraulic model used in this research to discuss flood management and control by SWMM and SSA hydrodynamic models. Two objective functions were considered in this research. It was found that the functions are in the form of reducing costs and the outflow of water from the urban network in Darakeh River in Tehran city;

The optimization process for the urban network was performed for the return periods of 20, 25, 35, 50, 75 and 100 years. The results showed that the HHO algorithm has a better performance than the PSO algorithm and reduces the costs to a suitable extent. The results showed that the HHO algorithm has a better performance than the PSO algorithm and reduces the costs to a suitable extent. Also, the results presented the efficiency of the HHO algorithm to carry out the optimal design of the surface water collection network in are urban areas. The HHO method has not been used in past researches for optimizing the construction cost of the surface

runoff collection network in the current form. The modeling form and linking the SWMM and SSA results with the HHO method in the current study can be a suitable idea for future researches.

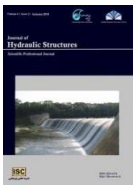
References

1. Reddy M. J., Kumar D. N. (2007). Multiobjective differential evolution with application to reservoir system optimization. Journal of Computing in Civil Engineering, pp: 21(2):136–146.
2. Pan T, Kao J (2009). GA-QP model to optimize sewer system design. Journal of environmental engineering, pp: 135(1):17–24.
3. Moghaddamam A, Alizadeh A, Faridhosseini A, Ziaei A. N., Heravi D. F. (2018). Optimal design of water distribution networks using simple modified particle swarm optimization approach. Desalination and Water Treatment, pp: 104: 99–110.
4. Azari B, Tabesh B (2018). Optimal Design of Stormwater Collection Networks Considering Hydraulic Performance and BMPs. International Journal of Environmental Research, pp: 12: 585-596.
5. Abdy Sayyed M. A. H., Gupta R, Tanyimboh T (2021). Combined flow and pressure deficit-based penalty in GA for optimal design of water distribution network. ISH Journal of Hydraulic Engineering, pp: 27:146-156.
6. Tanyimboh T. T, Seyoum A. G. (2020). Design optimization of water distribution networks: real-world case study with penalty-free multi-objective genetic algorithm using pressure-driven simulation. Water SA. pp: 46:(3): 465–475.
7. Ezzeldin R. M., Djebedjian B (2020) Optimal design of water distribution networks using whale optimization algorithm. Urban Water Journal, pp: 17 (1):14-22.
8. Heydari Mofrad H., Yazdi J. (2022). An enhanced multi-objective evolutionary algorithm for the rehabilitation of urban drainage systems. Engineering Optimization, pp: 54 (2), 349-367.
9. Diao Y., Ma H., Wang H., Wang J., Li S., Li X., Pan J., Qiu Q. (2022). Optimal Flood-Control operation of cascade Reservoirs Using an Improved Particle Swarm Optimization Algorithm. Water, pp: 14(8): 1239.
10. Cemiloglu A., Zhu L., Chen B., Lu L., Nanehkaran Y. A. (2023). Enhancing Urbun Surface Runoff Conveying System Dimensions through Optimization Using the Non-Dominated Sorting Differential Evolution (NSDE) Metaheuristic Algorithm. Water, pp: 15(16): 2927.
11. Babonneau F., Gilbert D., Piller O., Vial J.P. (2024). Robust optimal design of a tree-based water distribution network with intermittent demand, European Journal of Operational Research, pp: 319 (3): 834-844.
12. Riyahi M. M., Bakhshipour A. E., Haghighi A. (2023). Probabilistic warm solutions-based multi-objective optimization algorithm, application in optimal design of water distribution networks, Sustainable Cities and Society, pp: 91: 104424.
13. Jenks B., Pecci F., Stoianov I. (2023). Optimal design-for-control of self-cleaning water distribution networks using a convex multi-start algorithm, Water Research, pp: 231: 119602.
14. Essamlali I., Nhaila H., El Khaili M. (2024). Optimizing runoff and pollution mitigation through strategic low-impact development (LID) integration in the Bouznika city development plan, Case Studies in Chemical and Environmental Engineering, pp: 10: 100838.
15. Liu Z., Han Z., Shi X., Liao X., Leng L., Jia H. (2023). Multi-objective optimization

methodology for green-gray coupled runoff control infrastructure adapting spatial heterogeneity of natural endowment and urban development, Water Research, pp: 233: 119759.
16. Heidari A. A., Mirjalili S, Faris H, Aljarah I, Mafarja M, Chen H. (2019) Harris hawks optimization: Algorithm and applications. Future Generation Computer Systems, pp: 97:849-872.
17. Abbasi A., Firouzi B., Sendur P. (2021). On the application of Harris hawks optimization (HHO) algorithm to the design of microchannel heat sinks. Engineering with Computers, pp: 37: 1409-1428.
18. Elgamal Z. M., Yasin N. B. M., Tubishat M., Alswaitti M., Mirjalili A. S. (2020). An Improved Harris Hawks Optimization Algorithm with simulated Annealing for Feature selection in the Medical field. IEEE Access, pp: 8: 186638-186652.
19. Wang S., Jia H., Abualigah L., Liu Q., Zheng R. (2021). An Improved Hybrid Aquila Optimizer and Harris Hawks Algorithm for solving industrial engineering optimization problems. Processes, pp: 9(9): 1551.
20. Nematollahi Z., Zarif Sanayei H. R., (2023). Developing an optimized groundwater exploitation prediction model based on the Harris hawks optimization algorithm for conjunctive use of surface water and groundwater resources, Environmental Science and Pollution Research, pp: 30: 16120-16139.
21. TDDTM. 2011a. Tehran Stormwater Management Master Plan, Vol 2, Part 3: Urban Food Hydrology & Sediment Load, December 2011. Tehran: Technical & Development Deputy of Tehran Municipality.
22. TDDTM. 2011b. Tehran Stormwater Management Master Plan, Vol 4: Existing Main Drainage Network, Part 2: Hydraulic Modeling and Capacity Assessment, December 2011. Tehran: Technical & Development Deputy of Tehran Municipality.
23. Na W., Yoo C., (2018). Evaluation of Rainfall Temporal Distribution Models with Annual Maximum Rainfall Events in Seoul, Korea. Water, pp: 10(10): 1468.
24. USACE. 2008. Hydrologic Modelling System HEC-HMS, Quick Start Guide, Version 4.0. Davis: Institute for Water Resources Hydrologic Engineering Center.
25. Jang S., Cho M., Yoon J, Yoon Y., Kim S., Kim G., Kim L., Aksoy H., (2007). Using SWMM as a tool for hydrologic impact assessment. Desalination, pp: 212 (1–3): 344-356.
26. Lord S. A., Ghasabsaraei M. H., Movahedinia M., Shahdany S. M. H., Roozbahani A. (2021). Redesign of stormwater collection canal based on flood exceedance probability using the ant colony optimization: study area of eastern Tehran metropolis. Water Science & Technology, pp: 84 (4): 820-839.
27. Yazdi, J. (2016). Decomposition Based Multi Objective Evolutionary Algorithms for Design of Large-Scale Water Distribution Networks. Water Resources Management, pp: 30 (8): 2749–2766.
28. Yazdi, J., A. Sadollah, E. H. Lee, D. G. Yoo, and J. H. Kim. (2017). Application of Multi-Objective Evolutionary Algorithms for the Rehabilitation of Storm Sewer Pipe Networks. Journal of Flood Risk Management, pp: 10 (3): 326–338.

© 2024 by the authors. Licensee SCU, Ahvaz, Iran. This article is an open access article distributed under the terms and conditions of the Creative Commons Attribution 4.0 International (CC BY 4.0 license) (http://creativecommons.org/licenses/by/4.0/).

Journal of Hydraulic Structures
J. Hydraul. Struct., 2025; 11(1): 20-40
DOI: 10.22055/jhs.2024.47306.1306



OPEN ACCESS

Enhancing the seismic performance of platforms in intermediate water depth using shape memory alloy dampers

Mohammad Jafari[1]
Hamid Bayesteh[*1]
Reza Rasti Ardakani[1]

Abstract

Wharves supported by vertical piles are very common marine structures with suitable seismic responses. Nevertheless, they severely suffer from extensive lateral displacement in both design and service earthquake level state. Conversely, wharves with batter piles have limited displacement, but they are often restricted by numerous standards and guidelines due to the significant seismic base shear and undesirable failure modes such as buckling, pullout, and deck punching. This study aims to assess the efficacy of shape memory alloy (SMA) based dampers in controlling both displacement and seismic base shear within acceptable limits. To achieve this goal, a thorough investigation is conducted on an oil terminal platform, located north of Qesh in Iran, with a water depth of 20m, as a real case study. A structural system consisting of vertical and batter piles equipped with SMA dampers and base isolators is proposed, wherein batter piles were not directly connected to the deck. At first, three common scenarios (vertical piles, combination of vertical and batter piles, and friction dampers) are examined, and then the proposed SMA damper system is comprehensively evaluated and compares with the available solutions. The findings reveal that systems employing SMA dampers exhibit significantly reduced seismic base shear (20% reduction) and lateral displacement (68% reduction) compared to those with vertical piles. Additionally, the lateral displacement observed in systems utilizing SMA dampers falls within the range of those employing batter piles, while the seismic base shear is limited to only 40% of the system with batter piles.

Keywords: SMA, damper, wharves, batter piles, vertical piles.

Received: 30 June 2024; Accepted: 14 August 2024

1. Introduction

Wharves and platform have been widely constructed in Iran to import or export different materials. Among these marine structures, oil and gas platforms with jetty access bridges are utilized for docking large tankers, in variable water depths ranging from 10m to 20m. Typically,

[*]Email: h_bayesteh@sbu.ac.ir
[1]Faculty of Civil, Water and Environmental Engineering, Shahid Beheshti University, Tehran, Iran.

CC BY

these structures are pile-supported platforms including concrete decks and batter/vertical piles. Among different loads on marine structures, wave and earthquake imposes large lateral displacements that must be limited to an allowable range to ensure the operational integrity of the superstructures. Particularly in earthquake, the dual challenges of displacement and ductility become prominent. For instance, structures employing ductile components like vertical piles often suffer from excessive top-deck displacement, interrupting the structure's serviceability not only during design earthquakes but also under service-level seismic events. Conversely, structures equipped with batter piles exhibit a more tolerable range of displacement but display inadequate seismic performance [1]. Accordingly, most of standards and recommendations discourage the use of batter piles in wharves [1], and it is recommended to design the structure in elastic level in the presence of batter piles [1]. The primary inappropriate failure mechanisms associated with batter piles include pull-out from the soil, pile buckling, pile-to-deck separation, and deck punching effects [2].

In recent earthquakes, wharves with batter piles were experienced more serious damages in comparison with vertical piles [3]. For instance, pile-deck separation in batter piles were observed in Chilie earthquake at 2010 [4]. Additionally, research by [5] has highlighted the undesirable effect of vertical load carried by batter piles which reduces their performance during earthquake. Consequently, numerous studies have been developed to enhance seismic resilience of pile-supported structures, while keeping lateral displacement within acceptable range [5]. Generally, three strategies of employing fuses, dampers, isolators, or combinations them have been explored in the literature to enhance the seismic response of these structures.

Improvement in seismic response and reduction in displacement by utilizing viscous damper in combination with batter piles were investigated in [6]. It was also indicated in [6] that maintaining the displacement of structures within acceptable limits solely through the use of vertical piles (without additional measures) is very expensive. Friction dampers [7] and semi-active hydraulic dampers [8] have been successfully deployed in offshore jackets to regulate displacement [7]. Notably, friction dampers have also been employed to mitigate platform vibration caused by wave motion [9].

Experimental studies show the crucial role of connections on seismic response of the wharves [10]. Accordingly, a simple idea to improve seismic responses is to use scarified fuses in connections. Incorporation of yielding fuses in combination with batter piles has demonstrated a more flexible response characterized by ductile failure mechanisms in both the fuses and vertical piles [11]. Various investigations focusing on shear [12] and flexural [13] fuses have indicated a reduction in base shear within structures during seismic events.

Furthermore, utilizing LRB isolators in conjunction with batter piles has been explored in wharves, aiming to decrease the seismic base shear of the structure as documented in [14]. Additionally, viscous isolators have been studied for offshore jackets in China, aiming to improve the dynamic response of these structures. [15]The primary effects of isolators include elongating the period and managing torsion within structures [16], as well as ensuring uniform distribution of force among various piles [17]. The integration of base isolators alongside viscous dampers resulted in a notable reduction of 31% in displacement and 48% in base shear in Resalat jacket in the Persian Gulf [18].

As previously mentioned, in oil terminals containing sensitive equipment, both reduction in lateral displacement and base shear ensure operational integrity and safety. Recently, there has been significant development in SMA dampers exhibiting super-elastic properties, aimed at enhancing seismic response with minimal permanent displacement. MRF-SMA dampers [19] and combination of friction and SMA dampers [20] have been effectively used in offshore

jackets. However, to the authors' knowledge, no study has yet assessed the effectiveness of SMA dampers in wharves. Accordingly, this study investigates the effect of SMA dampers on platforms supported by vertical/batter piles without bracing systems, in 20m water depth where suitable for common oil tankers, to control both lateral displacement and base shear in earthquake.

The manuscript is structured as follows: Theoretical backgrounds are discussed in Section 2, and assumptions of modeling are presented in Section 3. Sections 4-6 express the proposed system, which is evaluated through static pushover and dynamic analysis. The findings are summarized in Section 7.

2. Theory

2.1. Piles and Decks

Wharves or platforms are type of marine structures used for mooring ships, constructed from concrete decks supported by steel piles (Figure 1). Typically, in these structures, vertical loads are transferred to the soil through deep piles embedded into the ground. The deck, which is supported by the piles, typically works to evenly distribute the applied loads onto the piles. Common resisting systems against lateral loads are vertical and/or batter piles. The structures are classified into rigid or flexible structures based on their stiffness against lateral loads. The degree of flexibility of these structures depends on the type of materials, soil conditions, and type of structural system [1]. Marine structures are comprehensively affected by lateral wave, wind and seismic loads. Among them, the presented study is focused on the seismic load as worst case in south of Iran.

Common practice to withstand seismic loads is to use the vertical piles with flexural behavior. These types of structures exhibit desirable flexibility with minimal seismic base shear. Additionally, in many cases, vertical pile systems are very cost-effective and offer greater feasibility in terms of construction. Therefore, they are preferred option for wharves and platforms. However, the important challenge with these types of structures, in water depths between 10 to 20 meters, is significant displacements under wave, wind, and earthquake loads, severely affecting the superstructure. On the other hand, a common alternative to overcome this challenge is to use batter piles with acceptable stiffness to control displacement. But batter piles show extremely undesirable seismic response. Accordingly, in this research, the effect of SMA dampers on improving seismic behavior and reducing displacements of platforms is investigated.

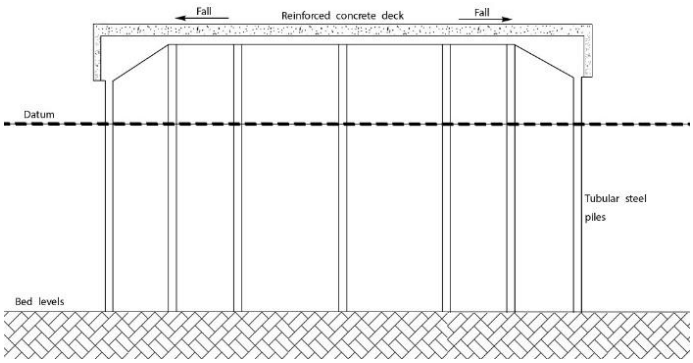


Figure 1. Wharf Supported by Vertical Piles

2.2. Shape Memory Alloys

Shape Memory Alloys (SMAs) are intelligent and innovative materials that, due to their unique behaviors, have found various applications in different fields of science and engineering in recent decades. They play a fundamental role in the development and implementation of smart materials devices. When integrated into the structures, they provide functionalities such as sensing, energy dissipation, monitoring, self-adapting, and structural repair [21].

The reversible phase change capability of these alloys allows them to endure significant shape changes and, depending on the temperature and applied stress conditions, return to their original shape when loaded or subjected to heat. This capability, accompanied by changes in mechanical, thermal, and electrical properties, has made shape memory alloys a suitable option for use in smart, advanced, and adaptive structures. When used in civil structures, these materials can reduce the damage caused by earthquakes as passive, semi-active, or active elements [21].

Until now, various types of shape memory alloys (SMAs) have been recognized. The most commonly used SMA in the industry is nickel-titanium alloy, also known as nitinol (NiTi), which is utilized in the construction for seismic applications such as passive vibration control and energy dissipation. However, the high cost of production and processing of this alloy has been reduced its widespread use in large-scale construction projects. In recent years, iron-based shape memory alloys (Fe-SMAs) have obtained significant attention in civil engineering due to their desirable properties for structural applications and reasonable cost. The recent progress in manufacturing and understanding of these alloys has expanded their application for the repair and strengthening of structures using pre-stressed Fe-SMA tendons [21].

Shape memory alloys exist in two crystalline phases called austenite and martensite. The austenite phase is the primary phase with high symmetry and stability at high temperatures and low stresses. On the other hand, the martensite is a phase with lower symmetry and stability at low temperatures and high stresses. By applying thermal or mechanical loading, these two phases can transform into each other. This reversible transformation of phases is called martensitic transformation, which affects all the characteristics of shape memory alloys, presenting them as smart materials [21]. Figure 2 illustrates martensitic transformation resulting from temperature change without applying stress. SMAs have four characteristic temperatures: As, Af, Ms, and Mf, which represent the austenite start temperature, austenite finish temperature, martensite start temperature, and martensite finish temperature, respectively. Martensitic transformations form a thermal hysteresis, meaning that direct and reverse transformations do not occur at the same temperature [21].

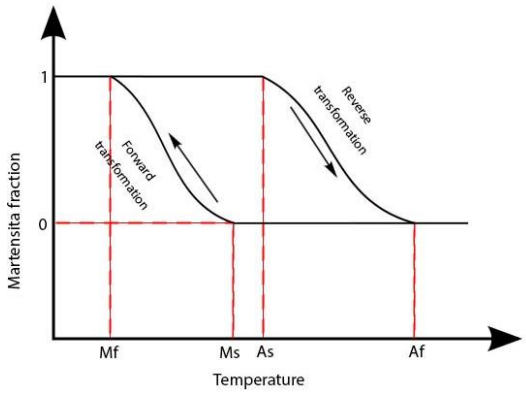


Figure 2. Martensitic transformation resulting from temperature change [21]

The stress-strain curve of this transformation, as shown in Figure 3, consists of three parts: an initial elastic branch with the initial elastic modulus of austenite, a horizontal segment where the phase transformation from austenite to martensite occurs, and again an elastic branch with the initial elastic modulus. Reverse transformation occurs during unloading and material returns to its initial shape without any residual strain. The reverse transformation along a different path forming a hysteresis loop representing the energy dissipation. This behavior is called superelastic or pseudoelastic behavior, because of zero residual strain in this loop [21].

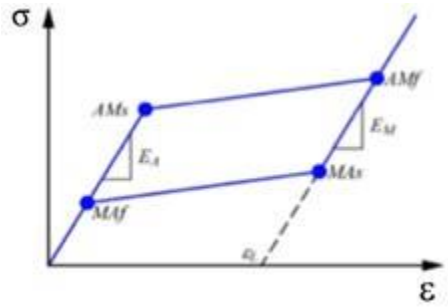


Figure 3. stress-strain carve of SMA [21]

When SMA is in the martensitic state under stress greater than the yield stress, due to the gradual reorientation of martensitic variants, it shows a high energy dissipation capacity, as depicted in Figure 4. Clearly, a large hysteresis loop is seen in this figure during cyclic loading and unloading. The mentioned crucial property of SMAs has led to attract special attention in passive control of structures. The energy dissipation capability of these materials reduces demand on the main members of the structure, and due to the high resistance to fatigue, they can also be used after earthquakes without replacement.

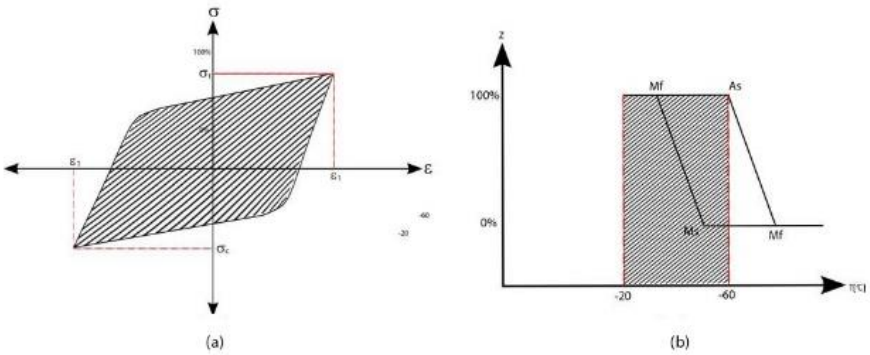


Figure 4. Martensitic Strain in SMA (a) Hysteresis Diagram (b) Martensitic Strain Temperature diagram at Zero Stress (Parameter Z refers to the martensite ratio and T refers to temperature) [21]

3. Assumptions of Modeling

3.1. Case Study of operational platform

An operational platform with area $30m \times 30m$ and 5×5 pile arrangement, as depicted in Figure 5, is investigated as a real case study in Qeshm. Height of platform from the seabed is 30 meters, with 20 meters underwater and 10 meters above the sea water level. Steel pipe piles with diameter of 1.3 meters and thickness of 19 millimeters is used. Additionally, thickness of

concrete deck is 40cm, and concrete beams with dimensions of 1m×2m are considered. The properties of the materials are as shown in Table 1.

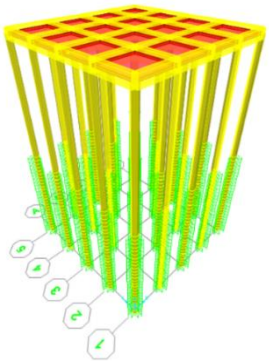


Figure 5. Model of operation platform with vertical piles in Qeshm.

Materials	Concrete	Steel (St52)
Yield stress/Compressive stress	35 MPa	360 MPa
Ultimate stress	-	520 MPa
Elastic modulus	27800 MPa	200000 MPa
Poisson' ratio	0. 2	0. 3

3.2. Soil-Structure Interaction

In the present study, a nonlinear spring model for soil-structure interaction based on the API code [22] has been utilized, as depicted in Figure 6. In this figure, tangent and normal springs to the pile's shaft are presented by t-z and p-y springs, respectively. Regarding the loading on the pile tip, which exhibits different behavior compared to the pile shaft, the end spring is designated as the "q-z spring".

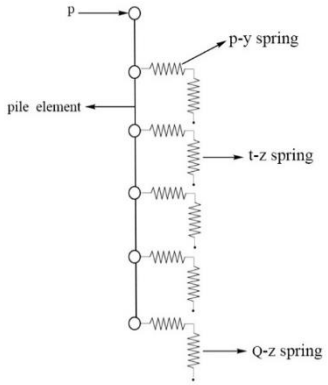


Figure 6. Soil-structure interaction for pile with p-y, t-z, and q-z springs [22]

Diagrams for p-y, t-z, and q-z springs in different levels are shown in Figure 7 to Figure 12, based on the geotechnical reports in north of Qeshm island and APIRP2 standard [22].

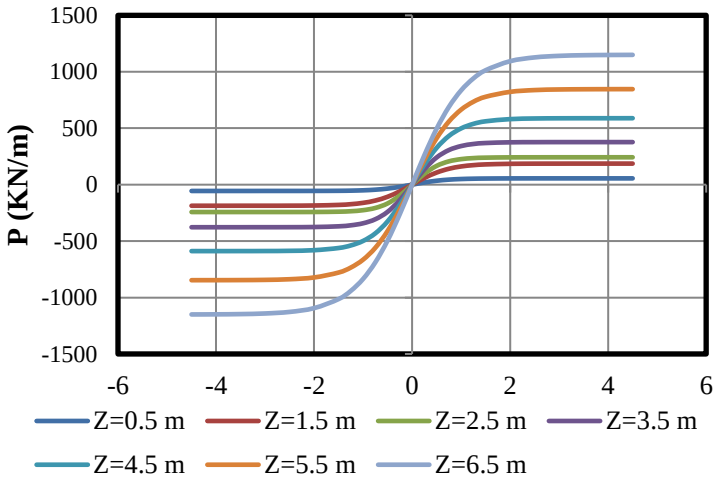


Figure 7. p-y diagram for sandy soil for 0<z< 7 from seabed.

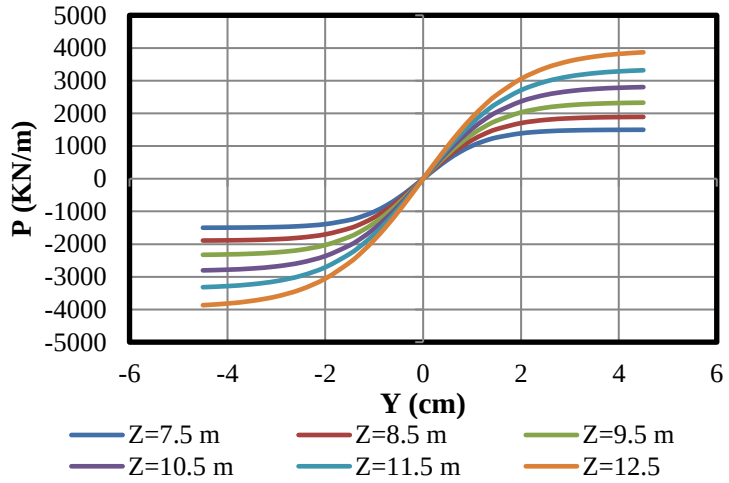


Figure 8. p-y diagram for sandy soil for 7<z<13 from seabed

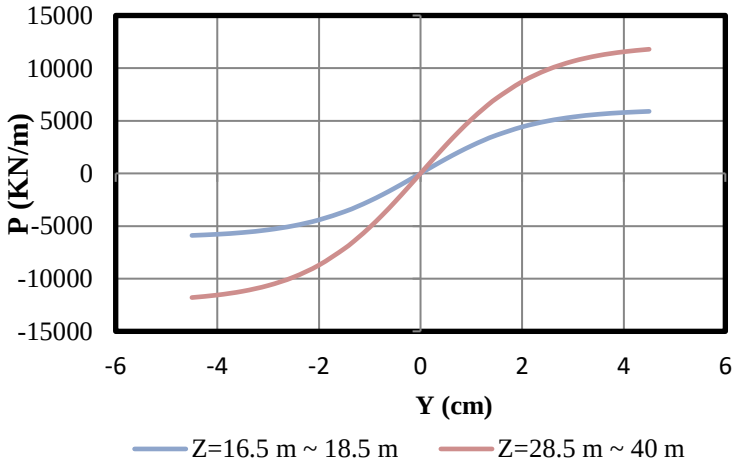


Figure 9. p-y diagram for sandy soil for z>13 from seabed.

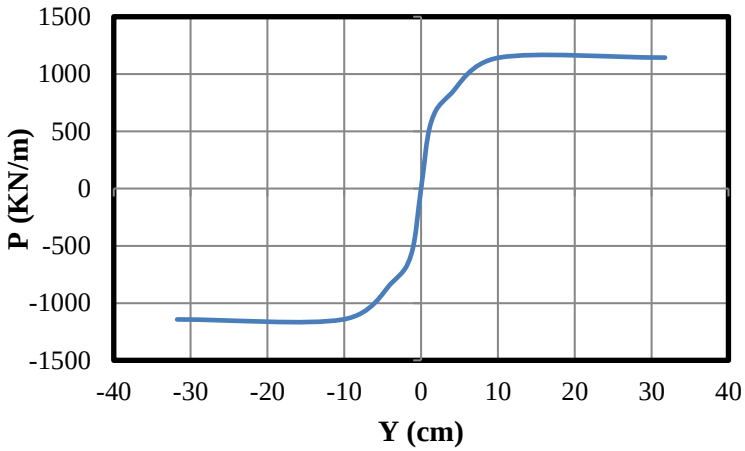


Figure 10. p-y diagram for clay.

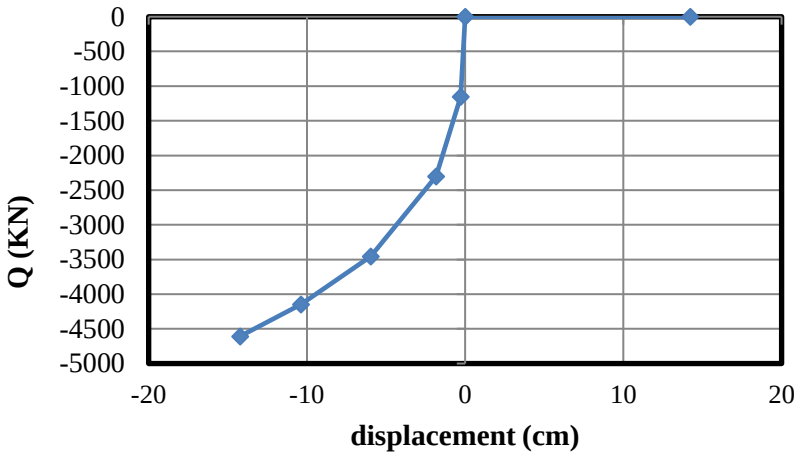


Figure 11. q-z diagram for sandy soil for 52" pile

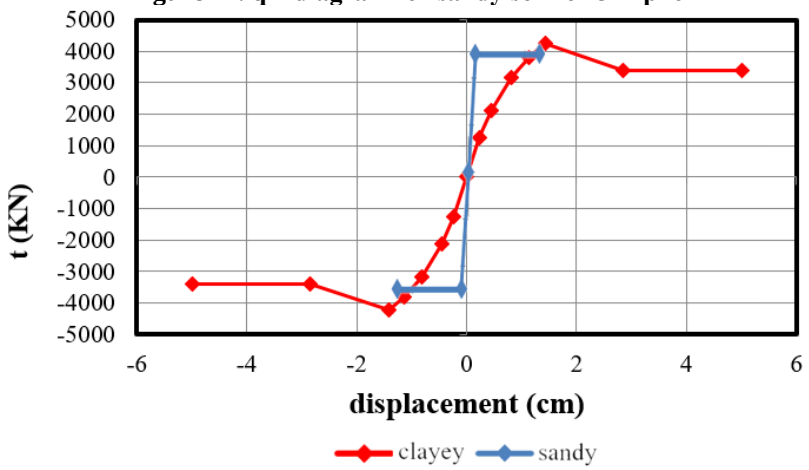


Figure 12. t-z diagram for sandy and clayey soil.

Pushover results with fixity point theory has been additionally analyzed. It should be noted that based on the OCDI recommendation, depth of fixity point is calculated as 5m as

3.3. Plastic Hinge and Acceptance Criteria

The definition and assignment of plastic hinges to steel pipe piles, as well as the criteria for failure of the hinges are considered based on the ASCE 61-14 standard [23]. As illustrated in Figure 13, the plastic hinges are defined as bilinear flexural hinges. Acceptance criterion for the joint according to the ASCE61-14 has been presented in Table 2. Additionally, the length of plastic joints according to ASCE 61-14 has been provided in Table 3.

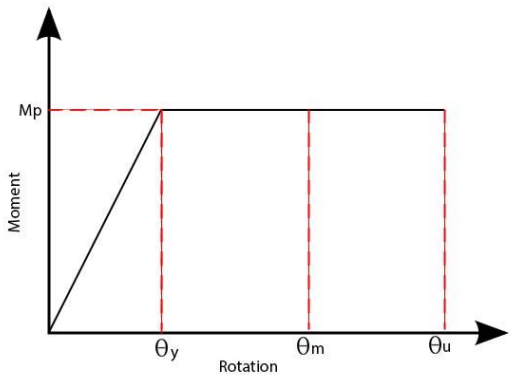


Figure 13. Flexural plastic hinge diagram for steel pile.

Table 2 - Plastic hinge acceptance criterion based on ASCE61-14 [23]

		Hinge location		
Pile type	**Component**	**Top of pile**	**In ground**	**Deep in ground (>10D_p)**
Solid concrete pile	Concrete	No limit	$\varepsilon_c \le 0.005 + 1.1\rho_s \le 0.012$	No limit
	Reinforcing steel	$\varepsilon_s \le 0.8\varepsilon_{smd} \le 0.08$		
	Prestressing steel		$\varepsilon_p \le 0.035$	$\varepsilon_p \le 0.050$
Hollow concrete pile[a]	Concrete	$\varepsilon_c \le 0.008$	$\varepsilon_c \le 0.008$	$\varepsilon_c \le 0.008$
	Reinforcing steel	$\varepsilon_s \le 0.6\varepsilon_{smd} \le 0.06$		
	Prestressing steel		$\varepsilon_p \le 0.025$	$\varepsilon_p \le 0.050$
Steel pipe pile	Steel pipe		$\varepsilon_s \le 0.035$[b]	$\varepsilon_s \le 0.050$
	Concrete	No limit		
	Reinforcing steel	$\varepsilon_s \le 0.8\varepsilon_{smd} \le 0.08$		

Table 3 - Plastic hinge length according to ASCE 61-14[23

Connection type Steel pipe piles	L_p at deck (in.)
Embedded pile	$0.5D$ (see Section 7.4.3.3)
Concrete plug	$0.30f_{ye}d_b$
Isolated shell	$0.30f_{ye}d_b + g$
Welded embed	$0.5D$ (See Section 7.4.2.4)
Welded dowels	NA
Prestressed concrete piles	
Pile buildup	$0.15f_{ye}d_b \le L_p \le 0.3f_{ye}d_b$
Extended strand	$0.2f_{pye}d_{st}$
Embedded pile	$0.5D$ (see Section 7.4.2.1)
Dowelled	$0.25f_{ye}d_b$
Hollow dowelled	$0.2f_{ye}d_b$
External confinement	$0.30f_{ye}d_b$
Isolated interface	$0.25f_{ye}d_b$

3.4. Evaluation of platform using vertical piled

The platform is firstly analyzed assuming supported by vertical piles, as a common practice in construction of marine oil platforms. According to the pushover analysis of the structure, as depicted in Figure 14, natural period of the structure and lateral elastic stiffness are 1.99 seconds and 3071.85 kN/m, respectively. The target displacement and base shear are 66cm and 1531 kN, respectively. The plastic hinges with minimum damage are located at the top of the piles. Investigations show that the structure passes acceptable resistance criteria, but is not within the acceptable displacement range. Accordingly, this study focuses on examining the effect of using SMA dampers to reduce displacement.

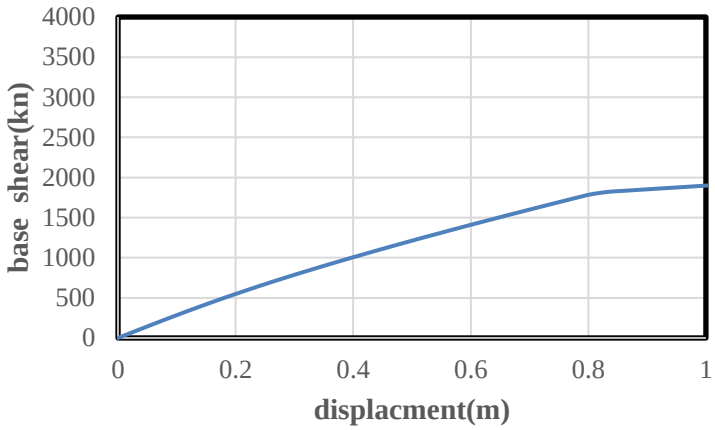


Figure 14. Pushover diagram for the platform with vertical piles.

3.5. Evaluation of platform with combination of vertical and batter piles

Batter piles with slope of 1:6, diameter of 1.3 meters, and thickness of 19 millimeters, are added to the platform, as a common remedy to reduce lateral displacement. 2D elevation of the platform is shown in Figure 15**.**



Figure 15. Schematic combination of vertical and batter piles in platforms.

Based on the pushover analysis, as depicted in **Figure *16***, the target displacement and base shear in this case are 0.215 meters and 3059 kN, respectively. The stiffness of the structure in this configuration is comprehensively higher than the previous case (only vertical piles). Accordingly, the target displacement has been reduced by 1/3 in comparison with the previous case. To obtain a similar displacement without batter piles, its necessary to add several vertical piles to the previous model that is economically unreasonable.

In contrast to the minimal displacements, the high lateral stiffness of the case of direct connection of batter piles to the deck is a major drawback of this system. Because it leads to dramatically increase the seismic demand level of earthquakes. The force in the batter piles during earthquakes can result in buckling, pull out from soil, and damage to the deck, similar to the Chile earthquake. Moreover, from geotechnical perspective, the significant axial force in the batter piles leads to excessive pile penetration into the soil or large number of piles.

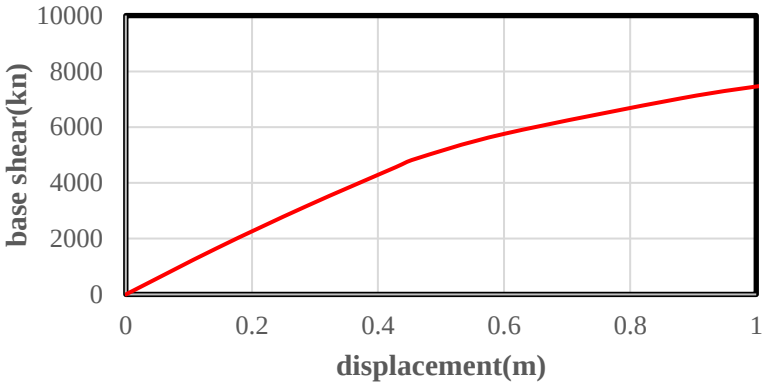


Figure 16. Pushover diagram for the platform with combination of vertical and batter piles.

4. Proposed SMA damper system

In this study, to simultaneously reduce both the seismic demand lateral displacement of the platform, a system of vertical and batter piles with SMA damper is evaluated, as depicted in Figure 17.

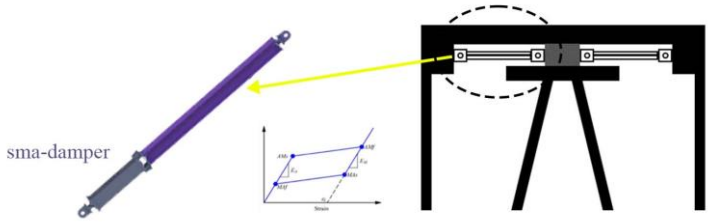


Figure 17. Schematic presentation of platform supported by vertical and batter piles, equipped with SMA dampers.

A multi-linear ideal model is used to represent the behavior of the phases of the shape memory alloy, in this study. For modeling shape memory alloy (SMA) dampers in SAP2000 software, two links should be defined. The first link is used to model elastic behavior, and the second link is a pivot type to consider cyclic behavior of SMA. Material properties of SMA damper, as described in Figure 3, is summarized in Table 4.

Table 4 - Mechanical Specifications of Shape Memory Alloy (SMA)

Mechanical Specifications	Value
Elastic modulus (Austenite and Martensite)	55 GPa
Superelastic strain	6%
Starting stress (Austenite to Martensite)	420 MPa
End stress(Austenite to Martensite)	520 MPa
Starting stress (Martensite to Austenite)	320 MPa
End stress (Martensite to Austenite)	240 MPa

To validate SMA modeling in SAP2000, a single element with an SMA link with the material properties of Table 4 has been modeled, as depicted in Figure 18. The resulted force-displacement diagram is shown in Figure 19, which represents the behavior of the flag-shaped SMA actuator.

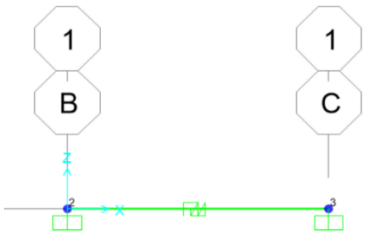


Figure 18. Modeling SMA link in SAP2000

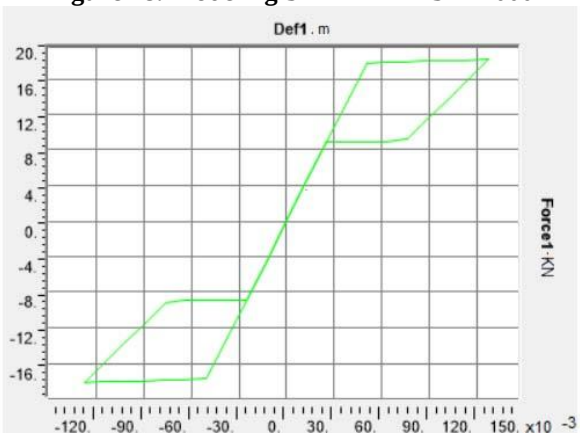


Figure 19. Flag-Shaped force-displacement for SMA damper in SAP2000

The results of the pushover analysis of the platform with SMA damper is shown in Figure 20. The target displacement and base shear for the system with SMA actuator are 21.5 cm and 1236 kN, respectively. As can be seen in this figure, lateral displacement and base shear during the earthquake is considerably reduced with the proposed structural system.

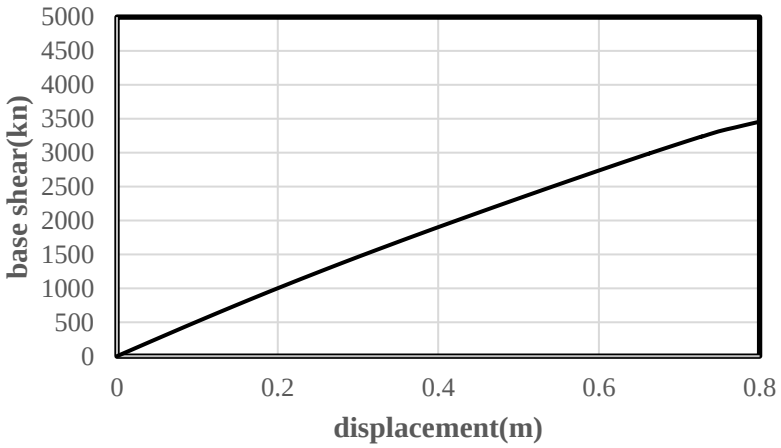


Figure 20. Pushover diagram of the platform with SMA actuator.

Table 5 compares lateral displacement and base shear of the following systems:

Case 1: Only vertical piles

Case 2: Combination of vertical and batter piles as depicted in Figure 15

Case 3: The proposed system with SMA damper as depicted in Figure 17

Comparing the mentioned systems, it can be concluded that the platform equipped with SMA dampers have been able to significantly control lateral displacement and base shear by dissipating the seismic input energy, as a main objective of the present study. For example, the minimum base shear is recorded in SMA system (1236kN) that is 80% and 40% of the base shear in cases 1 and 2, respectively. Similarly, the target displacement of 21.5cm in platform with SMA dampers is analogous to the system with batter piles which is 33% of the case 1. Additionally, no buckling and plastic hinges are seen in the piles.

Table 5. Comparison of pushover results in platform for different structural systems

type model	Effective period(s)	Effective stiffness (kN)	Target displacement (m)	Base shear (kN)
case 1	1.99	3071.85	0.66	1531
case 2	1.797	6387.31	0.215	3059
case 3	1.27	4775.36	0.215	1236

To provide a better comparison between SMA and other types of dampers, a system with friction damper is additionally evaluated. This system is modeled similarly to the viscoelastic dampers, and the FRICRTION link element with specification in Table 6 is employed.

Table 6. Friction damper specifications.

Friction Damper Model	Effective Damping	Shear Force (kN)
FR280	20%	80

The results of the pushover analysis for platform equipped with friction dampers is shown in Figure 21. The target displacement and base shear for the system are 24.5 cm and 1766.5 kN, respectively. The displacement and base shear of the system with friction damper are 14% and 43% more than SMA dampers, that indicate the superiority of the SMA over the friction damper.

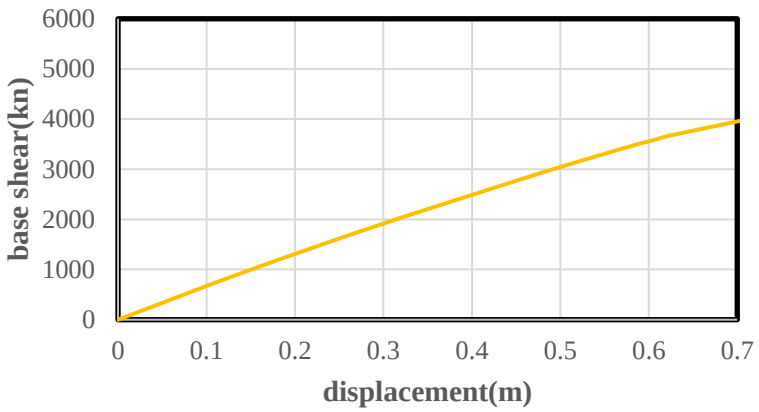


Figure 21. Pushover diagram for platform equipped with friction dampers.

5. Dynamic Analysis

To further investigation and more accurate conclusions, time history analysis is conducted on the platform in three scenarios (as discussed in Table 5) using the seismic acceleration record of Qeshm earthquake, as shown in Figure 22. Figure 23 and Figure 24 compare displacement and base shear, respectively, in different cases described in Table 5.

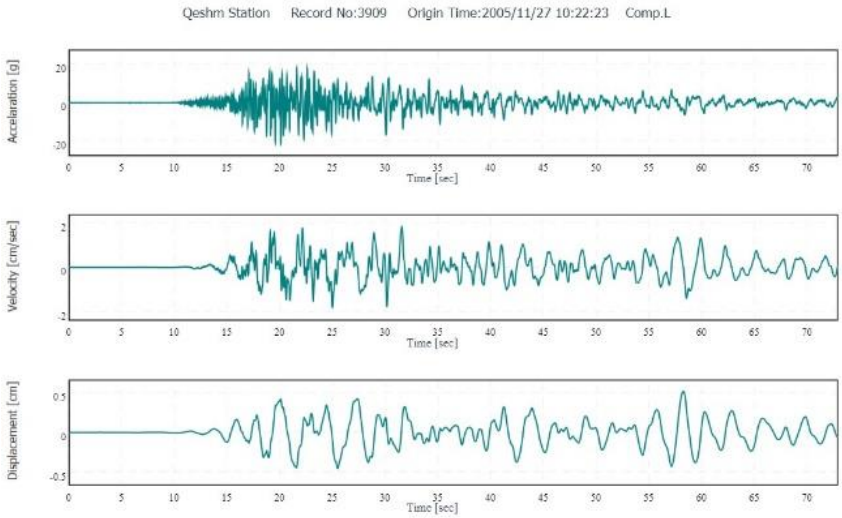


Figure 22. Time history of seismic record of Qeshm earthquake (2005)

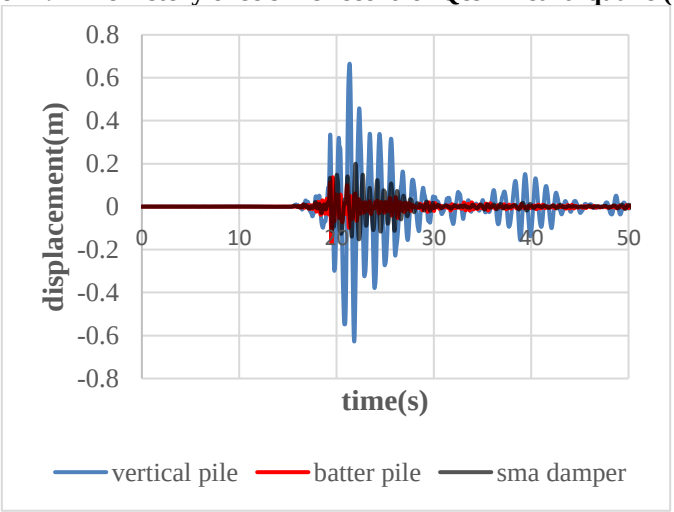


Figure 23. Comparison of displacement in the platform for different systems under Qeshm earthquake

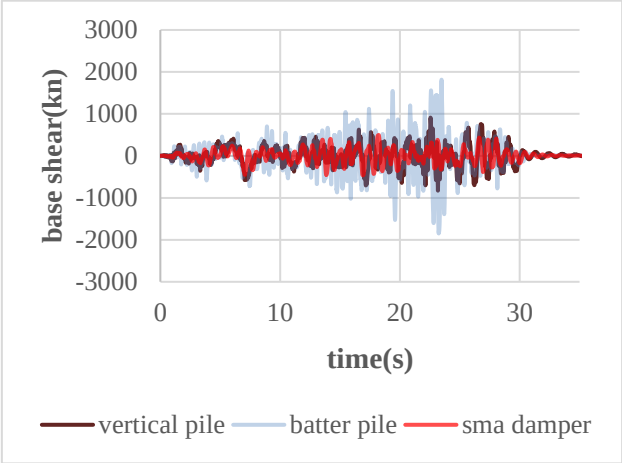


Figure 24. Comparison of base shear in the platform for different systems under Qeshm earthquake

To evaluate the capability of the SMA damper under other time histories, displacement and base shear of the structure under Manjil earthquake is shown in Figures *Figure 25* and *Figure 26*, respectively.

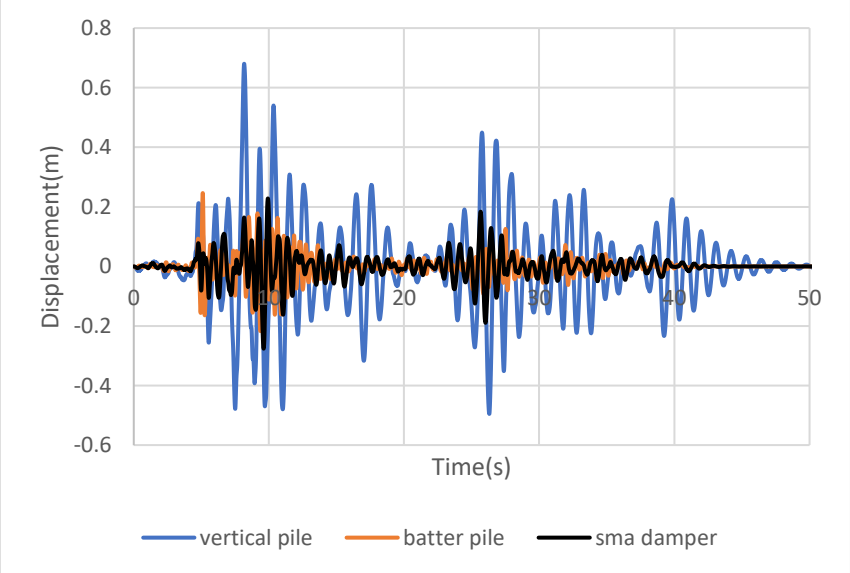


Figure 25. Comparison of displacement in vertical, batter and SMA dampers under Manjil earthquake.

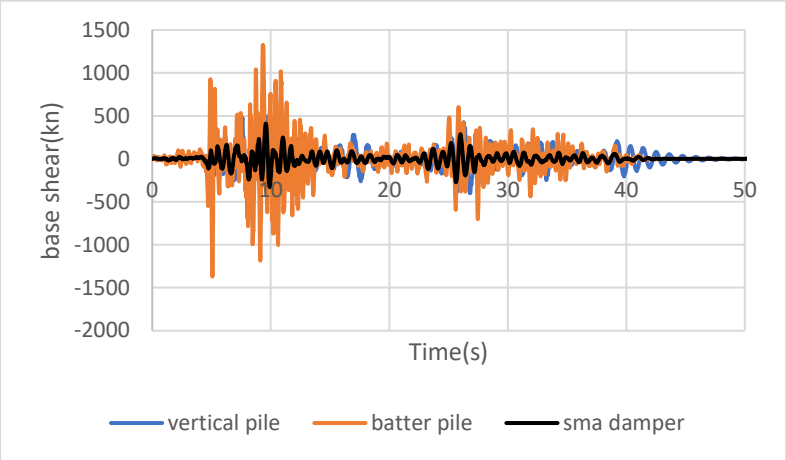


Figure 26. Comparison of base shear in vertical, batter and SMA dampers under Manjil earthquake.

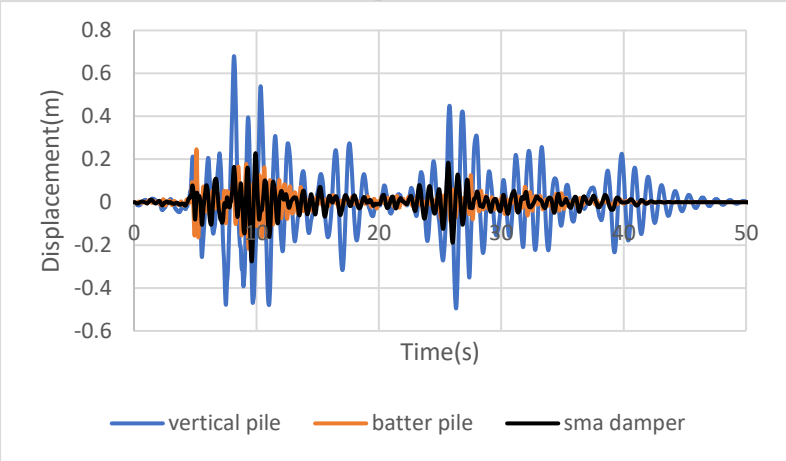


Figure 27. Comparison of displacement in vertical, batter and SMA dampers under Manjil earthquake.

Table 7 presents the seismic parameters obtained from dynamic analysis for different cases (vertical pile, batter piles and SMA systems), under the Qeshm earthquake record. As can be seen in this table, approximately the same results of the static pushover analysis has been achieved. Accordingly, it can be concluded that SMA dampers have led to reduction in displacement (comparable to the results of batter pile systems), and base shear in the proposed system is lower than both common systems of vertical piles and hybrid batter/vertical piles.

Table 7. Maximum displacement and base shear resulted from time history analysis under Qeshm record

Case	Maximum Displacement (m)	Base Shear (kN)
Case 1	0.71	912
Case 2	0.21	1850
Case 3	0.26	596

6. Fixity point theory

Pushover result have been additionally derive based on the fixity point theory in *Figure 28*. As can be seen in this figure, both p-y and fixity point theory are compatible. The hinge pattern based on the fixity point theory for different drifts are shown in Figures 29-31.

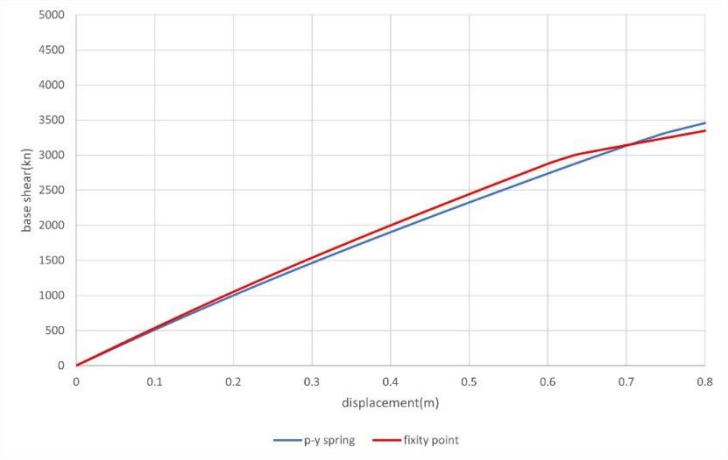


Figure 28. Comparison of pushover results for sma damper between fixity point theory and nonlinear P-Y spring.

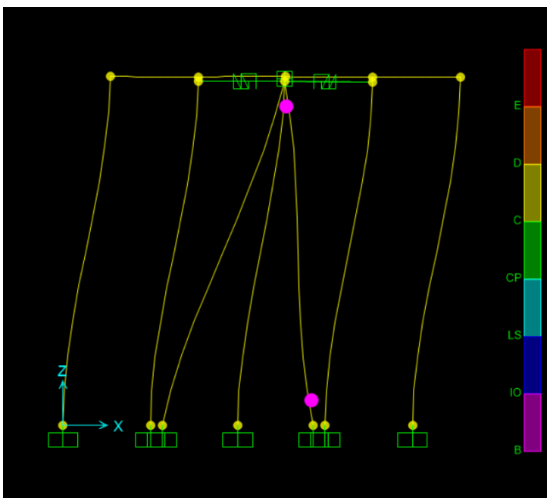


Figure 29. Hinge pattern for drift 42.6mm.

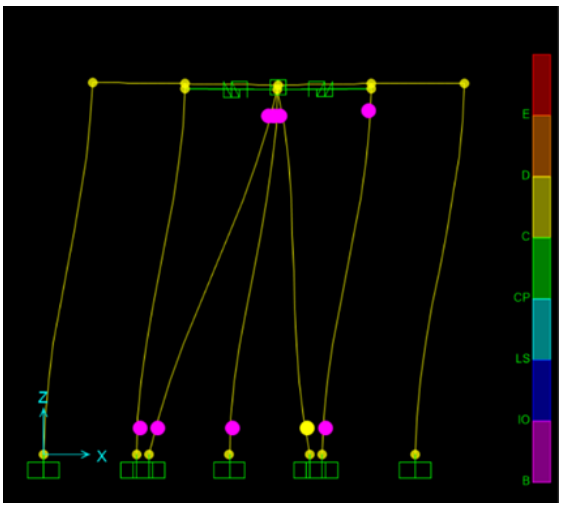


Figure 30. Hinge pattern for drift 110 mm.

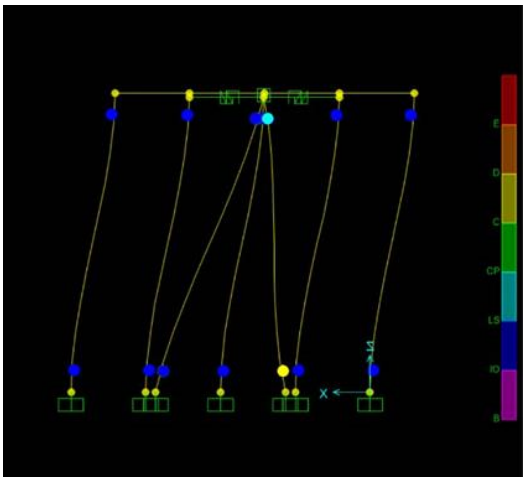


Figure 31. Hinge pattern for drift 208 mm.

7. Conclusion

In this study, a real case of operational platform in Qeshm island with two common pile and deck systems have been examined. In the first system, concrete superstructure is supported by vertical piles. In this case, a desirable flexibility and base shear were obtained, however, considerable resulted displacement was beyond acceptable range of serviceability of the structure. In contract, in the second system with hybrid vertical and batter piles, lower displacement (in acceptable range) with much more base shear (with undesirable failure mechanisms) were observed.

In this research, as an alternative, a system with SMA dampers was proposed to reduce both lateral displacement and base shear in the platform. The results revealed that the SMA damper considerably reduced the lateral displacements and base shear of the platform. Specifically, the following conclusion can be highlighted:

1. Displacements in the platform supported by the (only) vertical piles is in range 60-80cm, which is quite out of acceptable range of serviceability of the structure. Additionally, the base shear in this condition is approximately 1500 kN.
2. By adding batter piles to the platform, the displacement, approximately, is reduced by 70%, which was suitable according to the recommendations. However, in this condition, the undesirable failure mechanisms is seen, with the base shear more than double of the previous case.
3. Proposed system with SMA damper resulted in 59% reduction in base shear compared to batter pile system, and a 67% reduction in displacement compared to the vertical pile configuration. This result shows superiority of SMA damper systems over traditional lateral force systems.

Finally, comparing the SMA with friction dampers, the results show better performance of SMA over friction dampers.

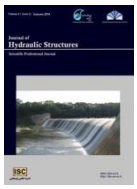
References

1. Seismic Design Guidelines of Wharves and Piers, Ministry of Road and Transportation Transportation Research Institute
2. Seismic Design Guidelines for Port Structures, Working Group No. 34 of the Maritime Navigation Commission International Navigation Association (pianc)
3. SEAOC (1991), "Reflections on the October 17, 1989 Loma Prieta Earthquake," Ad Hoc Earthquake Reconnaissance Committee, Sacramento
4. COPRI Chile Earthquake Investigation Team. (2013, June). Chile earthquake and tsunami of 2010: performance of coastal infrastructure. American Society of Civil Engineers
5. Roozbeh Amirabadi and Dr. Khusrow Barghi, Investigation of the Behavior of Pile and Deck Structures under Cyclical Lateral Loading
6. Ghiasian, M. , Fakher, A. , & Khanmohammadi, M. Enhancing the seismic performance of batter piles in pile-supported wharves using fluid viscous dampers. [In Persian]
7. Komachi, Y. , Tabeshpour, M. R. , Golafshani, A. A. , & Mualla, I. (2011). Retrofit of Ressalat jacket platform (Persian Gulf) using friction damper device. Journal of Zhejiang University-Science A, 12(9), 680-691.
8. Paul, S. , Datta, T. K. , & Kapuria, S. (2009). Control of fixed offshore jacket platform using semi-active hydraulic damper. Journal of Offshore Mechanics and Arctic Engineering, 131
9. Golafshani, A. A. , & Gholizad, A. (2009). Friction damper for vibration control in offshore steel jacket platforms. Journal of Constructional Steel Research, 65(1), 180-187.
10. Boroschek, R. L. , Baesler, H. , & Vega, C. (2011). Experimental evaluation of the dynamic properties of a wharf structure. Engineering Structures, 33(2), 344-356.
11. Shabankare, m. a. , Ketabdari, m. j. , & Arabzadeh, h. (2010). Evaluation of seismic operation of pile and deck wharves (case study: south pars petrochemical port wharves). [In Persian]
12. Memari, M. , Fakher, A. , & Mirghaderi, S. R. Improvement of seismic performance of wharves including batter piles
13. Naghdi, Mehrdad, 2015, "Seismic Analysis of Pile Wharves and Decks with the Aim of Improving the Performance of Inclined Piles," Master's Thesis, Supervisor: Fakher, Ali, University of Tehran.
14. Kilborn, J. , Harn, R. , & Firat, Y. (2010). Seismic retrofit of piers supported on battered piles using lead-rubber bearings. Ports 2010: Building on the past, respecting the future, 71-80.
15. Ou, J. , Long, X. , Li, Q. S. , & Xiao, Y. Q. (2007). Vibration control of steel jacket offshore platform structures with damping isolation systems. Engineering Structures, 29(7), 1525-1538.
16. Leal, J. , De La Llera, J. C. , & Aldunate, G. (2013). Seismic isolators in pilesupported wharves. In Ports 2013: Success through Diversification (pp. 590-599).
17. Mahdavi J, aghakouchak A, komakpanah A. Improving Seismic Performance of Pile Supported Wharves Using Seismic Isolators. Marine Engineering 2013; 8 (16) :79-93
18. Seyyed Hossein Hosseini, Mohammad Taher Kamali, Farshad Nasiri Minab. "Improving the Seismic Behavior of Pile Wharves and Decks Using Inclined Piles and Seismic Isolators - A Case Study on the Sirik Port Wharf."
19. Shahin Zareie, Mohammadjavad Hamidia, Abolghassem Zabihollah, Rafiq Ahmad, Kiarash M. Dolatshahi, Design, validation, and application of a hybrid shape memory alloy-

magnetorheological fluid-based core bracing system under tension and compression, Structures, Volume 35, 2022 [In Persian]
20. Zhang, J. , Ma, Z. , Liu, F. , Zhang, C. , Sharafi, P. , & Rashidi, M. (2017). Seismic performance and ice-induced vibration control of offshore platform structures based on the ISO-PFD-SMA brace system. Advances in Materials Science and Engineering, 2017.
21. Antonio concilio, Vincenza antonucci, Ferdinando auricchio, leonardo lecce, Elio sacco,shape memory alloy engineering For Aerospace, Structural, and Biomedical Applications, Second Edition
22. "Principles of Soil-Structure Interaction" authored by Dr. Ali Ghanbari (Professor at Kharazmi University)
23. Prestandard and Commentary for the seismic rehabilitation of buildings, american society of civil engineers reston, virginia and shima al sadat hosseini tehran.

© 2025 by the authors. Licensee SCU, Ahvaz, Iran. This article is an open access article distributed under the terms and conditions of the Creative Commons Attribution 4.0 International (CC BY 4.0 license) (http://creativecommons.org/licenses/by/4.0/).

Journal of Hydraulic Structures
J. Hydraul. Struct., 2025; 11(1): 41-50
DOI: 10.22055/jhs.2024.47215.1304



OPEN ACCESS

Spiral Flow Measurement at Vertical Intakes Using PTV Method

ShahWali Hamidi[1]
Hamed Sarkardeh[1*]
Ali Bashtani[1]

Abstract

In order to study the characteristics of the different formed free surface vortices at vertical hydraulic intakes, three sets of experiments were conducted. The spiral flow was detected using the Particle Tracking Velocimetry (PTV) measurement technique in three dimensions (3D) by installing two cameras at above and side of the model. The dimensions of model were 2000mm in length, 1300mm in width and 1500mm in height. Through the experiments, extensive data including tangential (V_θ), radial (V_r) and axial (V_z) velocities and their variations with the changing vortex center in different vortex classes, were recorded and analyzed. Using the obtained results, a 3D flow path was drawn for each class of the formed vortex. Moreover, changes in the diameter of the vortex core (D_{vo}) in the three different classes of vortex were investigated and its changes along the vortex axis were measured. Results showed that the average of D_{vo}/D (D is the intake diameter) was about 0.14, 0.2 and 0.23 for vortices Class C, B and A, respectively.

Keywords: Spiral Flow; Free Surface Vortex; Vertical Intake; PTV Method; Vortex core diameter.

Received: 24 June 2024; Accepted: 10 September 2024

Notations

D: intake diameter
Fr: intake Froude number = $V/(gD)^{1/2}$
g: gravitational acceleration
Q: intake discharge
Re: intake Reynolds number = VD/υ
r: radial distance from the vortex center
S: submergence of the intake centerline
S/D: relative submergence of the intake

*Email: sarkardeh@hsu.ac.ir
[1]Department of Civil Engineering, Hakim Sabzevari University, Sabzevar, Iran.

CC BY

We: intake Weber number = $\rho V^2 D/\sigma$
ρ: density of water
σ: surface tension of water
v: kinematic viscosity of water
V_θ: tangential velocity component
V_r: radial velocity component
V_z: axial velocity component
Z/s: relative depth
D_{vo}: diameter of the vortex core

1. Introduction

The occurrence of free surface vortex in reservoirs is a common and damaging event, posing a significant challenge in hydraulic engineering for intake design. The impact of these vortices can lead to severe damage to the hydraulic structures, especially hydraulic machinery, due to sudden pressure changes and shocks. This can result in inducing vibrations, noise pollution, decreasing the operational efficiency of hydraulic equipment, and moving debris and sediments into the intake. Forming air-core vortices can disrupt the expected forces on turbine blades, reducing power plant performance and increasing hydraulic losses during power generation [1-3]. Sarkardeh et al. categorized free surface vortices into three classes based on their strength and associated risks [4]. Class C represents weak and safe rotations, while Class B involves flow rotation reaching the intake and dragging debris. Class A denotes the strongest vortices that should be avoided, where air bubbles are trapped and drawn down to the intake. In the most intense state, a stable air-core forms at the vortex center, steadily drawing air into the intake (Figure 1).

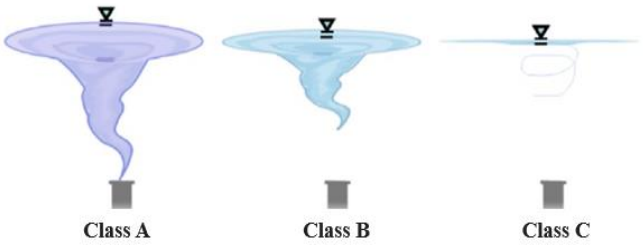


Figure 1. Classification of vortices based on their strength [4]

Some performed researches in the recent years, making significant contributions to the progress of knowledge in the field of hydraulic engineering. Sarkardeh and Marosi analytically recognized and analyzed the spiral flow motion of the free surface vortices at intakes [5]. Azarpira and Zarrati [6] created a precise computational model designed for the analysis of 3D air-core vortices. Suerich-Gulick et al. introduced a model for predicting the fundamental attributes of free surface vortices at intake [7,8]. Wang et al. [9] have conducted various studies on the evolution of vortices. Recently, numerical simulations have a significant effect on exploring different characteristics and aspects of free surface vortices at intakes [10-17]. Pakdel et al. conducted a numerical study to examine the impact of waves on vortices that are generated in vertical intakes [18-19]. Zi et al. [20] investigated formation and development mechanism of the air-core vortex situated between the free surface and the horizontal flow intake. Many aspects of vortex formation were discovered through the use of physical models [21-27]. Monshizadeh et al. and Tahershamsi et al. conducted a comparative study and analysis on

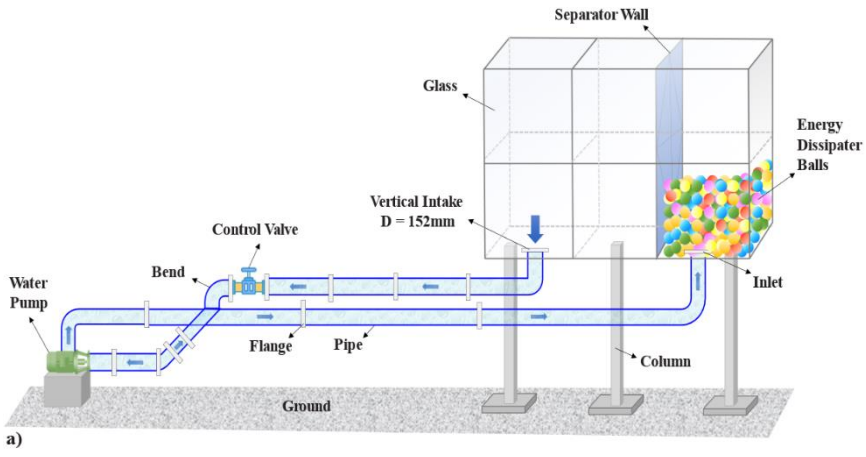
dynamic of a formed free surface vortex at horizontal intakes and also a hydraulic method on dissipating formed vortices [28-32]. Aghajani et al. investigated the effect of a trash rack at the entrance of intake on strength of formed vortices using an experimental model [33,34]. Amiri et al. investigated methods for preventing vortices by various anti-vortex plates [35]. Camnasio et al. conducted an experimental investigation on the velocity distributions within rectangular shallow reservoirs using ultrasound profiling. They aimed to assess how the reservoir geometry influences the flow patterns [36]. In an experimental study, Sarkardeh et al. [37] investigated the 3D components of velocity using an Acoustic Doppler Velocimetry (ADV) device in a reservoir with a horizontal intake. Suerich-Gulick et al. [8] have utilized Particle Image Velocimetry (PIV) to analyze the vortex flow field.

Although a large number of studies were conducted in the field of vortex recognition to date, there are still many problems to be solved due to the complexity of the vortex. The purpose of this study is to utilize the PTV technique to visualize the spiral flow and determine the 3D velocity components in different free surface vortices. In the present research, by employing a big experimental model, V_θ, V_r and V_z were determined using the PTV technique. Regarding the measured different velocity components, 3D spiral flow path line was drawn for three different classes of vortices. Moreover, diameter variations of the vortex core in each class were also recorded and analyzed.

2. Methods and Materials

2.1. Experimental setup

The used physical model consisted of a metal structure with 10mm thickness glass walls to provide a clear view of the reservoir sides and bottom [38]. The reservoir had dimensions of 2000mm in length, 1300mm in width, and 1500mm in height, with water capacity of approximately 4m³ . To minimize the scale effects, Reynolds (*Re*) and Weber (*We*) should be greater than a value which suggested by the different researchers to neglect the effects of viscosity and surface tension. Considering the effects of viscosity and surface tension in vortex modeling and creating scale errors, by summarizing the opinions of different researchers and maintaining the appropriate margin of safety in model design, *Re* and *We* should have a value greater than $Re \geq 1.1 \times 10^5$ and $We \geq 720$ [38]. The reservoir length was 2000mm to ensure undisturbed flow to the test area after passing through flow energy dissipaters (Figure 2).



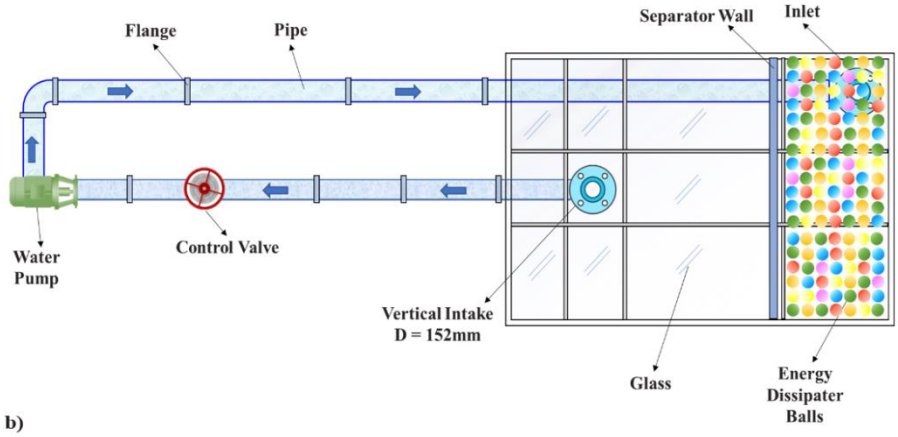


Figure 2. Side Schematic view (a), top schematic view (b)

2.2. Measurement technique

To prevent interruption in the flow, the PTV method was utilized to measure the 3D velocity distributions and plot the spiral flow path lines. In this system, a pair of 5-megapixel cameras was utilized, capable of recording videos at a frame rate of 25 fps. The importance of using these types of cameras was ability of synchronizing when recording starts and ends. In this investigation, because of low speed of motion, the tracer particles can be easily identified without the need for high image resolution and also high frame rate of camera. By installing an up view camera on the base of the tank, images related to the x-y coordinate plane can be recorded. By utilizing the camera positioned on the ground base, side-view images can be captured in the x-z coordinate plane. Two cameras can simultaneously send the recorded images to the Digital Video Recorder (DVR) device for storage. The images recorded on the DVR can be reviewed on the monitor and exported as video files for further processing (Figure 3).

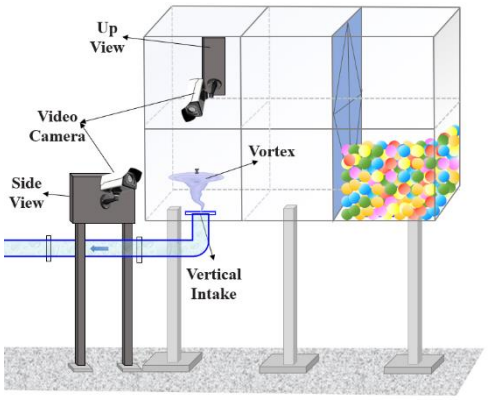


Figure 3. Imaging equipment

2.3. Experimental procedure

In this research, three classes of vortices are formed by adjusting the flow rate of the pump connected to the reservoir. Three different flow rates result in the generation of vortices in three

classes of C, B, and A, at a constant relative submerged depth (*S*/*D*). In order to create a stable vortex at the entrance of the vertical intake, each test required a minimum time of 15 minutes to establish stable conditions. After establishing stable conditions in each vortex class, a tracer particle was released into the test area in the reservoir, and its movement is recorded in the x-y and x-z coordinates. The recorded videos were divided into the frames. In this case, the spiral flow path line is drawn for each vortex class, and the 3D velocity parameters were determined based on the center of the formed vortex. The PTV method consists of several key steps. First, the tracer particle images acquired in each recording must be analyzed by removing any disturbing backgrounds. After that, the position of each particle must be determined with high accuracy at any time. The subsequent stage entails associating particle images that related to the same physical tracer, usually by identifying the image pair with the shortest distance as the accurate match. In the next step, by grouping the specified points into specific time intervals, it is possible to draw the spiral flow lines and determine the 3D velocity parameters. The PTV method offers several advantages. First, the velocity data obtained is relatively accurate because each velocity vector corresponds to the image of a particle. This characteristic guarantees that measurements remain unaffected by bias errors resulting from spatial averaging [39].

3. Results and Discussions

3.1. Vortex appearance at the intake entrance

The physical model used in this study was capable of simulating all three classes of vortices in terms of strength (Figure 4). Therefore, the physical model was capable to generate flows with varying *Fr* for a constant depth of water in the reservoir. By increasing the flow rate of the pump in the physical model, *Fr* was increased in a constant reservoir water level, leading to the change of the vortex from Class C to Classes B and A. Increasing *Fr* results in the formation of stronger vortices in the laboratory model [4].



Class A **Class B** **Class C**

Figure 4. Vortex formed in the physical model [38]

By forming vortices in three different classes (A, B and C), tracer particles (polystyrene tracer particles with a density similar to the water) were released into the intake area. Using image recording equipment, the trajectory of the tracer particle is visualized in two directions: up and side views of flow (Figure 5).

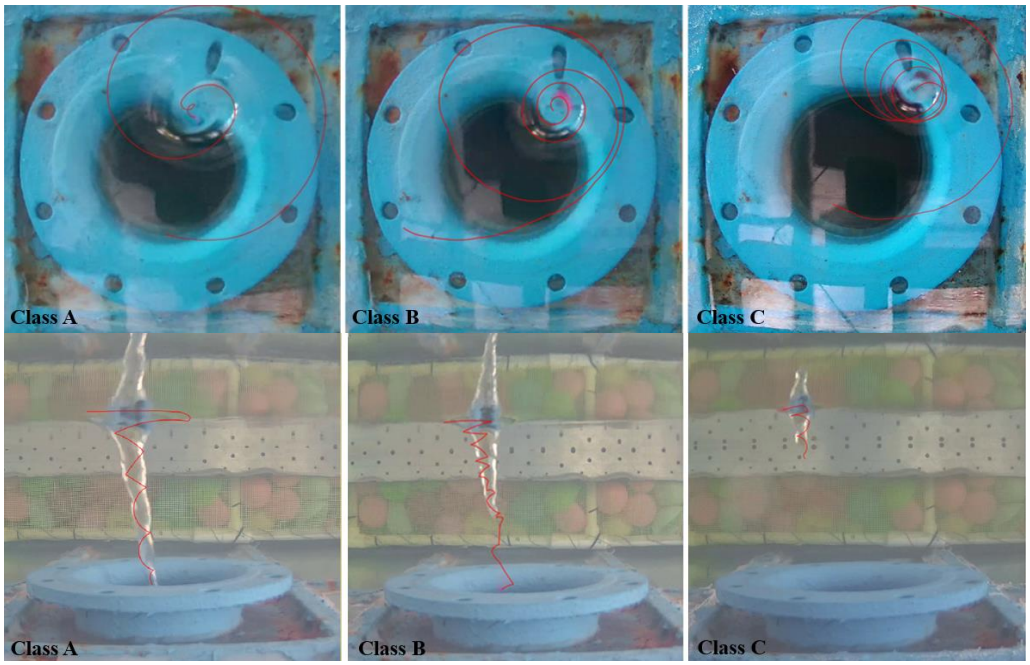


Figure 5. Tracer particle path in up and side views

3.2. Vortex core diameter variations

Figure 6 illustrates the variations in the funnel shape of the vortex across different classes, as well as the changes in the diameter of the vortex core.

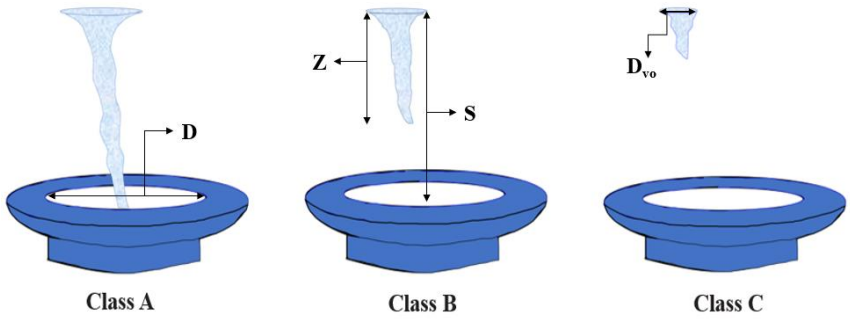


Figure 6. Schematic image of vortex core diameter in three vortex classes A, B and C

Based on the changes in the diameter of the vortex core along the vortex axis (Z) in relation to the intake submergence (s) and considering the Z/s criterion, the variations in the vortex core diameter were examined. The changes of D_{vo} in relation to D were also investigated. Results of D_{vo} changes along the three different formed classes of vortex indicate that Class A has the largest D_{vo} while Class C has the smallest D_{vo}. It is evidence that the maximum of D_{vo} occurs at Z/s = 1 and towards the intake decreases (Figure 7).

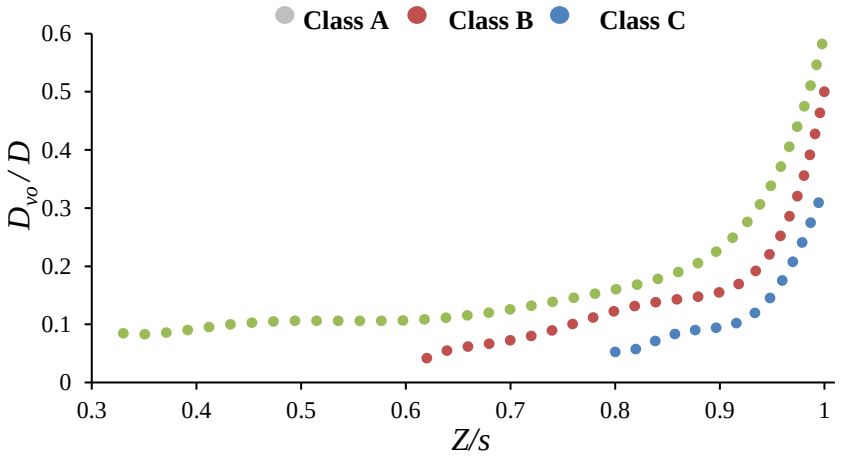


Figure 7. Changes in D_{vo} along the vortex axis at three different classes

The average of D_{vo}/D is about 0.14, 0.2 and 0.23 for vortices Class C, B and A, respectively. This trend demonstrates the impact of increasing the strength of the vortex on the diameter of the vortex core.

3.3. Drawing the spiral path lines

By drawing the flow paths regarding side and top views, three classes of vortex were determined. The output images from top view camera shows a surface spiral path. In Class A vortices, characterized by high flow rate and velocities higher than those of Classes B and C vortices, particles follow a shorter path. This causes their radius of movement to be decreased, rapidly, towards the center of the vortex. The difference in path lengths between Class C and B vortices can be attributed to the tracer particle position within the formed core in the Class C vortex, resulting in rotational movement. In Class A vortex, where there is a higher speed and flow rate than the other two classes of vortex, the tracer particle travels about 30% less distance than the tracer particles in Classes B and C vortices (Figure 8).

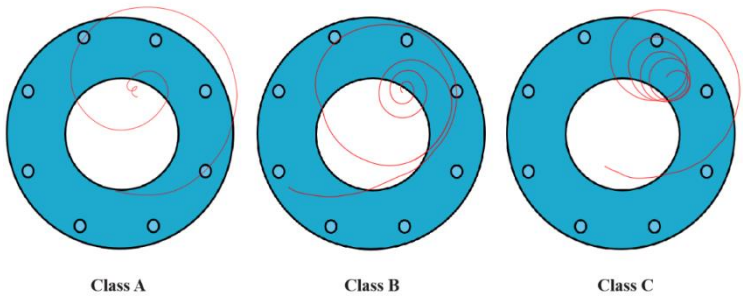


Figure 8. The path line of the tracer particle in an up view

Upon entering the radial range of the vortex, the tracer particles are attracted towards the center of the vortex and become visible in the output images captured by the vision camera positioned at the well side of the funnel-shaped path. In a Class A vortex, a stable air core is formed in the center of the vortex, trapping and transporting air bubbles from the water surface to the intake. Due to the presence of a strong air core in the center of the vortex, the tracer

particle travels a path that is 15% longer than the movement of the tracer particle in the Class B vortex. Figure 9 illustrates the rapid movement of the particle towards the intake in different vortex classes. The path traveled by the tracer particle in Classes A and B vortices is approximately twice as long as the path of the tracer particle in the Class C vortex (Figure 9).

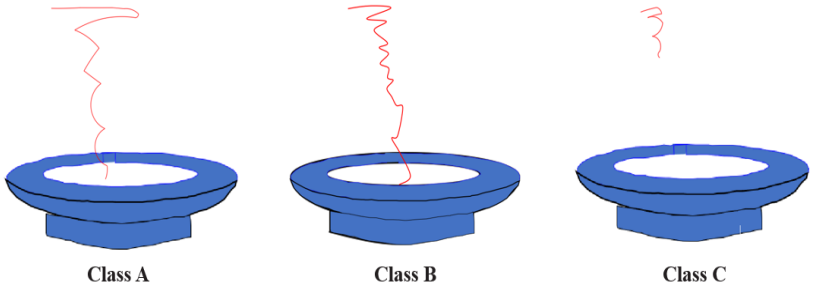


Figure 9. The path line of the tracer particle in a side view

4. Summary and Conclusions

In this study, a rectangular vortex tank with dimensions of 2000 mm in length, 1500 mm in height, and 1300 mm in width was utilized to examine the characteristics of the free surface vortex. The PTV method was used to measure the vortex flow field. In this study, the changes of D_{vo} and the flow path in different classes of vortices have been investigated. In this research, the impact of different vortex classes on flow paths was investigated using the PTV method. The tracer particle in a Class A vortex travels about 30% shorter than in Classes B and C vortex. Also, the tracer particle in the Class B vortex, which experiences more significant changes in radius compared to the Class C vortex, follows a path approximately same and eventually enters the center of the vortex. The tracer particle in Class C travels also same the particle path in the Class B vortex. Although the difference in path length is small, this path occurs over a longer period of time compared to the Class B vortex due to the lower flow velocity to the intake and the weaker strength of the vortex.

Conflict of Interest: The authors declare that they have no conflict of interest.
Availability of Data: The data that supports the findings of this study are available within the article.

References

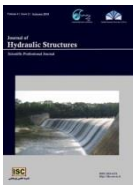
1. Lugt HJ (1983). Vortex Flow in Nature and Technology. J. Wiley.
2. Knauss J (1987). Swirling flow problems at intakes. Hydraulic Struc. Design Manual. Balkema.
3. Jorabloo M, Abdolahpour M, Roshan R, Sarkardeh H (2011). A techno-economical view on energy losses at hydropower dams (case study of Karun III Dam and Hydropower Plant). Computational Methods in Multiphase Flow VI. 70, 253.
4. Sarkardeh H, Zarrati AR, Roshan R (2010). Effect of intake head wall and trash rack on vortices, J. Hydraulic Research, 48(1): 108–112.
5. Sarkardeh H, Marosi M (2022). An analytical model for vortex at vertical intakes. *Water Supply* 22(1): 31-43.

6. Azarpira M, Zarrati AR (2019) A 3D analytical model for vortex velocity field based on spiral streamline pattern. Water Sci Eng 12:244–252.
7. Suerich-Gulick F, Gaskin SJ, Villeneuve M, Parkinson E (2014). Characteristics of free surface vortices at low-head hydropower intakes. J Hydraul Eng 140(3):291–299.
8. Suerich-Gulick F, Gaskin S, Villeneuve M, Parkinson É (2014c). Free surface intake vortices: Theoretical model and measurements. J. Hydraul. Res., 52(4), 502–512.
9. Wang Y, Jiang C, Liang D (2011a). Comparison between empirical formulae of intake vortices. Journal of Hydraulic Research, 49(1), 113–116.
10. Sarkardeh H, Zarrati AR, Jabbari E, Marosi M (2014). Numerical simulation and analysis of flow in a reservoir in the presence of vortex. Engineering Applications of Computational Fluid Mechanics. 8(4): 598-608.
11. Khadem Rabe B, Ghoreishi Najafabadi SH, Sarkardeh H (2017). Numerical simulation of air-core vortex at intake. CURRENT SCIENCE. 113(1): 141-147.
12. Sarkardeh H (2017). Numerical calculation of air entrainment rates due to intake vortices. Meccanica. 52: 3629-3643.
13. Khadem Rabe B, Ghoreishi Najafabadi SH, Sarkardeh H (2018). Numerical simulation of anti-vortex devices at water intakes. Proc. Inst. Civ. Eng. Water Manag. 171(18).
14. Esmaeilpoor E, Sarkardeh H, Jabbari E (2021). Numerical Study on Simultaneous Operation of Spillway and Power Intake. Journal of Dam and Hydroelectric Powerplant. 8(30), 33-42 (in Persian).
15. Taghizadeh AH, Sarkardeh H, Jabbari E (2023). Numerical study on effect of reservoir vortex on velocity distribution profile in pipe. The European Physical Journal Plus. 138(6), 521.
16. Mousavinia SH, Sarkardeh H, Jabbari E, Taghizadeh AH (2024). Performance of plate and perforated trashracks on vortex prevention at vertical intake. Meccanica. 59(4): 539-559.
17. Amini AA, Sarkardeh H, Jabbari E, Eidi A (2024). Understanding vortex characteristics in hydraulic systems: a temperature-driven analysis. Modeling Earth Systems and Environment, 1-13.
18. Pakdel E, Majdzadeh Tabatabai MR, Sarkardeh H, Ghoreishi Najafabadi SH (2020). Elimination of vortices by wave generation as a hydraulic anti-vortex method. J Braz Soc Mech Sci Eng 42(11):1–14.
19. Pakdel E, Sarkardeh H, Ghoreishi Najafabadi SH (2019). Numerical simulation of the effect of waves on the vortex formed in the vertical intake. Modares Civil Eng J. 19(5):59–71 (in Persian).
20. Zi D, Xuan A, Wang F, Shen L (2020). Numerical study of mechanisms of air-core vortex evolution in an intake flow. Int J Heat Fluid Flow 81:108517.
21. Khodashenas SR, Roshan R, Sarkardeh H, Azamatullah H (2010). Vortex study at orifice spillways of Karun 3 Dam, J. Dam Eng. 11:131–143.
22. Taghvaei SM, Roshan R, Safavi K, Sarkardeh H (2012). Anti-vortex structures at hydropower dams. Int J Phys Sci 7(28):5069–5077.
23. Azarpira M, Sarkardeh H, Tavakkol S, Roshan R, Bakhshi H (2014). Vortices in dam reservoir: a case study of Karun III dam. Sadhana 39(5):1201–1209.
24. Khanarmuei MR, Rahimzadeh H, Sarkardeh H (2015). Investigating the effect of intake withdrawal direction on critical submergence and strength of vortices. Modares Mechanical Engineering 14 (10), 35-42 (in Persian).
25. Khanarmuei MR, Rahimzadeh H, Kakuei AR, Sarkardeh H (2016). Effect of vortex formation on sediment transport at dual pipe intakes. Sadhana 41(9):1055–1061.

26. Sarkardeh H (2017). Minimum reservoir water level in hydropower dams. Chin J Mech Eng 30(4):1017–1024.
27. Khanarmuei MR, Rahimzadeh H, Sarkardeh H (2019). Effect of dual intake direction on critical submergence and vortex strength, Journal of Hydraulic Research, 57 (2), 272-279.
28. Monshizadeh M, Tahershamsi A, Rahimzadeh H, Sarkardeh H (2017). Experimental investigation of dynamics of the air-core vortices and estimating the air entrainment rate at a horizontal intake. Modares Mechanical Engineering. 17 (8), 59-67 (in Persian).
29. Monshizadeh M, Tahershamsi A, Rahimzadeh H, Sarkardeh H (2017). Comparison between hydraulic and structural based anti-vortex methods at intakes. The European Physical Journal Plus 132, 1-11.
30. Monshizadeh M, Tahershamsi A, Rahimzadeh H, Sarkardeh H (2018). Vortex dissipation using a hydraulic-based antivortex device at intakes. International Journal of Civil Engineering 16, 1137-1144.
31. Tahershamsi A, Rahimzadeh H, Monshizadeh M, Sarkardeh H (2018). A new approach on anti-vortex devices at water intakes including a submerged water jet. The European Physical Journal Plus, 133(4):143.
32. Tahershamsi A, Monshizadeh M, Rahimzadeh H, Sarkardeh H (2018). An experimental study on free surface vortex dynamics. Meccanica, 1-9.
33. Aghajani N, Karami H, Mousavi SF, Sarkardeh H (2019). Experimental study of the effect of the trashrack on the vortex at the intake of the hydroelectric power plants in various flow rates and submergence depths. Journal of Dam and Hydroelectric Powerplant, 6(21):49-62 (in Persian).
34. Aghajani N, Karami H, Sarkardeh H, Mousavi SF (2020). Experimental and numerical investigation on effect of trash rack on flow properties at power intakes. ZAMM-Journal of Applied Mathematics and Mechanics, 100(9).
35. Amiri SM, Zarrati AR, Roshan R, Sarkardeh H (2011). Surface vortex prevention at power intakes by horizontal plates. Proceedings of the Institution of Civil Engineers – Water Management 164(4): 193–200.
36. Camnasio E, Orsi E, Schleiss AJ (2011). Experimental study of velocity fields in rectangular shallow reservoirs. Journal of Hydraulic Research, 49(3), 352-358.
37. Sarkardeh H, Jabbari E, Zarrati AR, Tavakkol S (2014). Velocity field in a reservoir in the presence of an air-core vortex. Proc Inst Civ Eng Water Manag 167(6):356–364.
38. Bashtani A, Sarkardeh H (2022). Design of an Experimental Setup for Free Surface Vortex at Intakes (Including a Review on the Constructed Laboratory Models). *Journal of Hydraulic Structures*, *8*(2), 68-83.
39. Raffel M, Willert CE, Scarano F, Kähler CJ, Wereley ST, Kompenhans J (2018). Particle image velocimetry: a practical guide. springer.

© 2025 by the authors. Licensee SCU, Ahvaz, Iran. This article is an open access article distributed under the terms and conditions of the Creative Commons Attribution 4.0 International (CC BY 4.0 license) (http://creativecommons.org/licenses/by/4.0/).

Journal of Hydraulic Structures
J. Hydraul. Struct., 2025; 11(1): 51-64
DOI: 10.22055/jhs.2024.47500.1313



OPEN ACCESS

Dimensionless Equations for Hydraulic Jump Stilling Basins Downstream of Gabion Stepped Chutes

André Luiz Andrade Simões [1*]
Thaise Ithana de Souza França [1]
Luciano Matos Queiroz [1]
Iran Eduardo Lima Neto[2]
Harry Edmar Schulz[3]
Daniel Castro Hora Fontes[1]
Rodrigo de Melo Porto[4]

Abstract

Flows in stepped chutes built with gabions have been studied for about four decades and have found applications mainly in small dams and drainage systems. This paper presents a literature review of experimental studies on the subject, especially those that published data and methodologies for designing stepped chutes in gabions. A dimensionless methodology for predicting the main design variables is proposed, and equations were proposed for this purpose. These equations, based on physical principles and statistically supported, involve characteristics of stilling basins of hydraulic jump downstream of stepped chutes formed by gabions and the main quantities related to the design of these hydraulic structures. More than 160 data points were used, each of them involving several parameters of the adopted physical models, making the proposed methodology valid for five different slopes of the downstream face of the stepped chutes. The new equations allow for calculating the length and elevation of the stilling basin bottom. They also allow the determination of the supercritical depth at the basin inlet and the estimation of the height of the continuous end sill of the stilling basin. The proposed equations present strong correlations and adherence to the experimental data in the literature and reveal the missing data about the subject considering the existing literature. In addition, an application example illustrates the use of the developed methodology and compares the present results with those obtained from a methodology available in the literature.

Keywords: energy dissipation; gabion structures; hydraulic jump; stepped chutes; stilling basin.

[*]Email: andre.simoes@ufba.br
[1]Federal University of Bahia, R. Prof. Aristídes Novis, 2 - Federação, 40210-630, Salvador, Bahia, Brazil.
[2]Federal University of Ceará, Centro de Tecnologia, Departamento de Engenharia Hidráulica e Ambiental. Av. Mister Hull, Bloco 713 Pici 60451970 - Fortaleza, Ceará – Brasil.
[3] Auburn University, 238 Harbert Center, Auburn, Alabama, USA.
[4] University of São Paulo, USP, Av. Trabalhador Sãocarlense, 400 CP 359 São Carlos, SP CEP 13566-590, Brazil.

CC BY

Received: 24 July 2024; Accepted: 30 August 2024

1. Introduction

The understanding of flow characteristics in stepped spillways has advanced significantly over the past four decades, leading to an increase in the number of dams incorporating stepped chutes. This research has not only improved the design of larger structures but has also helped the development of smaller hydraulic structures, such as "water cascades" on steep terrains, drainage stairways, and decorative architectural features. Additionally, exploring alternative materials for constructing small dams with stepped spillways has promoted the use of gabions, which offer stability and substantial energy dissipation, as noted by [1].

Considering the study of gabions as porous/permeable materials to build weirs, several studies considering only one step, or, in other words, a weir using only one gabion, may be found in the literature. These studies involve general characteristics of the flows, like weir height and length, discharge, upstream and downstream water depths, gravel mean size, porosity, among others [2]; the relation between the flows over and through the gabion [3, 4]; the measurement of velocities and flow rates [5]; the study of the hydrodynamics of the porous weir and the proposition of nondimensional equations [6]; the energy dissipation [7]; dimensional analyses for discharge coefficients [8, 9]; and upstream and downstream slopes [10]. The conclusions of one-gabion weirs are also used to understand better the characteristics of stepped chutes and spillways built with multiple gabions.

Considering stepped chutes, [11] conducted experiments on gabion-formed stepped chutes with values of s/l of 1.0, 0.67, 0.50, and 0.33, where s represents the step height, and l denotes the length of the step floor. Among [11] contributions, the equation for the energy dissipated by the steps is well known, having been developed using the energy equation and the empirical equations of [12], who studied flow over a one-step dam. The comparison between the experimental data obtained for gabion chutes and the developed equation led to the proposition of some trend lines, albeit with some dispersion of points around the lines.

In the sequence, [1] experimentally studied flows in gabion-formed stepped chutes with s/l ratios of 1.0, 0.50, and 0.33, and for s/h_c ratios ranging from 1.08 to 2.72, where h_c represents the critical depth for a rectangular channel. The authors observed nappe and skimming flow regimes. Among their findings, [1] proposed graphs and equations for calculating the dissipated energy and determining the supercritical depth at the inlet of the stilling basin. The proposed curves exhibit adherence to experimental data with coefficients of determination greater than 0.874. In the same study, [1] suggested using Bélanger's equation for calculating the subcritical depth of the hydraulic jump, h_2, and the equation $L_j = 6h_2$ for calculating the stilling basin length. Bélanger's equation is traditional in the studies of hydraulic jumps, although it does not consider the bottom shear when quantifying the sequent depths. In this sense, [13] showed that the bottom shear can be considered through conservation principles, a method that can be extended to future studies on energy dissipation.

Further, [14] conducted experiments on gabion-constructed stepped chutes with s/l ratios of 0.58, 1.0, and 1.73, and for s/h_c ratios ranging from 0.52 to 6.02. The authors measured pressures, flow depths, and velocities, calculated head losses, and presented nondimensional empirical equations for these variables. They concluded that flows in gabion-constructed stepped chutes may exhibit dimensionless head losses up to 14% higher than flows in conventional stepped chutes. By analyzing data from other authors, [14] proposed Equation 1 for the occurrence of the skimming flow regime in gabion-constructed stepped chutes.

$$\frac{h_c}{s} \geq 0.61\left(\frac{s}{l}\right)^{-0.26} \quad (1)$$

Still further, [15] investigated volumetric air fraction distributions, velocity distributions, flow patterns, and energy dissipation in a gabion stepped chute with s/l = 0.50. Based on their experimental data, the authors concluded that energy dissipation is lower in gabion-constructed stepped chutes than in conventional stepped chutes. This result indicates a discrepancy with the conclusions presented in the literature (for example, [14]), suggesting a potential knowledge gap and the need for further studies.

Using an experimental setup different from the previously described, [16] conducted experiments on a stepped chute with s/l= 1.0, constructed with a structure wrapped in a mesh and filled with stones, which the author claimed represents a structure similar to gabions. The experiments were conducted for s/h_c ratios ranging from 0.94 to 1.2, and the author presented results for specific energy and total energy as a function of the discharge.

[17] conducted experiments on a gabion-stepped chute with s/l = 1.0 and s/h_c ratios ranging from 2.6 to 12.2. The authors measured flow depths and discharges, presenting results for the dimensionless head loss as a function of the discharge and the dimensionless parameter $(h_c/H_{dam})^3$, employed by [1], where H_{dam} is the height from the crest to the bottom elevation of the energy dissipation basin. By comparing the results obtained in a stepped chute with smooth floors, [17] concluded that gabions dissipate up to 16.9% more energy compared to chutes with conventional steps.

Using different gravels, [18] investigated the dissipated energy employing physical models of gabion stepped chutes filled with gravel of mean diameters of 10 mm, 25 mm, and 40 mm in channels with s/l ratios of 1.0, 0.50, and 0.33, and for s/h_c ranging from 0.29 to 4.0. The models utilized in the study included end sills on each step, and flow depths were measured using an ultrasonic sensor at a sampling rate of 20 Hz. The results demonstrated nearly equal energy dissipation, except for s/l = 1.0 and gravel mean diameter equal to 40 mm, resulting in lower dissipation than the other results.

Considering the dimension of hydraulic structures, [19] conducted experiments on a model with dimensions of 1.2 m width, 0.60 m height, s = 0.06 m, s/l = 0.50, and a mean gravel diameter of 24.1 mm for the gabion. The authors compared the energy dissipated by a smooth stepped chute with that dissipated by a gabion-stepped chute. They studied the length of hydraulic jumps established in a stilling basin with blocks, downstream of smooth steps and gabion steps, concluding that an 8.14% average reduction occurs in the hydraulic jump length when using gabions.

The eight articles shown in Table 1 in the present literature review of gabion stepped chutes contain experimental data related to energy dissipation. The Table summarizes the main geometrical characteristics of the physical models. The s/l ratios range from 0.33 to 1.73. The ranges of the dimensionless parameters s/h_c and s/l, together with the descriptions provided by the cited authors, indicate that nappe flow, transition flow, and skimming flow regimes occurred during their experiments.

Table 1. Characteristics of experimental studies on step chutes with gabions

Authors	s/l	s/h_c	H_{dam}/h_c
Stephenson [11]	1.0	-	1.3 - 4.9
	0.67		
	0.50		
	0.33		
Peyras *et al*. [1]	1.0	1.08 - 2.72	3.1 - 12.7
	0.50		3.2 - 12.4
	0.33		3.3 - 12.5
Chinnarasri *et al*. [14]	0.58	0.52 - 3.4	10.5 - 68.2
	1.0	0.74 - 2.4	14.8 - 48.4
	1.73	0.91 - 6.02	18.1 - 120.1
Wüthrich and Chanson [15]	0.50	0.59 - 2.0	5.9 - 20.1
Vashisth [16]	1.0	0.94 - 1.2	3.7 - 4.7
Rajaei *et al*. [17]	1.0	2.6 - 12.2	5.9 - 36.5
Salmasi et al. [18]	1.0	0.29 - 4.0	4.4 - 20.0
	0.50		4.3 - 21.1
	0.33		4.2 - 20.0
Daneshfaraz et al. [19]	0.50	0.97 - 1.75	9.8 - 17.1

Stepped gabion chutes are hydraulic structures that differ from conventional stepped chutes due to their porosity, roughness resulting from the natural irregularities of the rocks and grids, and the flexibility of the structure.

The flow in stepped gabion chute, less studied than in concrete structures, may exhibit different behaviors due to the interaction between the porous medium of the gabions and the overflow. [20] observed this distinction, identifying the hysteresis phenomenon and its influence on energy dissipation.

When designing stepped chute with gabions, it is essential to account for the inherent flexibility of the structure, which allows for a certain degree of deformation. In this context, the frontal slope of the chute may be altered, leading to a corresponding change in the energy dissipation that would be expected based on a conventionally shaped stepped spillway, as demonstrated numerically by [21]. Modifications in the shape of the steps can also lead to significant changes in energy dissipation. In this context, [22] used CFD (Computational Fluid Dynamics) to study stepped spillways with a trapezoidal labyrinth shape and found that these steps exhibited greater energy dissipation compared to conventional ones.

This study aimed to develop new dimensionless equations for designing hydraulic jump stilling basins downstream of gabion stepped chutes. The specific objectives were: (1) to develop equations for calculating the length of the stilling basin, considering state of the art on the length of the hydraulic jump; (2) to propose equations that allow the direct calculation of the elevation of the stilling basin bottom, in such a way that the hydraulic jump is established within it; (3) to propose an equation for calculating the height of the supercritical depth at the stilling basin inlet;

and (4) to demonstrate a methodology for the pre-design of the height of a continuous end sill in gabion stepped chutes.

Methodology

The energy dissipated, and the residual energy at the base of the stepped chute are quantities used to determine the supercritical depth h_1 (of the hydraulic jump) at the inlet of the stilling basin, a parameter used to quantify its size. To ensure that the hydraulic jump is established within the physical limits of the stilling basin, it is necessary to calculate the length and bottom elevation of the basin. All the cited works provide data that allow the calculation of the dimensionless parameter L_j/H_{dam} as a function of H_{dam}/h_c, proposed by [23], where L_j is the length of the hydraulic jump and H_{dam} is the height from the crest to the bottom elevation of the energy dissipation basin (Figure 1). The data also enable the calculation of H_{dam}/h_c as a function of D/h_c, where D is the vertical distance from the crest of the spillway to the water level in the tailwater channel, as indicated in Figure 1.

For the calculation of the mentioned dimensionless parameters, the Bélanger's equation (equation 2) is traditionally used, together with an equation for the length of the hydraulic jump, L_j. In the present description, equation 3 presented by [23] is the key tool for the calculation of the bottom elevation of the energy dissipation basin.

$$\frac{h_2}{h_1}=\frac{1}{2}\left(\sqrt{1+8Fr_1^2}-1\right) \tag{2}$$

where Fr_1 is the supercritical Froude number.

$$\frac{H_{dam}}{h_c}=\frac{D}{h_c}+\frac{h_1}{h_c}\frac{1}{2}\left(\sqrt{1+8\left(\frac{h_1}{h_c}\right)^{-3}}-1\right) \tag{3}$$

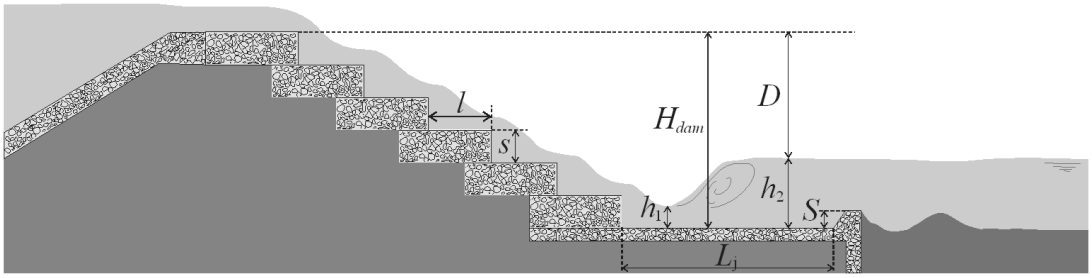


Figure 1. Sketch of stepped chute, variables from equations 1 and 2, and end sill height, *S*.

There are at least twenty equations available for calculating the length of the hydraulic jump, proposed since the early 20th century, which exhibit discrepancies with deviations exceeding 100% [13]. This discrepancy largely arises from the difficulty in defining the final position of the hydraulic jump. [21], using pressure transducers installed near the bottom of the channel and along the hydraulic jump, studied the statistical behavior of pressure distributions and identified the position from which the jump ceases to influence the subcritical flow, thus defining a methodology that can be replicated objectively and takes into account the statistical behavior of pressure near the bottom of the channel. The results of [21] revealed a final position for the jump around 8.5 times the height of the hydraulic jump, for the range $4.9 \leq Fr_1 \leq 9.3$.

Subsequently, [25], employing a methodology akin to that of [24] and focusing on jumps downstream of stepped spillways, measured that the terminal position of the jump was around

eight times the jump height (as per equation 4). This proposal was verified in subsequent experimental investigations, like the study of [26], performed for the Froude Fr_1 number within the $1.9 \leq Fr_1 \leq 4.6$ range.

$$L_j = 8.0(h_2 - h_1) \tag{4}$$

As mentioned, [1] recommends that the length of the hydraulic jump stilling basin be calculated as $L_j = 6h_2$. This recommendation is found in the reference book "*Design of Small Dams*" from 1987. It is based on the detailed study of [27] about the length of hydraulic jumps in rectangular channels with horizontal bottoms. Its use for sizing the length of stilling basins without continuous terminal sill results in shorter basins when compared to equation 4 or the proposal of [24]. This occurs because, on average, $L_j = 6h_2$ is equivalent to $L_j = 6.8(h_2\text{-}h_1)$, for $4.5 \leq Fr_1 \leq 9.0$, with the coefficient 6.8 growing to 7.2 when the Froude number attains $Fr_1 = 4.5$. [24] studied the pressure fluctuations that can induce bed erosion, indicating that lower coefficients of the pressure fluctuation at the end of the hydraulic jump imply safer conditions. In this case, if taking $L_j = 6.8(h_2\text{-}h_1)$, those authors showed that the pressure fluctuation coefficient is around 0.2 for $Fr_1 = 4.5$. On the other hand, taking $L_j = 8.5(h_2\text{-}h_1)$, the same coefficient is around 0.08, which is a difference of about 150%. Consequently, performing a project of a dissipation basin following [27] implies that part of the hydraulic jump may be located on the riverbed, potentially causing erosion and compromising the structure's structural integrity that the correct positioning of the jump should protect.

As known, the length of the stilling basin downstream of stepped spillways can be reduced provided that deflector blocks and an end sill are used, as shown, for example, by the experimental results of [28] and [29], for physical models of stepped spillways with a ratio of 1V:0.75H. In further work, [30] studied four heights of end sills downstream of a physical model of a stepped spillway also with a ratio of 1V:0.75H, concluding that end sills enable the design stilling basins with lengths $L_j \geq 6.9(h_2\text{-}h_1)$, for situations with easily erodible soil.

The three experimental studies of the former paragraph demonstrated that using end sills reduces the length of dissipation basins downstream of stepped spillways. However, applying $L_j \geq 6.9(h_2\text{-}h_1)$ is still limited because of the conditions imposed by the experiments to stepped spillways with a ratio of 1V:0.75H and for concrete as the used building material. In this sense, the presented review highlights the need for specific studies on the characteristics of hydraulic jumps downstream of stepped chutes and spillways constructed with gabions with different inclinations.

The introduction to this study shows that a survey was first conducted about published data of flows in physical models of stepped chutes built with gabions or similar mesh-gravel structures. The valuable studies that described the experiments and published the obtained data in tables and graphs allowed to conduct of the present analysis, enabling proper quantifications of the relevant dimensionless parameters L_j/H_{dam}, D/h_c, and h_1/H_{dam} and the subsequent regression analyses.

Considering the presented arguments for stepped chutes of concrete and the absence of information for gabion stepped chutes, equation 4 was used in favor of security to calculate the length of the stilling basin. The information on the influence of the end sill on the pressure distribution near the channel bed and the risk of erosion downstream of the basin was also taken into account. The methodology involved the use of nonlinear regression to determine the coefficients of the proposed equations for calculating the length and bottom elevation of the stilling basin. The coefficients were calculated using custom programming in Python, C, MATLAB, and, occasionally, Excel.

Results

As a synthesis of the conducted analyses, the data of the studies of Table 1 were compiled in Figure 2a, including the curves obtained by calculating the coefficients *a* and *b* of equation 5, a model similar to that of [23] and [31] for conventional stepped spillways. The data from [16] were not included in the fit because they exhibited significantly different behavior from the others, likely due to the geometrical differences of the steps implied by the adopted constructive method (rounded steps). The coefficients *a* and *b*, their respective correlation coefficients, and validity intervals are presented in Table 2. The graph and correlation coefficients show that equation 5 [31] adequately represents the trend of those experimental data and that there is adherence between the model and experimentation.

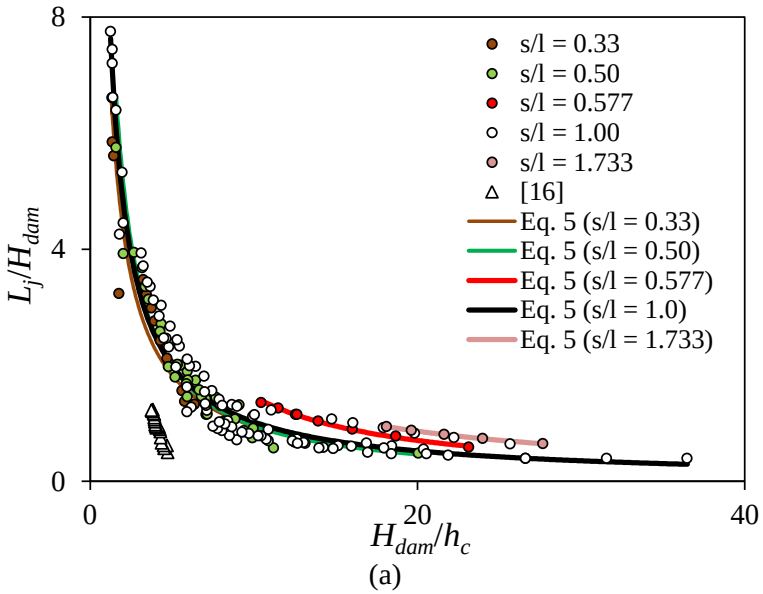
$$\frac{L_j}{H_{dam}} = \mathrm{a}\left(\frac{H_{dam}}{h_c}\right)^b \tag{5}$$

The average trend of equation 7 is obtained by taking the data of different origins as a single set and including the additional point from [14] for *s*/*l* = 1.0, (48.4; 0.27), where "tgh" is the hyperbolic tangent. The lower and upper envelopes given by equations 6 and 8 were calculated to indicate the observable variations. The coefficients of equation 7 were obtained through nonlinear regression applied to equation (5) for the interval $1.25 < H_{dam}/h_c < 48.4$, resulting in a correlation coefficient 0.970. The maximum relative deviation around equation 7 obtained with equation 6 is 39%, and with equation 8 is 47%.

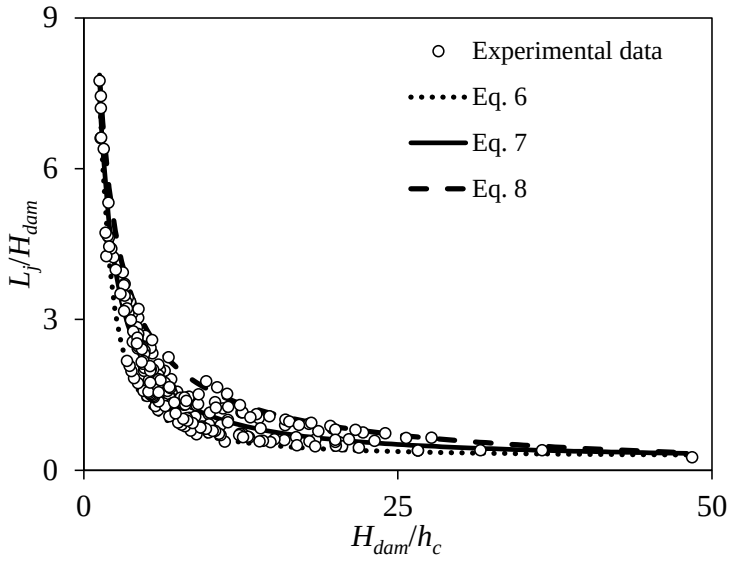
$$\frac{L_j}{H_{dam}} = -22.0\mathrm{tgh}\left[-0.48\left(\frac{H_{dam}}{h_c}\right)^{-1.41}\right] + 0.26 \tag{6}$$

$$\frac{L_j}{H_{dam}} = -15{,}1\mathrm{tgh}\left[-0{,}67\left(\frac{H_{dam}}{h_c}\right)^{-1{,}03}\right] + 0{,}15 \tag{7}$$

$$\frac{L_j}{H_{dam}} = -22{,}2\mathrm{tgh}\left[-0{,}45\left(\frac{H_{dam}}{h_c}\right)^{-0{,}74}\right] - 0{,}22 \tag{8}$$



(a)



(b)

Figure 2. Fitting of equation 5 to the experimental data (a) and equations 6, 7 and 8 (b).

The relationship between the dimensionless parameters H_{dam}/h_c and D/h_c (see Figure 1) followed the linear trend also observed for smooth and conventional stepped spillways. Equation 9 shows the basic linear trend between both variables and Table 2 shows the *c* and *d* values for each set of data. The correlation coefficients are greater than 0.98 for all values of *s*/*l*. The analysis of the unified data produced equation 10, with a correlation coefficient of 0.999, a spreading of data as shown in Figure 3, and valid for the interval $0.17 < D/h_c < 34.33$.

$$\frac{H_{dam}}{h_c} = c\frac{D}{h_c} + d \tag{9}$$

$$\frac{H_{dam}}{h_c} = 1.01\frac{D}{h_c} + 1.7 \tag{10}$$

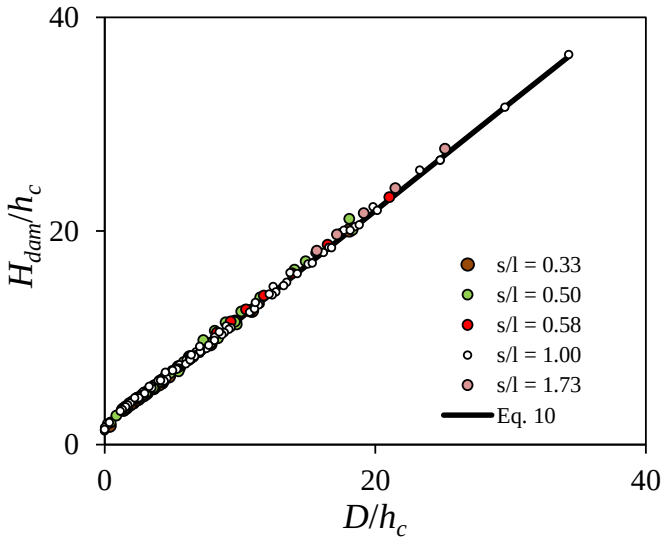


Figure 3. Fitting of equation 10.

Table 2. Coefficients of equations 5 and 9

s/l	a	b	R (eq. 5)	(*) H_{dam}/h_c	c	d	R (eq. 9)	(**) D/h_c
0.333	8.010	-0.895	0.952	1.35 - 20.04	1.010	1.703	0.999	0.36 - 18.09
0.500	8.480	-0.872	0.959	1.58 - 20.12	1.040	1.640	0.998	0.46 - 18.34
0.577	16.370	-1.050	0.994	10.46 - 23.14	0.982	2.385	0.999	8.31 - 21.06
1.000	9.670	-0.961	0.982	1.25 - 36.49	0.988	1.689	0.999	0.17 - 34.33
1.733	12.390	-0.889	0.999	18.12 - 27.68	1.010	2.297	0.999	15.69 - 25.17

Symbol: R = correlation coefficient; *validity interval for equation 5; **validity interval for equation 9.

For the calculations of the supercritical conjugate depth h_1 at the entrance of the stilling basin, the dimensionless parameter h_1/H_{dam} proposed by [1] showed a strong correlation with H_{dam}/h_c, leading to equation 11, valid for $1.74 < H_{dam}/h_c < 48.4$ and $1.18 < Fr_1 < 6.61$, with $R = 0.973$. The data and the equation are shown in Figure 4a, and the relatively small spreading of the data around the exact fit line is shown in Figure 4b.

$$\frac{h_1}{H_{dam}} = 18.1\text{tgh}\left[0.030\left(\frac{H_{dam}}{h_c}\right)^{-1.09}\right] + 0.005 \tag{11}$$

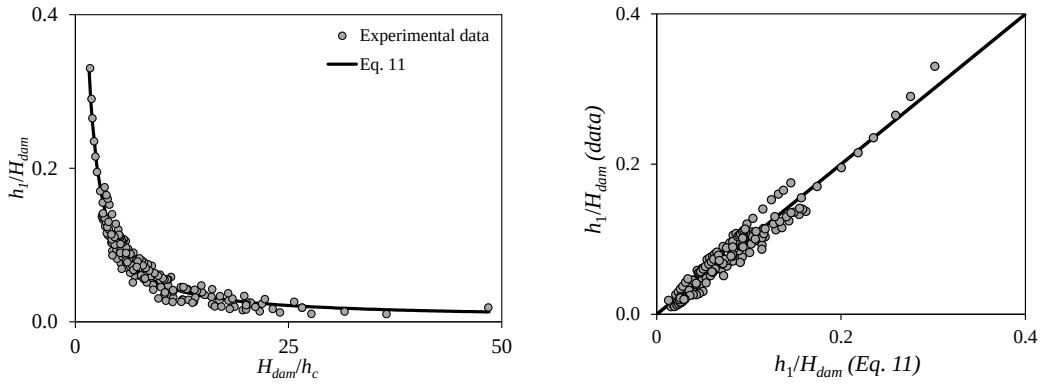


Figure 4. Relationship between h_1/H_{dam} and H_{dam}/h_c (a); comparison with the exact fit line (b)

The data of [30] were used to quantify the sill height S shown in Figure 1. Following the mentioned author, the data were expressed in the dimensionless form S/h_1 and as a function of the Froude number at the entrance of the stilling basin. The work of [30] considered the interval $5.44 \leq Fr_1 \leq 7.44$. Observing further the trend line inserted by [30], a possible constant value of S/h_1 for $Fr_1 \leq 5.44$ was noted. Considering this conjecture, Equation 12 is recommended here for the broader interval $1.89 \leq Fr_1 \leq 7.44$, being this a first quantification for pre-designs. It must be noted that the scarcity of data impedes a more definitive affirmation. Figure 5a shows the data graph and Equation 12, and Figure 5b shows the adjustment between the data and the proposed equation.

$$\frac{S}{h_1} = 2.1.10^{-5}\exp\left(Fr_1^{1.22}\right) + 1.62. \tag{12}$$

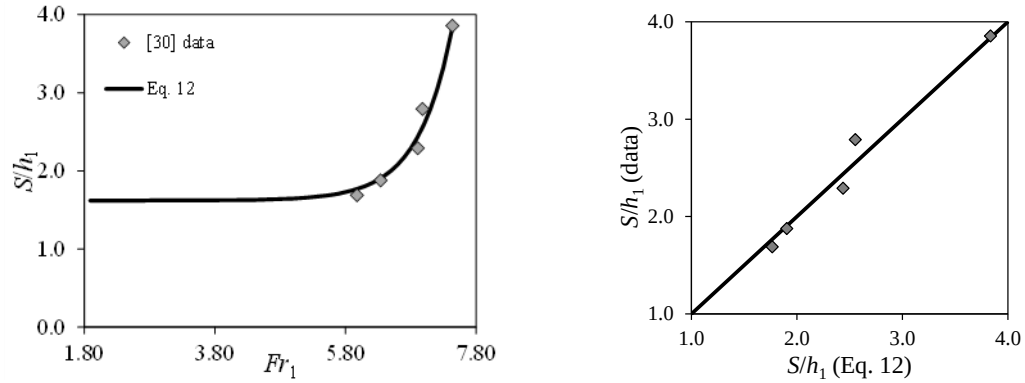


Figure 5. Relationship between S/h_1 and Fr_1 (a); comparison with the exact fitting line (b).

Example of Application

For the application of equations derived from researches that must consider some more profound scientific questions to attain their objectives, a practical sequence of steps considering the use of the main conclusions is very welcomed.

In this sense, the present example considers a spillway system to be designed with a rectangular stepped chute and a stilling basin of the same width to meet the following design conditions: (1) flow rate, Q = 204.2 m³/s; (2) width, B = 40 m; (3) s = 0.35 m and l = 1.05 m; (4) crest elevation of the weir, z_0 = 27.6 m; (5) elevation of the water level in the tailwater channel, z_2 = 20 m.

The practical steps are as follows:

For H_{dam} and L_j:

1) Initially, the specific discharge should be calculated, which leads to $q = Q/B \approx 5.11$ m²/s. The critical depth, used in the dimensionless parameters, follows immediately as $h_c = (q^2/g)^{1/3} = (5.11^2/9.8)^{1/3} \approx 1.39$ m.

2) In the sequence, the value of D (see figure 1) is obtained as $D = z_0 - z_2 = 27.6 - 20 = 7.6$ m, which produces $D/h_c \approx 5.49$.

3) Knowing the ratio of $s/l = 0.35/1.05 = 0.33$, it is possible to identify the values of c = 1.01 and d = 1.703 in Table 2 for the use of Equation 9, which leads to $H_{dam}/h_c = (1.01)(5.49)+1.703 = 7.24$ and, in the sequence, H_{dam} = 10.04 m. Table 2 allows interpolations of c and d for values of s/l not explicit in the table. It is noted that the values of D/h_c and H_{dam}/h_c are within the corresponding range for Equation 9, as shown in Table 2, enabling the use of Equation 5 with the respective coefficients.

4) Knowing $s/l = 0.33$, the coefficients of Equation 5 are a = 8.01 and b = -0.895; which lead to $L_j/H_{dam} = 8.01(7.17^{-0.895}) = 1.36$ and, in the sequence, L_j = 13.7 m.

Thus, H_{dam} and L_j were calculated. For further information, applying the values $s/l = 0.33$ and $s/h_c = 0.25$ to equation 1 indicates the occurrence of the transition flow regime.

To exemplify the use of Equations 7 and 10 for the unified set of data and compare their results with the equations developed for each s/l separately, we have the following steps:

1) Equation 10 provides the value of $H_{dam}/h_c = (1.01)(5.49)+1.7 = 7.24$ and, in the sequence, H_{dam} = 10.03 m. A relative deviation of only 0.04% is observed compared to Equation 9.

2) Equation 7 provides the value L_j/H_{dam} = -15.1tgh[(-0.67)(7.24$^{-1.03}$)]+0.15 = 1.463 and, in the sequence, L_j = 14.7 m. A relative deviation of 7.4% is observed when compared to Equation 5. It is understood as acceptable for the pre-design phase.

For *S*:

1) Equation 11 provides the value h_1/H_{dam} = 18.1tgh[(0.030)(7.24)$^{-1.09}$]+0.005 = 0.06776 and, in the sequence, h_1 = (0.06776)(10.03) = 0.68 m.). With this h_1 value, the Froude number is Fr_1 = 2.91.

2) Equation 12 provides then the value S/h_1 = 2.1.10^{-5}exp(2.91$^{1.22}$)+1.62 ≈ 1.621, and, in the sequence, *S* = 1.10 m.

S was thus calculated. As mentioned before, the scarceness of data for establishing equation 12 implies that this value should be taken for the pre-design phase. Certainly, more experimental data will improve the assurance of the proposed methodology.

Using the methodology of [1]:

1) For s/l = 0.33, the mentioned authors propose h_1/H_{dam} = 0.3416[$q^2/(gH_{dam}{}^3)$]$^{0.248}$ = 0.3416[5.11²/((9.8)10.03^3)]$^{0.248}$ = 0.0783 and, in the sequence, h_1 = 0.779 m.

2) The sequence of calculations furnishes, then: $V_1 = q/h_1$ = 6.56 m/s, Fr_1 = 2.37 and $h_2 = 0.5h_1[(1+8Fr_1^2)^{1/2}-1]$ = 2.25 m.

3) The mentioned authors recommend the use of $L_j = 6h_2$ = (6)(2.25) = 13.5 m.

L_j was thus calculated. However, the mentioned authors did not present a way to calculate H_{dam}, probably using the value measured in the experimental device in their calculations. Taking the shortest length obtained in the present study, the relative deviation about the result of [1] is (13.7-13.5)100/13.5 = 1.5%. The result of [1] is shorter, being eventually seen as economically more attractive. However, the formulation proposed here involves data from different origins, corresponding to a broader coverage of possible cases, where different practical conditions were employed. Additionally, the present result favors the security of the dissipation basin, avoiding the risk of intense fluctuations downstream of its end, thus avoiding the risk of erosion after the basin. As a further advantage of the present method, the sill height is also calculated.

Conclusions

The present literature review of gabion stepped chutes identified six experimental studies with adequate sets of data, conducted for the ratio s/l between 0.33 and 1.73. Although somewhat scattered, the data exhibited well-defined nondimensional trends for the length and bottom elevation of the stilling basin, as well as for the supercritical depth at the stilling basin inlet. One of the obtained datasets showed a significant deviation from the others, likely due to geometric differences (rounded steps due to the building procedures). This dataset was not used to obtain the here obtained equations, but suggests further studies involving geometry variations. The here proposed equations for the length of the stilling basin exhibited adherence to the experimental data through a power law, for both situations: 1) when used for each s/l separately, and 2) when used for the unified set of data. In the last case the envelopes of the dataset indicate relative deviations between 35% and 58%. Analyses regarding the bottom elevation of the stilling basin for the formation of the hydraulic jump within the basin limits led to linear equations between H_{dam}/h_c and D/h_c for each value of s/l, and also for the unified analysis, resulting in high correlations and adherence to the experimental data. The relatively non-dispersed characteristic of the data allows to propose the equation for the unified data, as the one

to be used in the calculations of such basins. Further, the evident relationship between h_1/H_{dam} and H_{dam}/h_c induced to a new equation for the calculation of h_1, with high adherence to the data and consequently a strong statistical correlation. Finally a methodology for calculating the height of the continuous end sill, was proposed, being mentioned that this topic requires further investigation, considering the current lack of data for gabion stepped chutes. An example of application was presented in a detailed step by step manner, where the present methodology was compared to a methodology available in the literature. The results show compatible results between the two methodologies, but point to the higher security of the present methodology, which considers sets of data of different sources.

ACKNOWLEDGMENTS

This work was supported by the Coordination for the Improvement of Higher Education Personnel - Brazil (CAPES) - Financing Code 001; processes 88881.708215/2022-01, PDPG Emergencial de Consolidação Estratégica dos Programas de Pós-Graduação (PPGs) stricto sensu acadêmicos com notas 3 e 4, from the Master's Program in Environment, Water, and Sanitation – MAASA – UFBA and the Bahia State Research Support Foundation (FAPESB), under Grant Agreement No. PIE0021/2016.

References

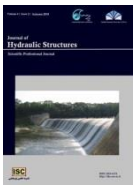
1. Peyras, L.; Royet, P.; Degoutte, G. (1992). “Flow and energy dissipation over stepped gabion weirs”. *Journal of Hydraulic Engineering*, Vol. 118, No.5, May, 1992, pp.707-717.
2. Mohamed, H.I. (2010) Flow over Gabion Weirs. *Journal of Irrigation and Drainage Engineering*, ASCE, August 2010, pp. 573-577. DOI: 10.1061/(ASCE)IR.1943-4774.0000215.
3. Al-Mohammed, F.M.; Mohammed, S.H. (2015) Flow Through and Over Gravel Gabion Weirs. *Journal of Kerbala University*, Vol. 13 No.2 Scientific, pp. 193-205.
4. Velázquez-Luna, L; Ventura-Ramos, E. (2017) Concentrated Flow through Gabions Weirs. *Hydraulics Conference of Autónoma de Querétaro*, IEEE, Querétaro, México, May 15-19, pp.1-4.
5. Pallavi, M.; Harashit, L. (2018) Open Channel Flow Characteristics Using Gabion Weir. *International Research Journal of Engineering and Technology* (IRJET) Vol. 5, No. 12, pp. 928-933.
6. Safarzadeh, A.; Mohajeri, S.H.; (2018) Hydrodynamics of Rectangular Broad-Crested Porous Weirs. *J. Irrig. Drain Eng.* ASCE, Vol. 144, No 10, 04018028.
7. Al-Fawzy, A.M.; Al- Mohammed, F.M.; Alwan, H. (2020) Energy dissipation in gabion weirs. *3rd International Conference on Engineering Sciences*, IOP Conf. Series: Materials Science and Engineering 671, pp.1-12.
8. Salmasi, F.; Sabahi, N.; John Abraham, J. (2021) Discharge Coefficients for Rectangular Broad-Crested Gabion Weirs: Experimental Study. *J. Irrig. Drain Eng.*, ASCE, Vol. 147, No. 3, 04021001.
9. Azma, A.; Sadrabadi, M.T.; Liu, Y.; Azma, M.; Zhang, D.; Cao, Z.; Li, Z. (2023) Boosting ensembles for estimation of discharge coefficient and through flow discharge in broad-crested gabion weirs. *Applied Water Science* 13:45. https://doi.org/10.1007/s13201-022-01841-x

10. Biabani, R.; Salmasi, F.; Nouri, M.; Abraham, J. (2022) Flow Over Embankment Gabion Weirs in Free Flow Conditions. *Journal of Hydro-environment Research*, ELSEVIER, Vol. 44, pp. 65-76.
11. Stephenson, D. (1979). "Gabion energy dissipators". *Proc. 13th ICOLD Congress,* New Delhi, Q. 50, R.3, p. 33-34, 1979.
12. Rand, W. (1955). Flow geometry at straight drop spillways. Journal of the Hydraulics Division, Proceedings, ASCE, v. 81, n. 791, Sept., p. 1-13, 1955.
13. Schulz, H.E.; Nóbrega, J.D.; Simões, A.L.A.; Schulz, H; Porto, R.M. (2015). *Details of Hydraulic Jumps for Design Criteria of Hydraulic Structures*, *Hydrodynamics - Concepts and Experiments*, Prof. Harry Schulz (Ed.), ISBN: 978-953-51-2034-6, InTech.
14. Chinnarasri, C.; Donjadee, S.; Israngkura, U. (2008). "Hydraulic Characteristics of Gabion-Stepped Weirs". *Journal of Hydraulic Engineering*, ASCE, Vol. 134, No. 8, August 2008, pp. 1147-1152.
15. Wüthrich, D.; Chanson, H. (2014). "Hydraulics, Air Entrainment, and Energy Dissipation on a Gabion Stepped Weir". *Journal of Hydraulic Engineering*, ASCE, June 2014, Vol. 140, No. 9, pp. 04014046.
16. Vashisth, A. (2017). "Energy Dissipation over Stepped Gabion Weir". *International Journal of Dynamics of Fluids* Vol. 13, No. 1, pp. 153-159.
17. Rajaei, S.H.; Khodashenas, S.R.; Esmaili, K. (2020). "Comparative evaluation of energy dissipation over short stepped gabion and rigid spillways". *Journal of Hydraulic Research*, Vol. 58, No. 2, pp. 262-273.
18. Salmasi, F.; Razi, S.; Abraham, J. (2023). Hydraulics of flow in gabion stepped spillways, an experimental study. Journal of Hydraulic Structure. 9, p. 75-100. 2023.
19. Daneshfaraz, Rasoul; Sadeghi, Hojjat; Ghaderi, Amir; Abraham, John Patrick (2024) The effect of gabion steps on the hydraulic jump characteristics downstream of stepped spillways, Water Science, 38:1, 128-139, DOI: 10.1080/23570008.2024.2307243
20. Daneshfaraz, Rasoul; Aminvash, Ehsan; Najibi, Amir. Experimental Study of Hysteretic Behavior of Supercritical Regime on Hydraulic parameters of Flow against Gabion Contraction. Iranian Journal of Soil and Water Research, [S.l.], v. 53, n. 1, p. 33-44, mar. 2022. University of Tehran. DOI: 10.22059/ijswr.2022.334538.669141
21. Aminvash, E.; Roushangar, K. (2023). Numerical Investigation of the Effect of the Frontal Slope of Simple and Blocky Stepped Spillway with Semi-Circular Crest on Its Hydraulic Parameters. Iranian Journal of Irrigation and Drainage, 17(1), 102-116.
22. Ghaderi, A., Abbasi, S., Abraham, J.; Azamathulla, H. M. (2020). Efficiency of Trapezoidal Labyrinth Shaped stepped spillways. Flow Measurement and Instrumentation, 72, 101711. https://doi.org/10.1016/j.flowmeasinst.2020.101711
23. Simões, A.L.A. (2008). Considerações sobre a hidráulica de vertedores em degraus: metodologias adimensionais para pré-dimensionamento. Dissertação (Mestrado) – Escola de Engenharia de São Carlos – Universidade de São Paulo, São Carlos.
24. Marques, M.G.; Drapeau, J.; Verrette, J-L. (1997). "Flutuação de pressão em um ressalto hidráulico". *Revista Brasileira de Recursos Hídricos*, Vol. 2, No. 2, Jul/Dez 1997, pp. 45-52.
25. Novakoski, C. K. (2016). Análise da distribuição longitudinal das pressões em um ressalto hidráulico formado a jusante de vertedouro em degraus. Dissertação (Mestrado em Recursos Hídricos)—Porto Alegre: Universidade Federal do Rio Grande do Sul - UFRGS, 2016.

26. Steinke Júnior, R. (2020). Caracterização das pressões em bacias de dissipação por ressalto hidráulico livre com baixo número de Froude. Dissertação (Mestrado em Recursos Hídricos)—Porto Alegre: Universidade Federal do Rio Grande do Sul - UFRGS, 2020.
27. Bradley, J. N.; Peterka, A. J. (1957). "The hydraulic design of stilling basins". ASCE, *Journal of Hydraulic Engineering*. Vol.83, n.HY5, p.1401-1406, Oct., 1957.
28. Cardoso, F.G. (2006). Estudo do ressalto hidráulico em bacias de dissipação de energia a jusante de descarregadores de cheias em degraus. 2006. 143f. Trabalho de Conclusão de Curso (Engenharia Civil) – Instituto Superior Técnico, Universidade Técnica de Lisboa.
29. Meireles, I.O.C; Matos, J.; Silva Afonso, A. (2010). Flow characteristics along USBR type III stilling basin downstream of stepped spillways. Hydraulic Structures: Useful Water Harvesting Systems or Relics? Third International Junior Researcher and Engineer Workshop oh Hydraulic Structures, May, 2010, Edinburgh, Scotland. R, Janssen and H. Chanson (eds). Hydraulic Model Report CH80/10, School of Civil Engineering, The University of Queensland, Brisbane, Australia, 211 pp.
30. Conterato, E. (2014). Determinação de critérios de dimensionamento de soleira terminal em bacia de dissipação a jusante de vertedouro em degraus. Dissertação (Mestrado em Recursos Hídricos)—Porto Alegre: Universidade Federal do Rio Grande do Sul - UFRGS, 2014.
31. Simões, A. L. A., Schulz, H. E. and Porto, R. M. (2010) Stepped and smooth spillways: resistance effects on stilling basin lengths, Journal of Hydraulic Research, 48: 3, 329 — 337.

© 2025 by the authors. Licensee SCU, Ahvaz, Iran. This article is an open access article distributed under the terms and conditions of the Creative Commons Attribution 4.0 International (CC BY 4.0 license) (http://creativecommons.org/licenses/by/4.0/).

Journal of Hydraulic Structures
J. Hydraul. Struct., 2025;11(1):65-88
DOI: 10.22055/jhs.2024.47686.1318



OPEN ACCESS

Numerical Study of Permanent Deformations of Embankment dams under Seismic Loading, A case study of Kheyrabad Dam

Masoud Oulapour [*1]
Mohammad Amjadzadeh [1]
Hossein Samani [1]

Abstract

Considering the developments of new accurate constitutive models and numerical methods, a comparison between the classical and modern numerical methods of dynamic analysis of earthfill dams seems necessary. A three steps procedure was followed in this study. First, the accelerations and displacements of a typical homogenous dam were calculated using Sarma, Makdisi-Seed, and Sarma-Ambraseys methods, the results were compared with the results of Quake/W and Slope/W software using both linear elastic and equivalent linear models. Then, a special code was developed to calculate the deformations of a given wedge of the dam body based on the outputs of numerical analyses and the Newmark double integration method. The studies showed that due to the use of linear elastic behavior model, which is different from the real soil behavior, the critical acceleration estimated in classic methods is different from the reality and leads to oversized design. However, the more realistic constitutive models give better results. Also, in classic methods the shape of the wedges was unrealistic as it was assumed to pass through the core of the dam, while in numerical analysis it was shown that the critical wedge passes through downstream shell. Therefore, since the shape of critical wedges in homogeneous dams was completely different from the assumed shape of critical wedges in classic methods, the critical acceleration of wedges was different from the predictions of the classic models, for example it was estimated to be 0.41g in the Ambraseys-Sarma method compared to 0.31g in the linear method for a wedge depth of 60% of dam height. It was concluded that numerical methods with more realistic constitutive models must be used. Finally, the Kheyrabad embankment dam was analysed using the developed method. It was concluded that the dam would show a permanent deformation of 0.04 m under scaled Naghan earthquake.

Keywords: Embankment dams, Dynamic analysis, Critical Acceleration, Permanent Deformations, Equivalent Linear model.

Received: 07 August 2024; Accepted: 24 September 2024

[*] E-mail: Oulapour_m@scu.ac.ir (**Corresponding Author**)
[1] Department of Civil Engineering, Faculty of Civil Engineering and Architecture, Shahid Chamran University of Ahvaz, Ahvaz, Iran.

CC BY

1. Introduction

Earth dams are massive three-dimensional and non-homogeneous structures composed of multi-phase, non-linear elastic materials. Therefore, their dynamic analysis under earthquake loading is one of the most complex problems in dam engineering. Recent advances in computer hardware and software, as well as the growing development of numerical methods for solving engineering problems, have overcome the problems related to these complexities, especially in the nonlinear behavior of dam materials. The early studies on the seismic stability of earth dam slopes can be attributed to the research of Mononobe et al. [1]. They initially proposed the shear beam method, which did not gain much attention due to the extensive computations required. In this method, the dam structure is assumed to be deformable, and its cross-section is divided into very thin horizontal layers, connected by linear elastic shear springs and viscous dampers. Later, Terzaghi [2] proposed the pseudo-static method and these methods were widely used then and are still somewhat relevant today. The basic assumption in the Terzaghi method was that the dam body behaves as a rigid body. Therefore, the effective acceleration in all its sections and at any height is equal to the maximum ground acceleration. Newmark [3] introduced the sliding block method, which is still in use by engineers and researchers due to its simplicity and practicality. Permanent deformations can be calculated for any specified sliding wedge using this method. Goodman and Seed [4] showed that the Newmark model gives acceptable results for highly cohesive soils. Seed [5] showed that an accurate determination of critical acceleration is very crucial for the estimation of permanent displacement. The development of the finite element method and its application in dynamic slope stability analysis led to a significant advancement in dam analysis methods. Ambraseys and Sarma [6] studied the response of earth dams under a group of important earthquakes and calculated the time history and distribution of acceleration in the dam body. Sarma [7] developed charts for calculating critical horizontal acceleration, where the critical horizontal acceleration is defined as the acceleration which can take the soil mass of the sliding wedge to a limit equilibrium state. Sarma [8] investigated the sensitivity of calculating permanent displacements to the parameters used in determining critical acceleration, such as dimensional coefficients and wedge geometry. Sarma [9] used the Newmark analysis model to show the effects of inertial forces and pore water pressure on the safety factor, critical acceleration, and displacements of potential sliding surfaces. This analysis was based on the principles of limit equilibrium, and the materials followed the Mohr-Coulomb failure criterion. Soil resistance parameters were also based on effective stress parameters. Makdisi and Seed [10] analyzed several different dams using the QUAD-4 program and calculated permanent deformations on assumed sliding surfaces using the Newmark sliding block method based on the movement of the block on the inclined surface. Seed [11] stated that if a dam is designed with a pseudo-static earthquake coefficient between 0.1 and 0.15 and a safety factor of 1 to 1.15, it will be stable and as long as the maximum crest acceleration of the dam is less than 0.75 g, the dam will be sustainable under an earthquake of magnitude 8.5 and its deformations will be tolerably small. Paskalov [12,13] included pore water pressure in calculating the critical acceleration using the average pore pressure coefficient and applied the method to seismic analysis of the damages of Upper SanFernando dam by 1971 earthquake. It was concluded that the method predicts the permanent deformations successfully. Hynes-Griffin and Franklin [14] stated in a report prepared for a group of engineers that if a dam is designed for an acceleration equal to half the maximum acceleration at the dam base and has at least 1 m additional freeboard, it will remain stable if a safety factor of at least one is reached using undrained parameters. Finn et al. [15] developed the TARA-3 computer program and directly calculated permanent deformations. The program was capable of performing both dynamic and

static analysis using either effective or total stress conditions. Daghigh [16] conducted a numerical study on the dynamic behavior of earth dams under seismic loading, and the general differential equation of dynamic equilibrium was solved using three different methods: 1) modal method, 2) complex response method, and 3) implicit numerical integration method. Cai and Bathurst [17] reviewed two methods, including one which only uses the peak ground acceleration and velocity as the properties of input motion and the other method which uses the fundamental period of the acceleration and provides the probability of exceedance for the expected permanent displacement. They indicated that statistically, the second method provides more reliable results. Matsumoto [18] conducted shaking table experiments involving models with maximum accelerations up to 0.7g. These experiments showed that only shallow landslides without deep and distinct failure surfaces in the core occur. Therefore, it was concluded that the Newmark method may be somewhat unrealistic. Day [19] demonstrated theoretically that slopes made of dry granular soil can undergo settlements and lateral deformations under an earthquake with a peak ground acceleration less than the critical acceleration. Therefore, he concluded that in some cases the Newmark method may not be reliable. Swaisgood [20] investigated over 70 earthquake-induced failures. The results showed that the peak ground acceleration (PGA) and earthquake magnitude (M_W) are the most important factors affecting the crest settlement of dams due to earthquakes. A graph was developed that briefly summarizes the relationship between the measured settlement and the maximum ground acceleration. A new empirical relationship was also presented. It was also found that the deformations of the dam were mainly settlement and lateral deformation, and no sliding along a distinct failure surface was observed. Based on the investigations, serious damages to the dam was only observed in cases where the PGA exceeded 0.2g, which was consistent with previous findings that a well-constructed dam can withstand moderate earthquakes with a maximum acceleration of up to 0.2 without damage. Wang et al. [21] incorporated a new nonlinear, effective-stress-based bounding surface hypo-plasticity model for sand instead of the frequently used the equivalent linear approach. They calculated permanent deformations and compared with the values estimated using other used models and measurements and concluded that the results showed the role of a suitable constitutive equation. Han and Hart [22] compared simple elastoplastic models with equivalent linear models and nonlinear numerical methods and concluded that simple elastoplastic models with small damping are accurate enough to determine the permanent settlements at the dam crest. Bray and Travasarou [23] utilized a nonlinear fully coupled stick-slip sliding block model to simulate the dynamic performance of an earth dam. The seismic displacement model which was developed capture the yield coefficient k_y, initial fundamental period Ts, and the ground motion's spectral acceleration at a degraded period equal to 1.5Ts, and includes the simultaneous occurrence of the nonlinear dynamic response of the potential sliding mass and the effects of periodic sliding events. The proposed model provided estimates of seismic displacements that were generally consistent with documented cases of earth dams. Sica et al. [24] studied the seismic performance of a zoned earth dam using coupled analysis. It was revealed that previously experienced stress paths, such as strong motions, influence seismic performance by hardening of the soils. The hardening parameters could be obtained by back analysis of a seismic event. Rampello et al. [25] evaluated the response of a homogeneous earth dam under real and synthetic earthquake loadings assuming different depths of bedrock. They conducted decoupled approach of displacement-based analysis which is based on the assumption that the sliding block analysis can be decoupled from the ground response analysis of the earth structure. They concluded that permanent displacements are resulted from plastic strains that accumulate during the earthquake because of the progressive plastic loading which are influenced by the duration of the strong

motions. Also, the results showed that the horizontal and vertical displacements of the body were also less than the crest settlement due to the mobilization of shear resistance in the confined upper third of the dam. The results of the finite element analysis were also higher than those of the double integration method from the acceleration diagram. Jinto and Davidson [26] compared the existing methods for determining permanent earthquake-induced displacements. They also critically reviewed the pseudo-static method and showed that the effective stress dynamic analysis method is a perfect tool for assessing the impact of earthquakes on earth dams, particularly their permanent deformations. Jibson [27] compared different methods for calculating permanent displacements and concluded that the rigid block analysis method is more suitable for shallow landslides and stiff ground. In contrast the coupled sliding block method is more suitable for deep landslides and softer soils. Also, it was concluded that the sliding block method is suitable for cases where the soil fundamental periods are greater than 10% of the average earthquake periods. Hsieh and Lee [28] modified the relationship between critical acceleration, Arias earthquake intensity, and permanent displacements by considering various sites and adding a new term, proposing more accurate relationships for rock and soil sites. Davoodi et al. [29] investigated the effect of fundamental periods of dam on the crest settlement of the dams in near or far field earthquakes. They indicated that high dams have smaller settlement of the crest and more critical responses to near-field records and shorter dams have more critical responses to far-field records. Dong et al. [30] investigated an ultra-tall dam and found that the acceleration amplification in the upper part of the dam increases sharply and reaches a maximum at the crest, and horizontal and vertical displacements at the crest are the largest. Bandini et al. [31] proposed a more complete method that considers the changes in wedge geometry and shear resistance due to sliding. The predicted behavior matched the observed behavior, which indicates the need to consider changes in block geometry and shear resistance due to sliding in the calculations. Park and Kutter [32] studied the effects of soil sensitivity on slope failure mechanisms by performing some static and dynamic centrifuge experiments for different earthquake input motions and some Vane shear and uniaxial compression tests to obtain the strength and sensitivity of the materials. It found that in dynamic tests, in a deep failure, there exists a diffused plastic zone, while in a shallow failure distinct shear bands are formed. Bray et al. [33] proposed a new probabilistic method incorporating the uncertainty of input ground motion. This model considers the slope's strength, vibration characteristics, and earthquake intensity. Ghahraman-nejad and Kan [34], using various methods of analysis ranging from empirical to non-linear numerical, compared the deformations of several case studies and predicted the magnitude of the crest settlements and concluded that assuming a unique failure plane, as adopted by some of the simplified methods, may be necessarily misleading, as deformation would be more likely to be characterized by the deformation pattern predicted using a non-linear elastoplastic model and numerical modeling. Chen and Liu [35] used Choleski decomposition method to generate random field for spatial variability of porosity and quantified a relation between the compaction quality and porosity. Implementing the relation in stochastic finite element method, it was concluded that the spatial variation of the compaction quality will lead to significant risk of exceeding standard of the displacements and stresses. Rollo and Rampello [36] employed a probabilistic approach to analyze slope stability during earthquakes with the ability to incorporate the inherent variability. The analysis exploits a comprehensive database of ground motion measurements. Mazaheri et al. [37] presented an improved approach by employing both static and dynamic analyses and an elastoplastic model, and Rayleigh damping in Abaqus software and studied the Azadi dam. The results of the dynamic analysis showed a 37% increase in settlement compared to the quasi-static

analysis. Cho and Rathje [38] developed a generic predictive model for earthquake-induced slope displacements based on the results of many of nonlinear finite-element (FE) simulations. The model was the first that related the displacement with the ratio of the depth of the critical slip surface relative to the slope height. Hwang and Rathje [39] performed a numerical parametric analysis consisting several models with soil stiffness and strength parameters selected to isolate the impact of yield acceleration, depth of the sliding mass, natural period of the slope, and the slope angle on the deformation patterns. The results indicated that deeper sliding masses experience notable strain localization at the sliding mass depth, while shallow sliding masses experience more distributed straining throughout the entire soil mass. Also, larger displacements for the deep sliding masses relative to shallow sliding masses at small ky are observed, whereas shallow sliding masses experience larger movements at large ky. Zhang et al. [40] examined the combined effects of mainshocks and aftershocks on slope sliding using 273 ground motion records from actual seismic sequences. The calculation results were compared with the traditional Newmark method and a displacement predictive model based on the FEM was proposed. They concluded that the sliding displacements which are calculated based on considering the aftershock effect were more conservative compared to those that only considered the mainshock effect. Consequently, a combination of the optimal scalar parameter of the mainshock and an aftershock parameter is required to express the characteristics of the seismic sequence.

According to the literature review, the utmost important objective of the dynamic analyses performed is to examine the accuracy of past approximate methods and to compare them with the results of dynamic analysis based on the finite element method (FEM). Therefore, it is attempted to use the geometry and characteristics corresponding to those of the Ambraseys and Sarma [6] so that the results obtained under the same initial conditions can be compared. In this study, a finite element software was used to calculate the accelerations and an auxiliary software was developed to determine the average acceleration and displacement in any specific failure wedge based on the analysis results. As a case study, the procedure was performed on the Kheyrabad dam using its real geometry and geotechnical parameters.

2 Materials and methods

The results of three different classic methods of calculating permanent displacements of the dam were compared with the results of numerical methods. The classic methods include: Ambraseys-Sarm, Sarma, and Makdisi-Seed methods. These methods and their related factors are briefly reviewed here.

2.1 Ambraseys-Sarma method

In this method, a series of wedges are considered with different depths ranging from 0.2h up to 2h from the dam crest, where h stands for dam height. The considered wedges have a specific shape, which is defined by n, the ratio of wedge depth to dam height, ψ, θ, as shown Fig. 1. The ratio of maximum of average wedge acceleration to peak ground acceleration, $\bar{k}_n$, is maximized at a θ about 50 when the wedge angle, ψ, is around 80 to 90. This increase in $\bar{k}_n$ becomes less significant as the fundamental period of the dam increases.

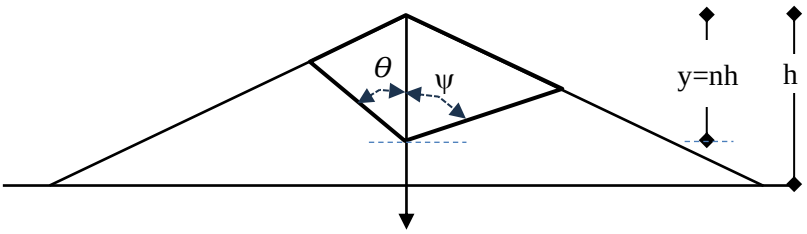


Figure 1. General Wedge geometry in Ambrasis & Sarma [6]

2.1.1 Natural Period of Vibrations of the Dam

In all of the methods of analysis, the natural frequency of the first mode of vibrations of the dam body should be determined, which can be calculated based on the Sarma method [41] as in equation 1:

$$T_0 = \frac{2\pi h}{S_1 a_1} \tag{1}$$

where h stands for the dam's height, and S_1 is the shear wave velocity in the dam body. The coefficient a_1 is obtained from Fig 2 based on the relative shear wave velocity in the foundation alluvium and the dam body parameters m and q, which are calculated using equations 2 and 3, presented in the following:

$$m = \frac{s_1 \rho_1}{s_2 \rho_2} \tag{2}$$

$$q = \frac{s_1 (H - h)}{s_2 h} \tag{3}$$

where H is the sum of the dam's height and the thickness of its alluvial foundation, and S_2 is the shear wave velocity of the alluvial foundation of the dam. Also, r_1 and r_2 are densities of the dam body and its alluvial foundation, consequently.

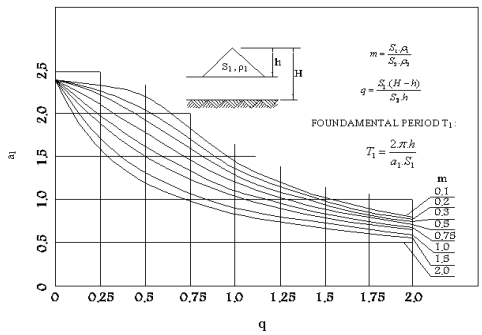


Figure 2. Fundamental period of the dam and foundation system [41].

As in the analyzed models the dams are assumed to be on seated on the bedrock, the value of q in Fig. 2 is zero and therefore, the value of a_1 is 2.3. Based on the relation between elastic modulus and shear wave velocity, the relation between the natural frequency, T_0, and elastic modulus, E, can be written as in equ. 4:

$$T_0 = \frac{2\pi h}{S_1}\sqrt{\frac{2(1+\mu)\rho}{E}} \quad (4)$$

where ρ is the density of the dam body materials. This shows that the natural period, T_0, is inversely proportional to the elastic modulus. Given the natural period of the dam body, T_0, the $\bar{k}_n$ can be determined for any given wedge based on its *n*, which then can be multiplied by the peak ground acceleration to obtain the maximum simultaneous acceleration for the given wedge. Given $\bar{k}_n$, and the maximum ground acceleration, $a_{base,max}$, the maximum simultaneous earthquake force applied to the wedge, F_n can be obtained from equation 5:

$$F_n = M_n . \bar{k}_n . a_{base,\,max} \quad (5)$$

where M_n presents the mass of the wedge. In the next step, the critical acceleration, k_y, the acceleration at which the safety factor for a given wedge is equal to one, must be determined. The critical acceleration for any wedge is obtained from the equation 6:

$$k_y = tg(\varphi_{eq} - \alpha) \quad (6)$$

where f_{eq} is the equivalent friction angle and a is the slope of wedge. Using coefficient *C*, as calculated using equation 7:

$$c = \frac{\cos(\beta-\theta-\varphi')}{\cos\varphi'} \quad (7)$$

where, β indicates the average angle of the shear surface with the horizon, θ is the angle of earthquake force with the horizon, and ϕ' is the effective friction angle of the material along the shear surface. Using k_n and the value of the coefficient C, the amount of horizontal displacement Xm can be calculated using the relevant graphs.

2.2 Sarma Method

The method of Sarma is mainly similar to the method of Ambraseys-Sarma, but in this method the charts modified by Sarma [7] are used. In this case, the maximum acceleration applied to the wedge can be calculated.

2.3 Makdisi-Seed Method

In this method, the first step is determining the maximum acceleration applied to the dam crest, Ümax. Determining the Ümax is difficult as it is very fluctuating. This is the weak point of the method. However, it can be determined using a finite element dynamic analysis. Next, the ratio of the maximum simultaneous acceleration applied to the intended wedge (Kmax) to the maximum acceleration of the dam crest can be estimated from the relevant charts based on the ratio of the wedge depth to the dam height. Then, the critical acceleration, k_y, the acceleration at which the safety factor of the wedge becomes equal to one, is calculated using pseudo-static analysis (SLOPE/W) or equation (6). Finally, the displacement induced in the intended wedge is determined using earthquake magnitude and the natural period of the dam body. [10]

2.4 Finite Element Method

In this study, the finite element method along with the nonlinear material behavior models were used for the dynamic analysis of the dam body. To perform the dynamic finite element analysis in the QUAKE/W software, first a preliminary static analysis must be performed to determine the initial stresses [42]. In this case, the required parameters are the elastic modulus, Poisson's ratio, shear modulus, and specific gravity of the materials. After the static analysis, the obtained stresses are used as input data for the dynamic analysis. In the stage of dynamic analysis, after introducing the initial static model as input, the functions of the variations of shear modulus and damping ratio, obtained from cyclic tests or existing charts, are entered. In this analysis, if a linear elastic model is used, the constant damping and shear modulus are used. Nevertheless, if an equivalent linear model is used for the material behavior, the damping ratio and shear modulus functions must be used [19]. Then, the results of the dynamic analysis of the models are used as input data in SLOPE/W. In this case, the calculated values of stress and strain in the dynamic analysis at each Gaussian point are used by the SLOPE/W calculations to estimate the failure wedge, average acceleration and displacement of the wedge, safety factor, critical acceleration of the wedge, etc.

2.4.1 Computational time step

The results of dynamic analysis calculations are sensitive to the choice of appropriate time step. The smaller the time step, the higher the accuracy of the results [42]. However, this needs much more time and computational cost. Therefore, to determine the appropriate time step, first the most significant frequency of loading or required response must be determined. If this value is denoted by w_n, based on equation (8), 5% of the corresponding period is considered as the time step, unless a smaller value for Δt is required due to convergence problems in the nonlinear analysis [42]:

$$\Delta t = \frac{1}{20}\frac{2\pi}{\omega_n} \approx \frac{0.3}{\omega_n} \tag{8}$$

2.5 Material properties and geometry of the dam in validation calculations

As the Sarma and Ambraseys (1967) models assume the dam's sections to be triangular and homogeneous, a homogeneous dam with a height of 50 meters and a side slope of 2.5H:1V is considered for validation calculations [6]. The characteristics of the model and the material properties used in validation calculations are presented in Table (1).

Table 1. Material properties and geometrical parameters used in validation example

Elastic Modulus (kPa)	105	Poisson Ratio	0.4
Natural Period (sec.)	1	Cohesion (kPa)	11
Damping (%)	20	θ of wedge(deg.)	50
Friction Angle (deg.)	38	ψ of wedge(deg.)	90

Soil stiffness is generally a function of the stress state, and the soil stiffness increases with increasing confining or overburden stress. It is particularly true for non-plastic granular soils. QUAKE/W uses Equation (9) to implement this effect:

$$G = K_G.(\sigma_m')^n \tag{9}$$

where, K_G and n are experimental constant coefficients and σ'_m is the average of the effective principal stresses. If the value of n is set equal to zero, G becomes a constant value, and if it is equal to one, then *G* increases linearly with depth. The value of the dynamic shear modulus, G, for the shell and core of the dam (granular and cohesive media) is obtained from equations 10 and 11 as follows:

$$G = 32700\ \frac{(2.97-e)^2}{4e}\sqrt{\sigma'_m} \quad \text{(used for dam core)} \quad (10)$$

$$G = 2210\ K_2\sqrt{\sigma'_m} \quad \text{(used for dam shell)} \quad (11)$$

Here, the shear modulus value, G, is obtained in kPa. The void ratio, e, based on the consolidation tests on samples prepared according to construction specification, is equal to 0.56 for core materials. The value of the coefficient K_2 is a function of the induced shear strain on the soil, the relative density of the material, and the gradation of the granular material. It is presented by experimental curves, covering the design purposes and conditions where the loading duration is less than 4 to 10 seconds. It is assumed to be between 120 and 170, with an average of 150.

2.6 Details of the developed code

Performing dynamic analysis by QUAKE/W can yield the values of acceleration, displacement, etc. at each node [42]. However, to determine the sliding wedge, the dynamic model must be linked to SLOPE/W. Also, the average acceleration, critical acceleration, safety factor, and displacement of the critical wedge must be calculated using the Newmark method throughout the earthquake duration. To compare the classic pseudo-static and the finite element method, a program was written to calculate the items mentioned above for any specific wedge at each time step, based on the results of the finite element analysis [43]. This rectifies the weakness of continuum mechanics-based models in determining plastic deformations. In this program, first, the coordinates of the nodes of the generated mesh in the model are read from the QUAKE/W program. Then the components of displacement, velocity, and acceleration at each node in both x and y directions are read from the output of the dynamic analysis [44]. Next, the configuration of the dam, including the upstream and downstream slopes, height and width of the berm (if any), and the configurations of the intended wedge, including the slopes of the two broken lines, are entered. The program starts by identifying all points located in the intended wedge, and stores their information. Then, the wedge area is divided into horizontal strips, the number of which is specified by the user, and the nodes located in each strip are identified, and their average displacement and acceleration are calculated and stored as the average displacement and acceleration of the strip. Finally, the average acceleration of the wedge is obtained using equation (12):

$$\ddot{U}_{ave} = \frac{1}{A}\sum a_i \ddot{U}_i \quad (12)$$

where a_i is the cross-sectional area of the i^{th} horizontal strip, $\ddot{U}_i$ is the average acceleration of the i^{th} horizontal strip calculated by the code, and A is the total cross-sectional area of the wedge. These steps are repeated for each time step. After each step, the final result is saved. Finally, the variations of maximum acceleration of the intended wedge are plotted as a function of time. In the next step, the developed code calculates the maximum displacement of the intended wedge at each time step by two different methods. In the first method, the same steps which were used to

calculate the maximum average acceleration are followed. In this method, equation (13) is used to calculate the maximum displacement of the wedge:

$$U_{ave} = \frac{1}{A}\sum a_i U_i \tag{13}$$

where the *Ui* is the average displacement of the i[th] horizontal strip. This method is used when the wedge behaves elastically, and has not yet entered the plastic state. To determine the behavior of the wedge, the shear stresses in the dam body are determined after completing the dynamic analysis. Also, the shear resistance at the bottom of the wedge is calculated using the Mohr-Coulomb shear strength model as in equation 14:

$$\tau_{max} = c' + \sigma'_n \, tg\,(\varphi') \tag{14}$$

where c' is the effective cohesion, σ' is effective vertical stress, and ϕ' is the effective friction angle. If τ_{max} is less than the working shear stress, the permanent deformations in the wedge have occurred, otherwise, the deformation of the wedge is considered elastic. In the second method, after calculating the average maximum acceleration applied to the wedge and plotting it as a function of time by double integration of the part of the acceleration-time curve in terms of time which is higher than the critical acceleration, the average maximum displacement of the wedge is obtained, which is the permanent displacement of the wedge.

3. Results and discussion

3.1 Validation Calculations

As mentioned in the previous section, a practical example was used in order to ensure the accuracy of the results of the model. The El Centro earthquake accelerogram was selected as the input earthquake to the model, and the boundary conditions were also defined. It was assumed that the dam is seated directly on the bedrock, which means that the entire bottom boundary of the model was assumed to be fixed in both x and y directions. Figure (3) shows some of the wedges used in the validation stage. Also, a summary of the results obtained from the methods mentioned above, is presented in Table 2.

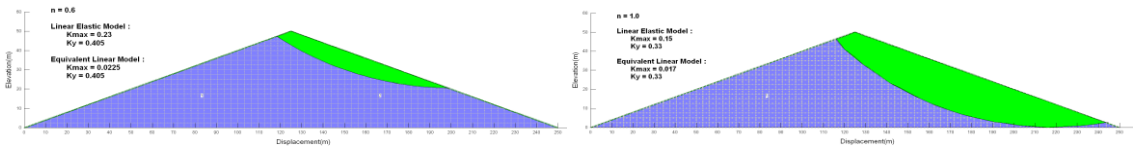


Figure 3. Maximum acceleration and critical acceleration in wedges used in validation stage.

As can be seen in Fig. (3), the shape of the wedges formed in the dam's body was entirely different from what Ambraseys and Sarma [6] had considered as the critical wedge. Therefore, the average critical acceleration of the wedges did not follow the graphs presented by Ambraseys and Saruma [6]. In order to reduce the number of variables and simplify the calculations, the shape of the critical wedge was adopted based on the graph prepared by Ambraseys and Sarma [6], which is inherently unable to yield accurately the acceleration induced in trial wedges with arbitrary shape. As can be seen in Table 2, among the classic methods, the Ambraseys-Sarma method [6] has resulted in the highest maximum horizontal accelerations and the lowest

maximum displacements, and it differed significantly from the other two methods. However, the results of the Sarma and Seed-Makdisi methods, which show lower maximum accelerations and larger maximum displacements, are closer to each other. However, the difference between these two methods is significant for shallow wedges, while for the case of wedge depth equal to dam height, they are very close. The main reason of the difference in the results of the Ambraseys-Sarma method with other two methods, is the method of determining the critical acceleration. This result indicates the importance of choosing the strength parameters, especially for the shell zone, as it controls the critical acceleration. Also, according to Tab.3, the calculated displacements from the classic methods and the numerical dynamic analysis performed with the linear elastic model using SLOPE/W are much greater than the other methods.

Table 2. Summary of dynamic analysis results of classic methods for validation example

Wedge Depth	Maximum Displacement (m)			Critical Acceleration (g)			Maximum Acceleration (g)		
	1	2	3	1	2	3	1	2	3
0.2h	0.97	0.480	0.63	0.014	0.240	0.014	0.418	0.530	0.460
0.4h	0.78	0.140	0.59	0.011	0.240	0.011	0.300	0.456	0.357
0.6h	0.52	0.040	0.42	0.012	0.240	0.012	0.209	0.342	0.272
0.8h	0.27	0.008	0.25	0.020	0.240	0.020	0.165	0.275	0.0204
1.0h	0.14	0.000	0.15	0.025	0.240	0.025	0.119	0.216	0.150

1=Sarma, 2=Ambraseys-Sarma, 3=Seed-Makdisi

One of the reasons for this is the use of a linear constitutive model for the soil. The energy dissipation in plastic deformations is not considered in this model. Unfortunately, most classic methods are based on a linear elastic model for soil materials. Linear numerical dynamic analysis is only suitable for relatively rigid structures subjected to low vibrations. In soil structures where the elastic zone of materials is very limited, usually nonlinear analysis is necessary.

Table 3. Summary of dynamic analysis results of numerical methods for validation example

Wedge Depth	Maximum Displacement (m)				Critical Acceleration (g)				Maximum Acceleration (g)			
	SlopeW		Code		SlopeW		Code		SlopeW		Code	
	1	2	1	2	1	2	1	2	1	2	1	2
0.2h	0.845	0.149	0.124	0.0640	0.014	0.014	0.014	0.014	0.420	0.034	0.684	0.294
0.4h	0.784	0.129	0.110	0.0636	0.011	0.011	0.011	0.011	0.295	0.028	0.512	0.290
0.6h	0.707	0.089	0.095	0.0630	0.012	0.012	0.012	0.012	0.230	0.023	0.447	0.292
0.8h	0.504	0.000	0.079	0.0615	0.020	0.020	0.020	0.020	0.180	0.020	0.429	0.297
1.0h	0.365	0.000	0.063	0.0544	0.025	0.025	0.025	0.025	0.150	0.017	0.376	0.289

1= Linear model, 2=Equivalent Linear model

Another notable point is that the written code, which uses the results of the QUAKE/W program at each time step, gives more realistic figures. Table 4 presents relatively similar measured values. All of these figures indicated the validity of the calculations of the written code. This shows that classic and numerical methods based on elastic behavior are very conservative and lead to extra volume of construction operations, materials consumption, and construction costs. Therefore, numerical methods and more accurate constitutive models must be used.

3.2 Kheyrabad Dam Calculations

In this research, the Kheyrabad dam was used as a case study. The dam site is located 33 km south of Behbehan city, near the Behbehan-Bandar e Deylam asphalt road, on the Kheyrabad

Table 4. A history of some of the permanent displacement incidents occurred in a number of dams in different countries

No.	Dam properties						Earthquake Properties				Damage	
	Name	Country	Type	H (m)	CL (m)	FT (m)	date	M	FD (km)	PGA (g)	S. (m)	Damage
1	Vermilion	California	E	50	1290	50	80.05.27	6.3	22	0.24	0.05	Negligible
2	Namioka	Japan	ECRD	52	265	0	83.05.26	7.7	145	0.08	0.06	Negligible
3	La Villita	Mexico	ECRD	60	427	75	85.09.21	7.5	61	0.04	0.12	Negligible
4	Nagara	Japan	ECRD	52	-	?	87.12.17	6.9	29	0.27	0.02	-
5	Austrian	California	E	56	213	0	89.10.17	7.1	2	0.57	0.85	Sever
6	Lexington	California	E	63	253	0	89.10.17	7.1	3	0.45	0.26	Minor
7	Diayo	Philippines	ECRD	60	201	0	90.07.16	7.7	18	038	0.07	Minor
8	R. Matthews	California	E	46	192	0	92.04.25	6.9	64	0.07	0	Negligible
9	Los Angeles	California	E	47	671	0	94.01.17	6.7	10	0.43	0.09	Medium

E: Earthfill dam, ECRD: Earth Core Rockfill Dam, H: Height, CL: Crest Length, FT: Foundation Thickness, M: Magnitude, FD: Focal Depth, PGA: Peak Ground Acceleration, S: Crest Settlement river.

This river is a tributary of Zohreh river. The dam is an earthfill-rockfill dam with a vertical clay core, a height of 60 meters from the foundation, a crest length of 720 meters, and a body volume of 4.5 MCM. The reservoir volume equals 179 MCM, the normal reservoir level is 259.6 meters above sea level, and a maximum flood level of 269.5 meters above sea level.

3.2.1 Design Earthquakes

Since the graphs provided in currently available methods are based on the El Centro earthquake accelerogram, this earthquake was used in numerical analysis of this research, in order to obtain comparable results. However, for dynamic modeling of the dam, the seismological characteristics of the construction site should be used. By combining the seismologic and geological studies of the site, the acceleration with a specified occurrence probability over the structure's life is calculated based on statistical methods. The horizontal component of acceleration of the design base level (DBL) earthquake is 0.295 g, and the vertical component is 0.18 g. The horizontal component of accelerations of the maximum design level (MDL) earthquake is 0.406 g, and the vertical component is 0.253 g.

3.3.2 Dynamic analysis of Kheyrabad dam using classical methods

In this stage, the stability of the Kheyabad dam (Fig. 4) under earthquake conditions is investigated using the pseudo-static method. In this context, slope stability analysis is performed using the limit equilibrium method, and the effect of the earthquake is implemented by horizontal or vertical forces, or both applied to the center of gravity of each slice. The magnitude of these forces were calculated by multiplying the seismic coefficients to the weight of each slice. In other words, in this analysis, a fraction of the acceleration of gravity is considered as the equivalent seismic inertia [45].

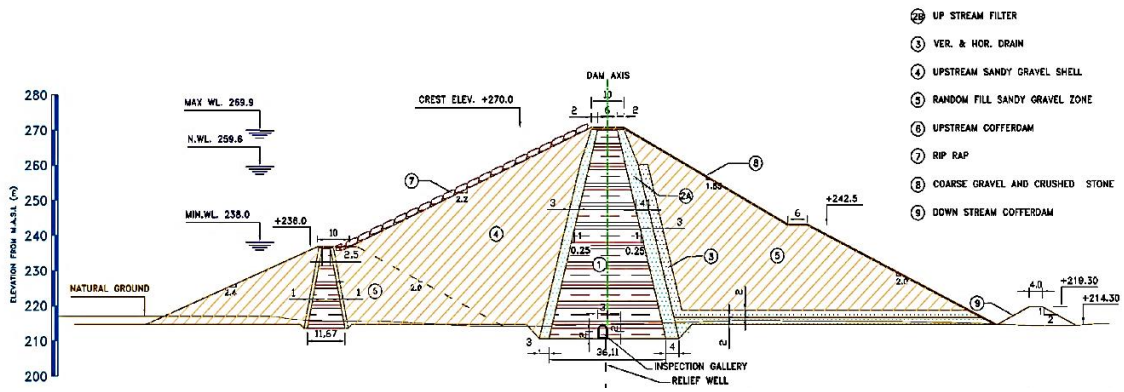


Figure 4: Geometry of highest cross-section of Kheyrabad dam

As during an earthquake, the displacement of the slopes of an earth dam is within an acceptable range, applying seismic coefficients corresponding to the probable earthquake at the site will result in the design of a slope that will not move or deform during the earthquake, which is unnecessary and very conservative [46]. On the other hand, the maximum acceleration of the probable earthquake is applied to the dam only for a fraction of a second, and then it will reduce or even change direction. Therefore, in practice, it is feasible to reduce the design seismic coefficient and accept some level of movement of the slope and its consequent deformation of the dam's body. The effective seismic coefficient is selected based on the magnitude and peak ground acceleration of the expected earthquake at the dam site. Usually, mandatory codes of practice require selection of some recommended seismic coefficients for dam design. Due to the lack of such criteria in the current dam design standards in Iran, the seismic coefficient in slope stability calculations is generally selected based on engineering judgment and with reference to technical manuals and codes of practice of other countries. For example, the Japanese standard recommends a minimum seismic coefficient of 0.18g at the foundation of dams in high-risk areas, which increases linearly to 0.45g at the dam crest. The US Army Corps of Engineers recommends a seismic coefficient 0.15 for high-risk zones in zoning maps.

Based on the above, and the results of seismologic studies of the Kheyrabad dam site, a horizontal seismic coefficient of 0.15 was used for the end-of-construction loading case and 0.15 and 0.20 for the remaining loading cases in the pseudo-static analyses. Due to the low and also unknown effect of the vertical component of earthquake, it was not applied. According to the results of the stability control analyses, in which accelerations of 0.15g and 0.2g were used as the PGA of the design base earthquake (DBE) and maximum credible earthquake (MCE), the studied storage dams will not have large and destructive deformations during an earthquake. During the occurrence of the maximum probable earthquake and the design base earthquake in short periods, the sliding masses will have an acceleration higher than the critical acceleration of the intended wedge. This acceleration, due to the reciprocating nature of the earthquake, changes direction immediately. However, a permanent displacement of the slopes of the dam occurs. These displacements must not compromise the overall stability of the dam. It means the deformations must be small, and give enough opportunity for the remediation process. The Newmark method, which calculates the permanent displacement of a specified wedge by double integration of the average acceleration of the sliding wedge in excess of the critical acceleration, has been used here. The methods proposed by Sarma, Ambraseys-Sarma, and Seed-Makdisi are used in this regard. According to seismological studies, the horizontal and vertical peak ground accelerations of the maximum credible earthquake at the Kheyrabad dam site were proposed to

be 0.532 g and 0.331, respectively. Assuming that the upstream shell is submerged, the downstream shell unsaturated, and the dam core is saturated, the average effective stresses in these zones are calculated using weighted averaging along the vertical slices, which were equal to 320, 400, and 664 kPa, respectively. As a result, the corresponding shear modulus values were calculated to be 589, 663, and 218.5 MPa, respectively. To calculate the average shear wave velocity in the dam body, weighted averaging of the shear modulus, G, and density, □□ were performed over the areas of each zone. Considering that the shear wave velocity for the upstream shell, downstream shell, and core were calculated to be 164, 183, and 102 m/s, respectively, the average shear wave velocity in the body is calculated to be 164 m/s. Therefore, considering that in this stage, the dam is assumed to be located on the bedrock, the value of q in the relevant charts will be zero, and as a result, the value of a_1 is equal to 2.3. Using the values of h, S_1, and a_1 the natural period of the first mode of vibration of the dam body was estimated to be 1.0 second. Using the Ambraseys-Sarma chart, the natural period of the dam body, and the maximum bedrock earthquake acceleration, the maximum acceleration induced at the dam crest is calculated to be 0.66g. The results of dynamic calculations show that despite the material damping, due to the bottom-up propagation of transverse earthquake waves, the wave vibrations are amplified along the dam's height dam.

To calculate the earthquake permanent displacements, initially, the critical seismic coefficient must be determined. For this purpose, sliding surfaces for different depths have been analyzed using the SLOPE/W software. As mentioned in earlier, various methods has been used for this purpose, including the Ambraseys-Sarma, the Sarma, and the Seed-Makdisi methods. The results of these methods are presented in Tab. 5:

Table 5. The calculated permanent displacements of Kheyrabad dams using 1) Sarma, 2) Seed-Makdisi, 3) Ambraseys-Sarma methods

Wedge Depth (y/h)	Kc			Km			Kc/Km			$\frac{4X_m}{C.K_m.g.T^2}$			Xm (cm)		
	1	2	3	1	2	3	1	2	3	1	2	3	1	2	3
0.2	0.46	0.46	0.48	0.64	0.71	0.81	0.72	0.65	0.59	0.040	0.010	0.08	7.2	6.9	18.0
0.4	0.30	0.30	0.43	0.45	0.50	0.70	0.67	0.60	0.62	0.053	0.011	0.07	6.8	5.2	13.8
0.6	0.29	0.29	0.41	0.32	0.42	0.52	0.91	0.69	0.79	0.001	0.006	0.02	0.1	2.6	2.9
0.8	0.29	0.29	0.4	0.25	0.31	0.42	1.16	0.93	0.95	-	0.0002	0.001	0.0	0.0	0.1
1.0	0.24	0.24	0.38	0.18	0.23	0.33	1.33	1.04	1.15	-	-	-	0.0	0.0	0.0

3.3.3 Dynamic analysis of Kheyrabad dam using numerical methods

For the dynamic analysis of the Kheyrabad earth dam, first, the static stresses were determined using appropriate linear elastic geotechnical properties of the materials, as presented in Table 6, which were introduced to the QUAKE/W sub-module of Geo-Studio finite element software. The discretization of the dam is presented in Fig. 5, and contour lines of calculated initial static stresses is presented in Figs. 6, which proves the validity of the numerical calculations. Next, the Naghan earthquake accelerogram, scaled to the design maximum probable earthquake (MDL) acceleration, presented in Fig. 7, was used, and the dynamic calculations were performed.

Table 6: The geotechnical material properties used in initial static analysis

Material	Saturated density	Wet density	Elastic Modulus	Poisson ratio	Shear Modulus	Damping ratio
	r_{sat} Ton/m^3	r_{wet} Ton/m^3	E MPa	υ	G MPa	ξ (%)
Shell	2.19	1.98	58	0.32	22	0.10
Filter	2.16	2.00	40	0.34	14.9	0.15
Core	2.10	2.02	20	0.36	7.35	0.20
Foundation	2.20	2.20	2000	0.30	76.9	0.02

Nevertheless, for the equivalent linear model, instead of the constant values provided in table 5, the damping ratio and shear modulus were selected based on shear strain and according to the functions shown in Figure 8. The time step in calculations was chosen iteratively. The peak horizontal accelerations of Kheyrabad Dam under the El Centro earthquake scaled to a maximum acceleration of g 0.41 were calculated for time steps of 0.01, 0.02, 0.05, and 0.08 sec. The results were the significantly different when 0.08 sec was used for the time step, but the same results were obtained when 0.01 and 0.02 sec were used as time steps. Considering saving in time and cost, and ensuring the accuracy of the solution, the time step of 0.02 sec was used in all analyses.

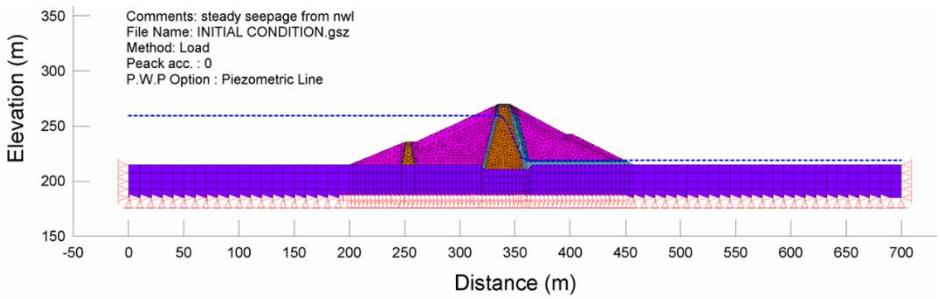


Figure 5: The discretization and boundary conditions of Kheyrabad dam

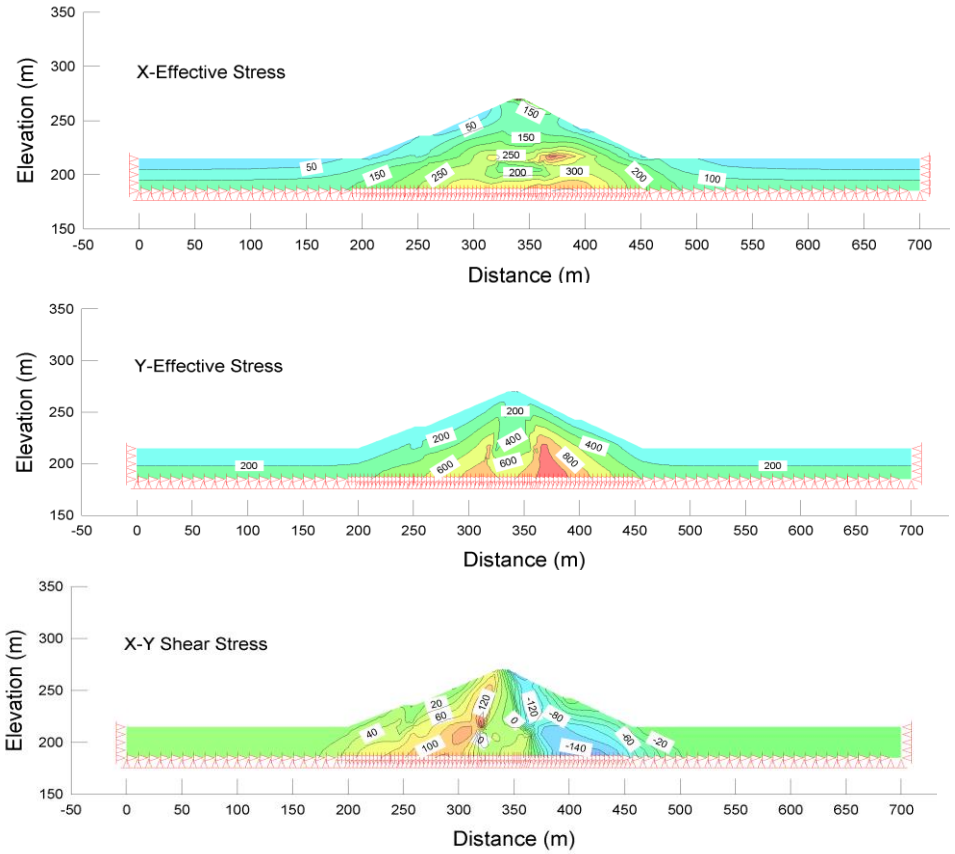


Figure 6: Isometric contour lines of the initial static stresses of Kheyrabad Dam

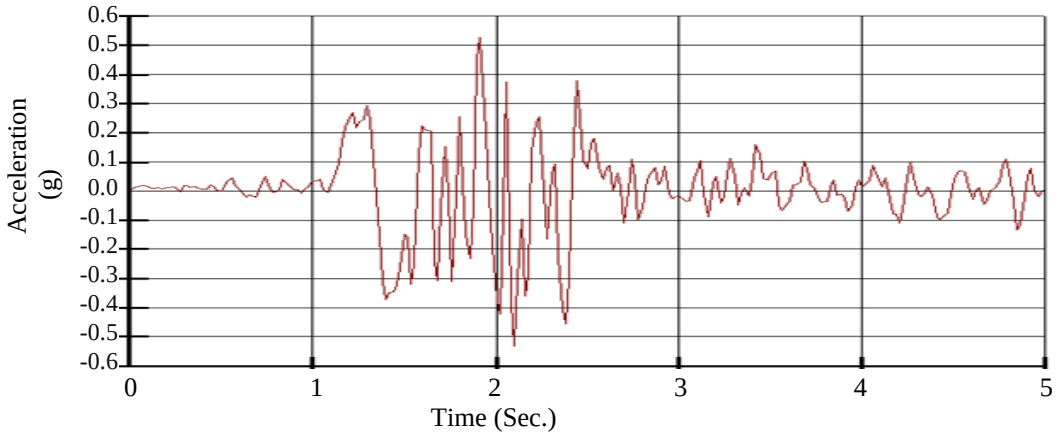


Figure 7: Naghan earthquake record scaled to MDL earthquake of Kheyrabad dam

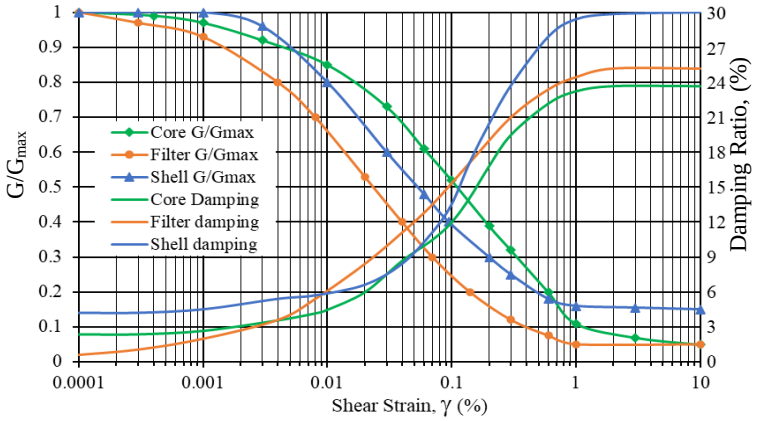


Figure 8: Shear modulus and damping ratio functions for dynamic analysis

The results of the dynamic analysis were used to determine the average acceleration and displacement induced in any intended wedge. The stresses, accelerations, and displacements calculated by the dynamic analysis were imported to the SLOPE/W software. It calculates the average acceleration and displacement for the intended wedges using the Newmark method. The final results of the dynamic analysis for wedges with different depths are summarized in Table 7, which presents the results of the dynamic analysis for both linear elastic and equivalent linear models.

It is observed that although the maximum acceleration at the dam crest was higher in the linear elastic model than in equivalent linear model, the maximum displacement obtained in this model was less. This was attributed to the decrease in the shear modulus ratio with increasing shear strain. Also, due to the increase in the damping ratio due to the increasing shear strain in the equivalent linear model, the dam crest accelerations were less than the elastic linear case model.

3.3.4 Dynamic analysis of Kheyrabad dam using numerical methods and the developed code

As the Newmark method is also a classic method, an effort was made to develop a program which could calculate the accelerations and displacements of wedges based on the results of the finite element method dynamic analysis.

Table 7. Summary of the results of the dynamic stability analysis of Kheyrabad Dam performed with SLOPE/W

Type of analysis	Wedge depth/dam height	0.2	0.4	0.6	0.8	1.0
Linear Elastic	Critical acceleration (g)	0.46	0.30	0.31	0.29	0.24
	Maximum acceleration(g)	0.24	0.23	0.21	0.19	0.17
	Displacement (m)	0.000	0.000	0.000	0.000	0.000
	Factor of Safety	1.55	1.35	1.20	1.19	1.15
Equivalent Linear	Critical acceleration, ky	0.38	0.25	0.29	0.23	0.18
	Maximum acceleration, kmax	0.069	0.062	0.050	0.044	0.040
	Displacement (m)	0.000	0.000	0.000	0.000	0.000
	Factor of safety	2.12	1.61	1.58	1.56	1.50

A summary of the results obtained by this code using both linear elastic and equivalent linear models is presented in Table 8. Also, a summary of the results of all methods including results earlier presented in tables 5, 7 and 8, is now presented in Table 9 for comparison. Figure 9 shows the variations of the permanent deformations calculated by the developed code for a wedge of 1.0h depth for both linear elastic and equivalent linear elastic models.

Table 8. Summary of the results using the developed code for Kheyrabad dam

Type of analysis	Wedge depth/dam height	0.2	0.4	0.6	0.8	1.0
Linear Elastic	Critical acceleration (g)	0.46	0.30	0.31	0.29	0.24
	Maximum acceleration(g)	0.449	0.441	0.447	0.532	0.450
	Displacement (m)	0.000	0.028	0.021	0.024	0.036
Equivalent Linear	Critical acceleration, ky	0.38	0.25	0.29	0.23	0.18
	Maximum acceleration, kmax	0.559	0.557	0.541	0.528	0.555
	Displacement (m)	0.018	0.040	0.034	0.038	0.041

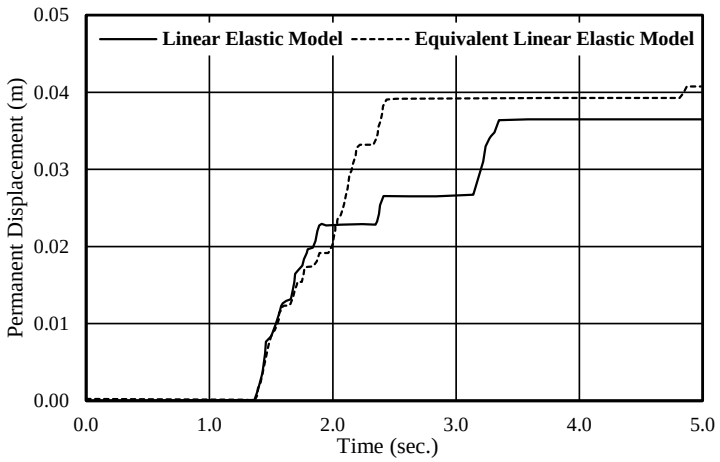


Figure 9. Permanent displacements of a wedge of 1.0h height of Kheyrabad dam under Naghan scaled earthquake

Table 9. Comparison of calculated acceleration and displacement in Kheyrabad Dam using different methods

Analysis Method	Wedge Depth	Maximum Acceleration (g)	Critical Acceleration (g)	Maximum Displacement (cm)	Analysis Method	Maximum Acceleration (g)	Critical Acceleration (g)	Maximum Displacement (cm)
Sarma	0.2h	0.64	0.46	7.2	quake/w Linear Elastic Model	0.24	0.46	0.0
	0.4h	0.45	0.30	6.8		0.23	0.30	0.0
	0.6h	0.32	0.29	0.10		0.21	0.31	0.0
	0.8h	0.25	0.29	0.0		0.19	0.29	0.0
	1.0h	0.18	0.24	0.0		0.17	0.24	0.0
Ambraseys – Sarma	0.2h	0.81	0.48	18.0	Linear elastic and developed code	0.449	0.46	0.0
	0.4h	0.70	0.43	13.8		0.441	0.30	2.8
	0.6h	0.52	0.41	2.9		0.447	0.31	2.1
	0.8h	0.42	0.40	0.1		0.532	0.29	2.4
	1.0h	0.33	0.38	0.0		0.450	0.24	3.6
Seed-Makdisi	0.2h	0.71	0.46	6.9	Equivalent Linear and developed code	0.559	0.38	1.8
	0.4h	0.50	0.30	5.2		0.557	0.25	4.0
	0.6h	0.42	0.29	2.6		0.541	0.29	3.4
	0.8h	0.31	0.29	0.0		0.528	0.23	3.8
	1.0 h	0.23	0.24	0.0		0.555	0.18	4.1

As it can be seen in table 7, the results of the calculations using the developed code are significantly different from the results of classic methods and are lower than them. Also, the results of the equivalent linear model are more accurate and closer to the measurements. Fig. 8 shows that till the 1.9 sec time (between 1.7 and 2.1 sec), the permanent displacements in the equivalent linear model is close but less than the results of linear elastic model. However, after that, the results of permanent displacements of the equivalent linear model increases and becomes higher than the results of the linear elastic model. The developed code was used for calculations in both cases. This was due to the fact that the levels of strains induced in the dam body grew in the time range of zero to about 1.9 seconds were very low. On the other hand, according to the fig. 7, the shear modulus functions of the dam body materials start dropping after a specific strain, and the shear modulus decreases rapidly afterwards. Also, the strains in the intended wedge of the dam body, at about 1.9 seconds, correspond to the strains at which the shear modulus curve drops rapidly. It worths to note that the reason for the variability of the time of start of this changes between 1.7 and 2.1 seconds for different intended wedges is the changes in percentage of different materials constituting the wedges. A high ratio of the shallow wedges bodies consists of the core materials, but this ratio decreases gradually as the depth of the wedges increases and the percentage of the shell materials increases. Therefore, in shallow wedges, as the shear modulus of core materials starts reducing at higher strains compared to shell material, the time the equivalent linear permanent displacement exceeds the elastic linear permanent displacement is longer, 2.1 sec. However, in deep wedges, where the wedge body material is consists of the shell material, this time is reduced to 1.7 seconds.

Another point obtained from the tables is that the amount of displacement in the different classic and numerical methods differs. The calculated displacements in the models are all within the range of low displacements, but what is important is to note that when displacement occurs in a wedge, the safety factor of that wedge will be less than one. At same time, the safety factor obtained in numerical methods is very high and sometimes more than two.

On the other hand, based on the results obtained, it was found that despite the higher maximum acceleration applied to the dam crest in the linear elastic model, the crest displacement in this model is less than the equivalent linear model. The reason for this observation is the decrease of the shear modulus ratio and increase in damping ratio versus increasing shear strain.

In the linear elastic model, the damping ratio and shear modulus are constant. However, in the equivalent linear model, the damping ratio increases with strain, as a result of which, the accelerations of the dam crest decrease, on the other hand, the ratio of shear modulus decreases with strain, which increases the displacement of the dam crest in this model as compared to the linear elastic model. In the equivalent linear model, the displacement of the dam crest increases initially but subsequently decreases. The is attributed to using the damping function in the equivalent linear model instead of a constant damping. The results showed that the shape of the wedges formed in the dam body is entirely different from what Ambraseys and Sarma [6] proposed as the critical wedges. Therefore, the average critical acceleration of the wedges will not be consistent with the results of this method either. It may worth mentioning that Ambraseys and Sarma [6] proposed this shape of the critical wedge in order to reduce of the number of the variables, and to simply the calculations. The results of the Sarma, Seed-Makdisi, Newmark (SLOPE/W), and finite element methods are presented separately in Table 9. It was observed that the displacements obtained from the classic methods, and the elastic linear model in the dynamic analysis performed using SLOPE/W, are very high. One of the reasons for this is the use of a linear elastic model for the soil. Majority of the classic methods are based on assuming a linear elastic model for soil materials. While the linear dynamic analysis is suitable only for structures consisted of stiff materials and subjected to low vibrations amplitudes. The domain of elastic behaviour of soil material is very limited, and nonlinear analysis is necessary. This finding is in agreement with the findings of some previous studies such as [47], [48] and [49]. Another considerable point in Table 9 is the significant difference between the results of the equivalent linear model in the SLOPE/W analysis and the analyses performed using the developed code. The classic methods widely used so far have been very conservative, leading to an increase in the time and costs of construction work. This highlights the need to use numerical methods and more accurate constitutive models.

4. Conclusions

In the linear elastic model, the displacements increase with the increase in natural period and decrease in the material stiffness. Nevertheless, in the equivalent linear model, the displacements depend on the shear modulus and damping ratio which depend on strain level. As the equivalent linear model represents the behavior of soil materials more realistically, it is crucial to determine the strain-dependent shear modulus and damping ratio functions.

In homogeneous dams, the average of accelerations calculated by all different methods is higher for more shallow wedges and decreases with increasing the wedge depth. However, for non-homogeneous dams which include core, shell, and filter zones, the average acceleration of the wedge depends on the wedge location and the materials it passes through due to the different damping ratios of these materials.

The results of classic methods are often overestimated, leading to significant increase in the project construction time and cost.

The results proved that the Ambraseys-Sarma method yields very unrealistic estimates of the maximum acceleration applied to a wedge of a given depth. In Ambraseys-Sarma method it is assumed that the wedges pass through the center of the dam and consequently through the core, while analyses show that most of the wedges pass through the downstream shell, posing less threat to dam integrity. This is particularly important in dynamic analysis. The calculated permanent displacements of the Kheyrabad Dam under the design base earthquake for wedges with the depth of 0.6 and 1.0 dam height are 3.4 and 4.1 cm, respectively. While these values are higher than estimates from other methods, they are within acceptable limits.

References

1. Mononobe N, Takata A, Matsumura M, (1936). Seismic stability of the earth dam. Proc. 2nd Congress on Large Dams, Washington DC, (4), 1435-
2. Terzaghi K, (1950). Mechanisms of Landslides. In Application of Geology to Engineering Practice, (S. Paige, ed.), pp: 83-125, Geological Society of America, New York, NY, USA.
3. Newmark N.M., (1965). Effects of earthquakes on dams and embankments. Geotechnique,15(2)139-
4. Goodman R.E., Seed H.B., (1966). Earthquake-induced displacements in sand embankments. Journal of the Soil Mechanics and Foundations Division 90(SM2), 125-
5. Seed H.B., (1966). A Method for Earthquake Resistant Design of Earth Dams. Journal of the Soil Mechanics and Foundations Division. ASCE, 92(1),13–
6. Ambraseys N.N., Sarma S.K., (1967). The Response of Earth Dams to Strong Earthquakes. Geotechnique, 7, 18l-
7. Sarma S.K., (1973). Stability analysis of embankments and slopes. Geotechnique, 23 (3):423-
8. Sarma S.K., Bhave M.V., (1974). Critical acceleration versus static factor of safety in stability analysis of earth dams and embankments. Geotechnique, 24(4), 661-
9. Sarma S.K., (1975). Seismic stability of earth dams and embankments. Geotechnique, 25 (4): 743-
10. Makdisi F.I., Seed H.B., (1978). Simplified procedure for estimating dam and embankment earthquake-induced deformations. J. Geotech. Engrg., ASCE, 104, GT7, 849-
11. Seed H.B., (1980). Lessons from the performance of earth dams during earthquakes, Design of Dams to Resist Earthquake, ICE, London, 1980, 251-
12. Paskalov T.A., (1984). Permanent displacement estimation on embankment dams due to earthquake excitations. In proceedings of the Eighth World Conference on Earthquake Engineering, July 21-28, 1984, San Francisco, California, U.S.A. 7(D) 327-
13. Paskalov T.A., (1985). Earthquake induced deformations on earth-fill dams and rock-fill dams. International Journal of Soil Dynamics and Earthquake Engineering, 4 (1) 35–
14. Hynes-Griffin M.E., Franklin A.G., (1984). Rationalizing the seismic coefficient method. Miscellaneous Paper. GL-84-Vicksburg, Miss, USA: US Army Corps of Engineers Waterways Experiment Station.

15. Finn W.D.L., Yogendrakumar M, Yosida N, Yoshida H, (1986). Tara-3: A Program for Nonlinear Static and Dynamic Effective Stress Analysis. Soil Dynamics Group, University of British Columbia, Vancouver, B.C., Canada.
16. Daghigh Y, (1993). Numerical simulation of Dynamics Behavior of and Earth Dam During seismic loading. Thesis presented to Delf University of Technology Netherland in partial fulfillment of the requirement for the degree of Doctor in Technical sciences.
17. Cai Z, Bathurst RJ, (1995). Deterministic sliding block methods for estimating seismic displacements of earth structures. Soil Dynamics and Earthquake Engineering, 15 (4) 255–
18. Matsumoto N, (2002). Evaluation of permanent displacement in seismic analysis of fill dams. In Proc third US-Japan workshop on advanced research on earthquake engineering for dams, San Diego, 22-23 June.
19. Day R.W., (2002). Geotechnical earthquake engineering handbook. McGraw-Hill.
20. Swaisgood J.R., (2003). Embankment dam deformations caused by earthquakes. 7th Pacific conference on earthquake engineering, 13-15 February, University of Canterbury Christchurch, New Zealand, paper
21. Wang Z.L., Makdisi F.I., Egan J, (2006). Practical applications of a nonlinear approach to analysis of earthquake-induced liquefaction and deformation of earth structures. Soil Dynamics and Earthquake Engineering, 26(4), 231–
22. Han Y, Hart R, (2006). Application of a simple hysteretic damping formulation in dynamic continuum simulations. Proceedings of the fourth international FLAC symposium on numerical modeling in geomechanics, Madrid, Spain. Paper No. 04-R. Hart and P. Varona, Eds.
23. Bray JD, Travasarou T, (2007). Simplified procedure for estimating earthquake-induced deviatoric slope displacements. J Geotech Geoenviron Eng,133 (4) 381–
24. Sica S, Pagano L, (2009). Performance-based analysis of earth dams: Procedures and application to a sample case. Soils and Foundations, 49 (6) 921-
25. Rampello S, Cascone E, Grosso N, (2009). Evaluation of the seismic response of a homogeneous earth dam. Soil Dynamics and Earthquake Engineering, 29 (5) 782–
26. Jinto H, Davidson R, (2010). Earthquake –induced Displacements of Earth Dams and Embankments. Australian Geomechanics Journal, 45 (3) 65-
27. Jibson RW, (2011). Methods for assessing the stability of slopes during earthquakes—A retrospective. Engineering Geology, 122 (1-2) 43-
28. Hsieh SU, Lee CT, (2011). Empirical estimation of the Newmark displacement from the Arias intensity and critical acceleration. Engineering Geology, 122 (1-2) 34–
29. Davoodi, M., Honardoust, H., Jafari, K. (2013). Study the dynamic behaviour of high and short embankment dams under near-source and far-source earthquakes. Proceeding of 7th NCCE, Zahedan, I. R. Iran.
30. Dong WX, Xu WJ, Yu YZ, Lv H, (2013). Numerical analysis of earthquake response of an ultra-high earth-rockfill dam. Natural Hazards and Earth System Sciences, 1 (12) 2319–

31. Bandini V, Biondi G, Cascone E, Rampello S, (2015). A GLE-based model for seismic displacement analysis of slopes including strength degradation and geometry rearrangement. Soil Dynamics and Earthquake Engineering, 71 128–
32. Park DS, Kutter BL, (2015). Static and seismic stability of sensitive clay slopes. Soil Dynamics and Earthquake Engineering, 79 118-
33. Bray JD, Macedo J, Travasarou T, (2017). Simplified Procedure for Estimating Seismic Slope displacements for subduction zone earthquakes. J. Geotech. Geoenviron. Eng., 144 (3).
34. Ghahreman-Nejad, B., Kan, M. E. (2017). Seismic deformation analysis of embankment dams: A comparison between simplified and non-linear numerical methods. Proceedings of the 19th International Conference on Soil mechanics and Geotechnical Engineering, Seoul, Korea.
35. Chen H, Liu D, (2019). Stochastic finite element analysis of rockfill dam considering spatial variability of dam material porosity. Engineering Computations, 36 (9) 2929-
36. Rollo F, Rampello S, (2021). Probabilistic assessment of seismic induced slope displacements: an application in Italy. Bulletin of Earthquake Engineering, 19, pp:4261–
37. Mazaheri AR, Rozbahani MZ, Beiranvand B, (2020). Quasi-Static and Dynamic Analysis of Vertical and Horizontal Displacements in Earth Dams (Case Study: Azadi Earth Dam). J. Civil Eng. Mater .App., 4 (4) 223-
38. Cho Y, Rathje E M, (2022). Generic predictive model of earthquake-induced slope displacements derived from finite-element analysis. J. Geotech. Geoenviron, 148 (4) p:
39. Hwang YW, Rathje EM, (2023). Insights into seismic slope deformation patterns using finite element analysis. Soil Dynamics and Earthquake Engineering, 164, p:
40. Zhang, C.Y., Wu, Q., Li, D.Q., and Du, W. (2024). Estimating sliding displacement of slopes induced by earthquake sequences based on the finite element method. IOP Conf. Series: Earth and Environmental Science, GeoShanghai 2024 – Volume 1334 012038.
41. Sarma, S. K. Response and stability of earth dams during strong earthquakes. Misc. paper GL-79-13. Geotechnical Laboratory, U.S. Army Engineer Waterways Experiment Station, P.O. Box, 631, Vicksburg, Miss. 39180.
42. Geo-Slope International, Ltd. Geostudio, User manual, Calgary, Alberta, Canada, 1991-2008.
43. Liu C, Macedo J, (2022). Machine learning-based models for estimating seismically-induced slope displacements in subduction earthquake zones. Soil Dynamics and Earthquake Engineering, 160, p.
44. Le PH, Nishimura SI, Nishiyama T, Fang C, Nguyen TC, (2022). Seismic Deformation of Earth Dams: A State-of-the-art Review. Reviews in Agricultural Science, 10, pp:138-
45. Wang MX, Li DQ, Liu Y, Du WQ, (2022). Probabilistic decoupled approach to estimate seismic rotational displacements of flexible slopes considering depth-dependent soil variability. Acta Geotechnica, 17 (4), pp:1551-
46. Bassal PC, Oathes TJ, (2024). Sliding Mass Period for Seismic Displacements of Spatially Variable Slopes. In Geo-Congress 2024, pp. 351-

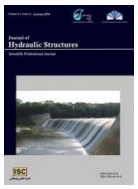
47. Rathje EM, Bray JD, (2000). Nonlinear coupled seismic sliding analysis of earth structures. Journal of Geotechnical and Geoenvironmental Engineering, 126, pp: 1002-
48. Meehan CL, Vahedifard F, (2013). Evaluation of simplified methods for predicting earthquake-induced slope displacements in earth dams and embankments. Engineering Geology, 152 (1) 180–
49. Ghahreman-Nejad, B., Taiebat, H. A., Noske, C., and Murphy, D.
50. Seismic response and dynamic deformation analysis of SarCheshmeh tailings dam. Proceedings of the 2nd International FLAC/DEM Symposium in Numerical Modeling. Melbourne, Australia: Itasca.



© 2024 by the authors. Licensee SCU, Ahvaz, Iran. This article is an open access article distributed under the terms and conditions of the Creative Commons Attribution 4.0 International (CC BY 4.0 license) (http://creativecommons.org/licenses/by/4.0/).



Journal of Hydraulic Structures
J. Hydraul. Struct., 2025; 11(1): 89-110
DOI: 10.22055/jhs.2024.47326.1307



OPEN ACCESS

Integrating Fuzzy Logic and Numerical Modeling for Analyzing Wave Patterns: A Study of the Makran Coastline

Maryam Rahbani[1]
Danial Ghaderi [2*]

Abstract

The Makran coastline, a strategic maritime region, has remained understudied regarding its hydrodynamic behavior. This study applies numerical simulations to analyze wave patterns in the northern Gulf of Oman, focusing on wave height (H_S), power (P), and mean wave direction (MWD) through Fuzzy Logic transformation and overlaying techniques. Seasonal and annual variations reveal that H_S ranges from 0.07 to 1.9 m, peaking during the summer with an average of 0.7 m, while winter and spring exhibit calmer conditions with an average H_S of 0.4 m. Wave power (P) shows a marked increase in summer, reaching up to 10.2 kW/m, with an annual mean ranging from 0.02 to 5.3 kW/m. Wave direction shifts seasonally, predominantly from 171° to 247° during winter and spring, and between 189° to 191° in summer and autumn. Spatial analysis highlights intensified hydrodynamic activity in the eastern region, influenced by oceanic conditions and the monsoon, while the western sector remains relatively calmer. Omega-shaped coasts and bays demonstrate more stable conditions, whereas headlands and capes experience significant hydrodynamic intensification. These findings provide critical insights for coastal management and sustainable development, enabling policymakers to balance maritime potential with risk mitigation. By integrating hydrodynamic dynamics into coastal planning, resilient strategies can be established for the sustainable utilization of the Makran region's resources.

Keywords: Makran; Gulf of Oman; Significant Wave Height; Wave Power; MIKE 21.

Received: 03 July 2024; Accepted: 11 September 2024

1. Introduction

The coastline has perpetually captivated human societies, serving as a focal area for settlement and development. Over 40% of the global population resides within 100 km of the coast [1], driven by factors such as food security, ocean transportation, and favorable climatic conditions [2,3].

*Email: danialghaderi.phd@hormozgan.ac.ir, danialghaderi1@gmail.com
[1] Department of Atmospheric and Oceanographic Science, Faculty of Marine Science and Technology, University of Hormozgan, Bandar Abbas, Iran.
[2] Researcher at Center Providing Consultation And Simulation Services For Coastal And Marine Environments (NPDS Company), Bandar Abbas, Iran.

However, these regions face significant challenges, such as coastal erosion and inundation [4,5]. These challenges, often driven by weather patterns and hydrodynamic behaviors in seas and oceans, pose serious threats to coastal human settlements [6,7]. Understanding the hydrodynamic conditions of coastal regions, as well as the morphological responses of shorelines to these conditions, is essential for effective coastal development [8].

One of the key regions where such an understanding is required is the west part of the Makran coast. This coastal area, located in the northern Gulf of Oman, is characterized by its dry and windy conditions, with limited rainfall and the presence of several seasonal rivers [9]. Despite some human settlements, this region remains sparsely populated. Development plans, however, have designated this coastal region for significant marine development, increasing the need to understand its hydrodynamic patterns. Therefore, the objective of this study is to analyze the patterns of hydrodynamic variables along this coastline, with a focus on integrating them using Fuzzy Logic techniques.

Some investigation of hydrodynamic conditions had been conducted in the coastal and offshore area of the northern Gulf of Oman through numerical simulation studies. For instance, Allahdadi et al., [10] utilized the MIKE 21 Spectral Waves (SW) to simulate the waves due to the Cyclone Gonu in June 2007 in the Gulf of Oman. The model was calibrated using data from the Chabahar buoy. The numerical model was used to analyze the behavior of Cyclone Gonu, starting from its formation in the Arabian Sea. In another research, utilizing the coupled models MIKE 21 SW and MIKE 21 hydrodynamic (HD), Moghaddam et al., [11] examined the local wave and wave-induced currents in Ramin Port, located in the northern part of the Gulf of Oman. The primary objective of utilizing the model was to find solutions for the sedimentation issues occurring within the port basins. The model encompasses both regional and offshore domains and has been validated using data from the Chabahar buoy. In order to examine the effects of constructing Beris port in the northern Gulf of Oman, Sayehbani and Ghaderi, [12] conducted a study on the hydrodynamic conditions of the area. They compared the conditions before and after the construction of the breakwater, focusing on the months of July and August when wind activity is quite strong. To analyze the wave pattern and current behavior near the port and its potential impact on sedimentation, they utilized the MIKE 21 SW and MIKE 21 HD models. In continuation of the studies on the impact of the construction of Beris Port, Ghaderi and Rahbani, [13] conducted a simultaneous investigation using hydrodynamical simulation and remote sensing (RS) imagery. They expanded the spatial and temporal range of their study to analyze the wave and current patterns as well as long-term shoreline changes. For the hydrodynamical study, they utilized the MIKE 21 Coupled model, ECMWF wind and wave data, and Chabahar buoy wave data. The findings of their study highlight the sedimentation problems faced by the port and its surrounding beaches. Armanfar et al., [14] utilized climate change scenarios to evaluate the vulnerability of the coastal areas in the Chabahar region (in the northeast part of the Gulf of Oman). They employed MIKE 21 numerical modeling to simulate the potential impacts of sea level rise, changes in significant wave height, and alterations in tidal patterns. The assessment focused on estimating possible changes until the year 2100. The findings indicated that a significant portion of the coastal zones in the Chabahar area face the risk of inundation due to sea storms and potential climate change. Siahsarani et al., [15] conducted a study focused on the analysis of Cyclone Gonu behavior and its impact on the storm surge in the Gulf of Oman. They conducted a numerical simulation that involved coupling wave and hydrodynamic models, specifically using MIKE 21 SW and MIKE 3 HD, along with measured data. The aim of the study was to investigate the role of variables in the model setup and their influence on coastal areas while studying the behavior of Cyclone Gonu. Foroutani et al., [16] investigated Tropical Cyclone Ashobaa in the Gulf of Oman

through numerical simulation. Their findings indicated that during storm conditions, there are substantial changes in water level, current speed, and even current direction in the Chabahar region.

While previous studies have provided valuable insights into the hydrodynamics of specific events or locations, none have offered a comprehensive assessment of wave patterns across the entire Makran coast. This study aims to fill this gap by using numerical simulations to analyze the spatiotemporal behavior of hydrodynamic variables along the Makran coastline, specifically focusing on wave height, wave power, and wave direction. The novelty of this research lies in the detailed analysis of wave patterns with sufficient accuracy to support coastal development projects in the region. To gain a comprehensive understanding of the hydrodynamic conditions, variables such as wave height (H_S), power (P), and mean wave direction (MWD) are integrated using Fuzzy Logic techniques. This approach allows for a more realistic description of the hydrodynamic environment, representing a significant innovation in the study of coastal hydrodynamics. Furthermore, it provides a clearer assessment of the region's potential for sustainable development while mitigating hydrodynamic risks.

2. Method

2. Study Area

Makran coast stretches along the Gulf of Oman for approximately 550 km (Fig. 1) [17]. This region is receiving significant attention from politicians and administrators, as it has been identified as an area with great potential for maritime development [18]. The development of marine industries along this coastline is still in its early stages. There are still no large-scale industries or ports in the area, but they are included in future development plans. Due to its proximity to the Arabian Sea and Indian Ocean, the region is constantly influenced by the climatic conditions of the northern Indian Ocean and the monsoon [19,20]. Additionally, previous reports and studies have highlighted the region’s vulnerability to tsunamis [21,22] and rising sea levels [23]. Makran coastal region encompasses a variety of landforms, such as sand spits and barrier islands primarily located in the western part of the region (Codes 2, 5, 8-11 and 15 in Fig 1). Additionally, there are mangrove forests and estuaries in both the eastern and western areas (Codes 2, 8, 11, 15, 29 and 30 in Fig 1). High beaches and rocky coastline are spesifically the characteristics of eastern part (Codes 17, 23, 24, 26, and 28 in Fig 1). Human settlements can also be found in both the eastern and western parts (Codes 6, 23, 24, and 28 in Fig 1). There are only two notable ports, namely Jask (Codes 6 in Fig 1) and Chabahar port (Codes 23 in Fig 1), in the area. These ports are both large and significant in terms of their infrastructure and capacity. The offshore part of the Makran region is significantly deep, reaching up to 2500-3000 m (Fig 1 C). Given the geomorphological diversity of the Makran region, with its eastern part adjacent to oceanic waters and its western part more distant from oceanic influence, it is essential to conduct a precise analysis of the hydrodynamic conditions, taking into account these variations. This study aims to address this gap by providing a detailed examination of these hydrodynamic differences.

Despite the presence of several rivers, the area is generally characterized as dry and semi-arid, resulting in low water levels or complete dryness for most of the year. The majority of rainfall occurs during the winter season, specifically during the winter monsoon period [24]. The wind patterns in the eastern and western parts of the study area differs. In the western part, the prevailing wind direction is from the W and E, with wind speeds exceeding 6 m/s from the W and NW. In the eastern part however, the wind primarily blows from the SE, with a secondary direction of W-SW [13]. The maximum wind speed in the southeast direction reaches up to 8 m/s. Figure 1 shows the bathymetry of the region utilizing GEBCO, and local depth data. To enhance the dissemination

of the findings, 30 major cities/villages of the area are identified in the figure, labeled as numbers 1-30 (Table 1).

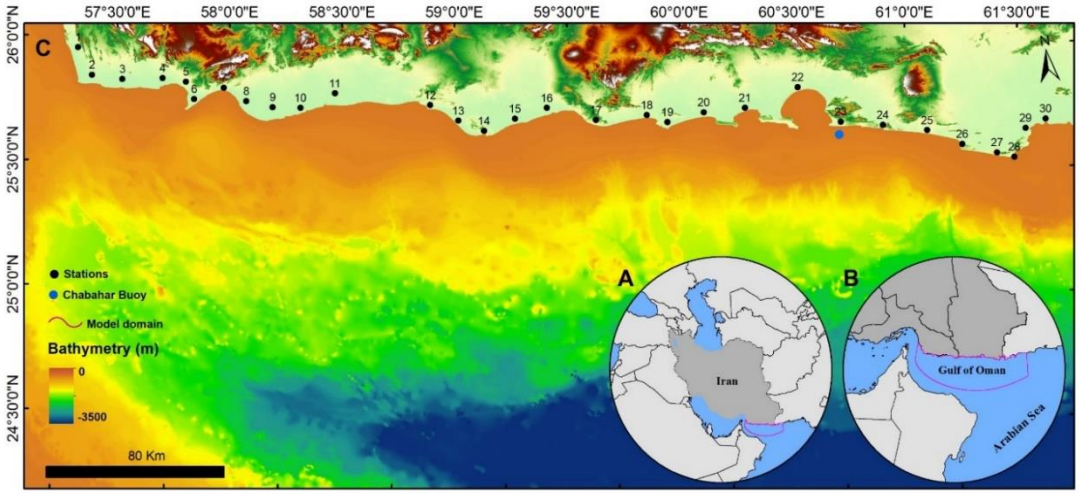


Figure 1. A & B) location of the study area, and C) Bathymetry of the area

Table 1. Location of zones in the study area

Zone	Name	Lat (°N) Long (°E)	Zone	Name	Lat (°N) Long (°E)	Zone	Name	Lat (°N) Long (°E)
1	Bunji-ye Karbasi	25.93048 57.31323	11	Gabrik & Jask Protected Area	25.64053 58.43555	21	Pozm Bay	25.39705 60.24757
2	Kuh Mobarak	25.81495 57.36336	12	Gougsar	25.55259 58.85217	22	Chabahar Bay	25.45441 60.49167
3	Gāvbandi	25.78589 57.49725	13	Lirak	25.47730 58.96959	23	Chahbahar	25.29404 60.66402
4	Rig	25.77291 57.67578	14	Kalirak	25.42460 59.07945	24	Lipār	25.26020 60.84942
5	Jāsk-e-kohne	25.74879 57.77878	15	Khowr Rapch	25.45963 59.22262	25	Rudik-e Molladad	25.21703 61.04211
6	Jask	25.67641 57.80693	16	Khowr Galak	25.48877 59.36922	26	Beris	25.14394 61.18974
7	Hojdān	25.70982 57.94357	17	Kalāt	25.41747 59.58070	27	Poshot	25.09217 61.33887
8	Shahreni	25.64608 58.03730	18	Birdaf	25.41375 59.80901	28	Pasabandar	25.06598 61.41234
9	Karap	25.61141 58.15128	19	Tang	25.37591 59.89553	29	Mangrove Gwadar	25.17594 61.47860
10	Khowr Jagin	25.59748 58.27522	20	Gurdim Bay	25.39829 60.06286	30	Khowr Bahokalat	25.20328 61.57267

2.2. Numerical Model Description

To assess the characteristics of waves in the Makran region, we have utilized the numerical model MIKE 21, which was developed by the Danish Hydraulic Institute (DHI) [25]. Although

various other numerical models, such as WAM [26], WW3 [27], SWAN [28], TOMAWAC [29], and ROMS [30], are available for simulating hydrodynamic conditions, MIKE 21 was selected due to its exceptional performance, comprehensive tools for data preparation and output analysis, and proven accuracy in numerous studies [12,13,31–35]. The MIKE 21 model is highly capable and widely employed for simulating wave and current characteristics in various environments, including river entrances, gulf interiors, coastal areas, as well as shallow and deep waters [11,12,26,31]. It is developed based on the fundamental principles of shallow water equations and the depth-integrated incompressible Reynolds averaged Navier-Stokes equations. The Spectral Waves (SW) module is designed to simulate the growth, decay, and transformation of wind-generated waves and swell in offshore and coastal areas. In this module, the waves are characterized using the density spectrum $N(\sigma,\theta)$, where σ represents the relative angular frequency ($\sigma = 2\pi f$) and θ represents the direction of wave propagation. The equation that governs the behavior of these waves is the wave action balance equation, which can be expressed in either cartesian or spherical coordinates (Eq. 1).

$$\frac{\partial N}{\partial t} + \nabla.(\vec{v}N) = \frac{s}{\sigma} \quad \rightarrow \frac{\partial}{\partial t}N + \frac{\partial}{\partial x}C_x N + \frac{\partial}{\partial y}C_y N + \frac{\partial}{\partial \sigma}C_\sigma N + \frac{\partial}{\partial \theta}C_\theta N = \frac{s}{\sigma} \tag{1}$$

where N represents the density of wave action, C_x, C_y, C_σ, and C_θ are parameters describing the velocity of the wave in geographical and spectral coordinate systems, and the term 's' represents the combination of five distinct energy sources, as described in Eq. 2.

$$s = s_{in} + s_{nl} + s_{ds} + s_{bot} + s_{surf} \tag{2}$$

In the context of energy generation, s_{in} represents the wind-generated energy, s_{nl} represents the transfer of wave energy resulting from the interaction between waves, s_{ds} accounts for the dissipation of wave energy caused by white capping, s_{bot} refers to the dissipation due to bottom friction, and s_{surf} represents the dissipation of wave energy resulting from breaking induced by changes in water depth [25,26,36].

Utilizing the spectral wave simulation feature within the MIKE 21 software package, spectral moments of order i are calculated using equation 3 to ascertain spectral wave parameters.

$$m_i = \int_0^{2\pi}\int_0^{\infty} E(f,\theta)\, f^i df\, d\theta, \tag{3}$$

where $E(f,\theta)$ denotes the directional wave energy spectrum, and f denote the wave frequency.

In the following, the key parameters associated with wave characteristics—namely, significant wave height (H_s), mean wave period (T_m), and energy period (T_e)—are determined using the following equations.

$$H_s = 4\sqrt{m_0} \tag{4}$$

$$T_m = \frac{m_0}{m_1} \tag{5}$$

$$T_e = \frac{m_{-1}}{m_0} \tag{6}$$

The wave power, denoted as the energy flux per unit crest length (P), is computed through the application of the directional wave power formulation, as expressed in Eq. 7.

$$\vec{P} = \rho g \int_0^{2\pi} \int_0^{\infty} \overrightarrow{C_g}(f,\theta)\, E\,(f,\theta) df\, d\theta, \quad (7)$$

where ρ, g and C_g are the density of seawater, the acceleration due to gravity, and group velocity respectively.

The wave power flux (P), in kW/m, can be calculated using Eq 8 [37,38].

$$P = \frac{\rho g^2}{64\pi} H_s^2 T_e \approx 0.49\, H_s^2 T_e, \quad (8)$$

2.3. Model Settings and Calibration

A mesh file prepared for the simulation comprising 6636 nodes and 10335 elements, and forming a flexible triangle. Three different mesh zone considered for the area (Fig. 2), where thinner mesh used for near shore area. The modeled area includes one land boundary (yellow line in Fig. 2), and three open boundaries of the eastern (green line in Fig. 2), the western (red line in Fig. 2), and the southern boundaries (blue line in Fig. 2). The bathymetric data is derived from the modified GEBCO data, and local nearshore data from Chabahar buoy (Fig 1C).

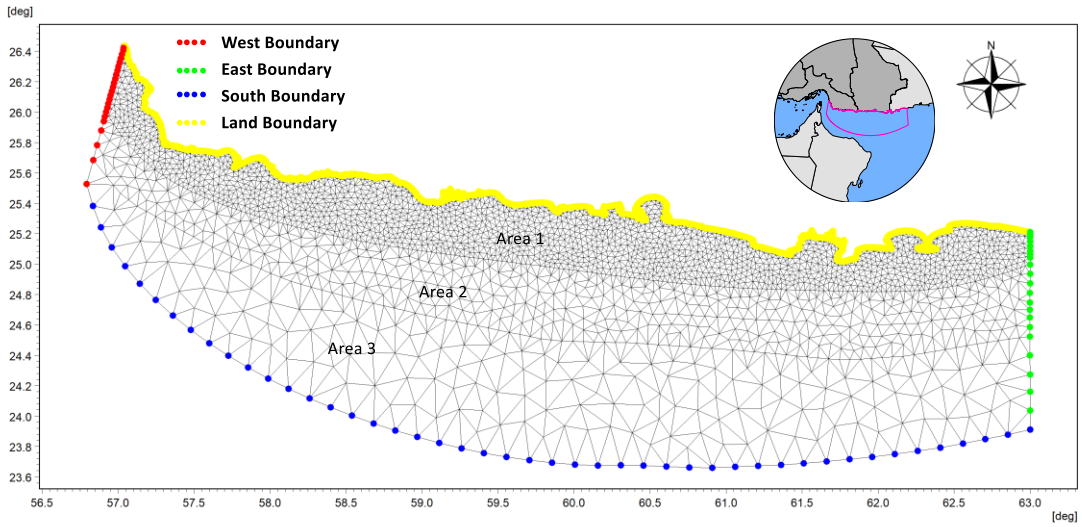


Figure 2. Mesh file with three open boundaries in the east (green), west (red) and south (blue)

Wind data obtained from European Centre for Medium-Range Weather Forecasts (ECMWF) ERA-40 [39] with a time step of 6 hours. The data is formatted as u and v components, with a spatial resolution of 0.125˚ × 0.125˚. (Fig. 3). According to the fig. 3 maximum wind speed is about 4 m/s. In the eastern part of the area, the prevailing wind direction is from the SE. In the central part, the wind speed is lower and predominantly originates from the E. In the western part, the prevailing wind direction is mostly from the NE.

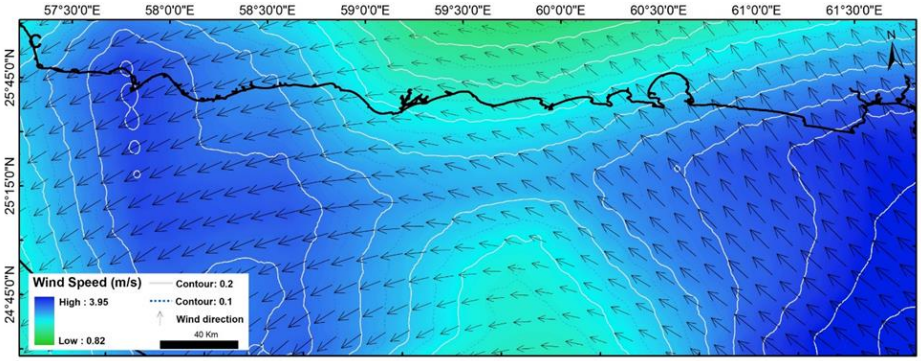


Figure 3. The Averaged wind speed and direction, of the year 2018, over the area, derived out from ECMWF ERA-40

Significant wave height (H_S), Spectral peak period (Tp), and Mean Wave Direction (MWD) are variables obtained from the ECMWF ocean model to utilize to the three open boundaries of the model. Initial conditions were set according to Anton et al., [40] and Ghaderi and Rahbani, [13] studies in the form of JONSWAP spectrum with a fetch of 100 km.

The calibration of the model involved the selection of specific coefficients related to wave breaking, bottom friction, and white capping parameters [12,13,31,40]. To optimize the results, various coefficient values were employed across multiple model iterations. Following extensive simulations and a thorough review of analogous studies, the selected parameters were: for wave breaking, Gamma was set to 0.8 and Alpha to 1; for bottom friction, Nikuradse roughness was set to 0.04; and for white capping, cdis was set to 4.5 and Delta to 0.05.

2.4. Model Validation

Following the enhancement of the model's performance, an evaluation was conducted, comparing H_S values simulated by MIKE 21 SW with those from the ECMWF ocean model data at the specified location illustrated in Fig. 2 (Fig. 4). Statistical parameters are imployed assess the quality of the model results [40,41]. The Correlation Coefficient (CC) [42] demonstrates a strong correlation between the patterns of both data series, with a value of 0.95. This parameter for the same region is reported as 0.98 by Ghaderi and Rahbani, [13]. The Root Mean Square Error (RMSE) [43] is calculated as 0.14, the Bias parameter (BIAS) [44] is derived as -0.02, and Dispersion Index (SI) [45] is computed as 13.8%. These statistical values implied that model results in this investigation are reliable.

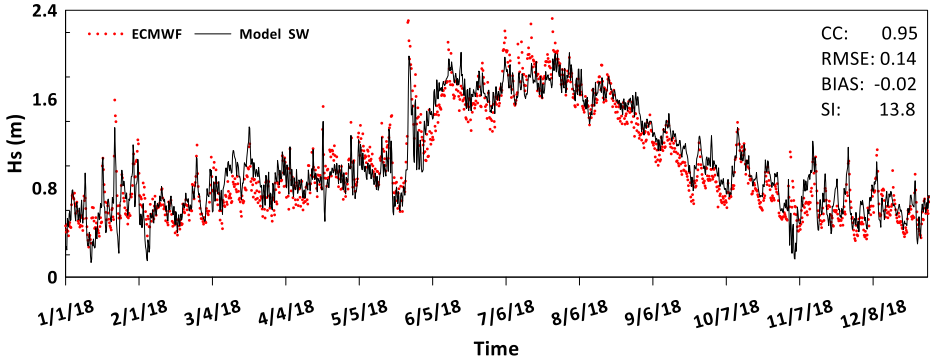


Figure 4. Comparison of the H_S obtained from the simulated MIKE 21 SW model and the ECMWF ocean model data in 2018

2.5. Fuzzy standardization and overlay

After completing the numerical model and obtaining the outputs from the spectral wave model, this study employs Fuzzy Logic to integrate the values of these variables in a comprehensive manner. This integration allows for a simultaneous consideration of all variables [35,46], thereby providing a detailed description of the wave patterns along the Makran coastline. We employed Fuzzy Logic [47] to combine the values of three variables, H_S, P, and MWD, to identify the sensivity of the region in response to the combination of these variables. Prior to the overlaying phase, it is necessary to standardize each variable, taking into account their diverse units and numerical ranges. In this study, standardization is achieved through the utilization of Fuzzy membership. Fuzzy membership assigns values to each variable within the range of zero to one, depending on the adopted concept [48–50].

In the sea and coastal zone, wave height serves as an indicative parameter of sea state [51], where higher fuzzy membership values signify a higher sea state. The variable H_S is standardized using the Linear function with the min and max values of 0 and 2.2m (highest observed value) respectively. Fig. 5 A illustrates annual average of H_S and corresponding fuzzy membership values within a one-km buffer from the Makran shoreline. Within this buffer, the maximum and average H_S are 1.06 and 0.58 m, respectively, yielding fuzzy membership values of 0.48 and 0.26 consequently (Table 2). Wave power denotes the rate of wave energy transfer (to the coast) [52], and regions with higher fuzzy membership values experience greater wave power. Increased wave power has the potential to increase erosion and flooding in coastal regions, while a substantial significant wave height indicates the presence of hazards and challenges in sea state [53,54]. Generally, greater wave height and a shorter wave period align with augmented risks and challenges in the sea state [55]. As a result, both variables are considered in this study. The P variable is subjected to standardization using the large function (midpoint=5, spread=5). The highest wave power value reaches up to 14 kW/m across the entire study area, primarily concentrated in the eastern part and during the summer period. Therefore, the midpoint of the large function is specified as 5. Fig. 5 B depicts the relationship between the annual average of P variable and the calculated fuzzy membership value within a one-km buffer from the shoreline. In this buffer, the maximum and average P values are 4.83 and 1.50 kW/m, respectively, resulting in fuzzy membership values of 0.46 and 0.04 consequently (Table 2). The MWD variable undergoes standardization through a Gaussian function (midpoint=180, spread=0.005). This standardization is based on the premise that waves approaching the coast at oblique angles are more likely to attack the coastal area [56,57]. Consequently, a reversal of the Gaussian function is required for this standardization. In this process, waves arriving from the southern side (180 degree) are assigned the lowest fuzzy membership value, while oblique waves receive the highest fuzzy membership value. Depicted in Fig. 5 C, the relationship between annual average of MWD and fuzzy membership (within a one-km shoreline buffer) is modeled using a Reverse Gaussian function. The mean is approximately 270° (StDev 17.6), with computed maximum and average fuzzy membership values of 1.0 and 0.66, respectively (Table 1).

Table 2. Annual average of Hs, P, and MWD variables for the year 2018 obtained from the output of the model and the standardized results through Fuzzy membership along the one-km buffer of Makran shoreline

Variable	Model output				Fuzzy membership				
	Min	Max	Mean	StDev*	Function	Min	Max	Mean	StDev
Hs	0.08	1.06	0.58	0.23	Liner	0.03	0.48	0.26	0.11
P	0.02	4.83	1.50	1.30	Large	0.00	0.46	0.04	0.09
MWD	106	269	196	17.63	Reverse Gaussian	0.00	1.00	0.66	0.31

*Standard deviation

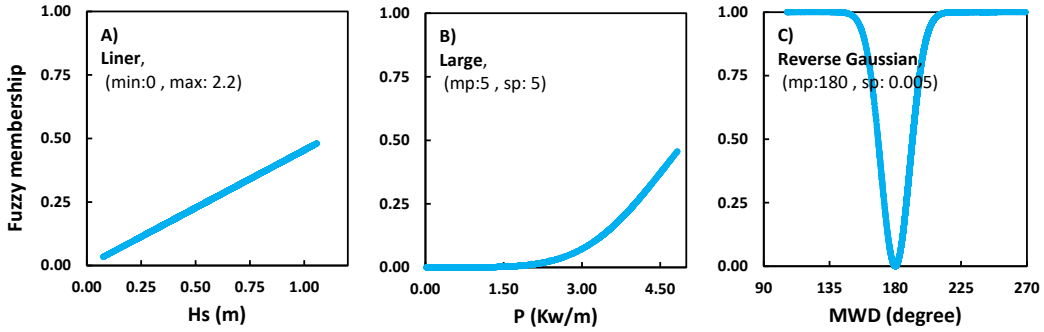


Figure 5. Annual averaged Hs, P, and MWD along the one-km buffer of Makran shoreline and their simultaneous fuzzy membership values (after standardized) through the introduced function.

To achieve overlaying, the fuzzy GAMMA operator was employed [58]. The principles of this operator are elucidated in Equation 9, encompassing both fuzzy sum and fuzzy product operators.

$$\mu_{Combination} = [1 - \prod_{i=1}^{n}(1-\mu_1)]^{\delta} \times \ [\prod_{i=1}^{n}\mu_1]^{1-\delta} \quad (9)$$

where, $\mu_{Combination}$ is the final result of the fuzzy combination, the μ_i is fuzzy value of each set i, δ is a weight parameter between 0 and 1, and, n is the number of fuzzy sets. The fuzzy GAMMA operator is governed by the δ parameter (gamma coefficient). Lower gamma coefficients mean low sensitivity class areas, while higher gamma coefficients signify areas with high sensitivity [59,60]. The selection of the δ parameter involves achieving a dynamic equilibrium between the impacts of augmenting and diminishing overlapping variables [59,61]. δ parameter should be chosen wisely in order to correctly signify the influence of combined parameter in the area. We employed the operator function for this reason. δ value of 0.9 has been selected to establish adaptable compatibility between escalating and diminishing trends.

3. Results and Discussion

3.1. Simulated variables

Considering the substantial variation in wave characteristics along the approximately 550 km Makran coast across different seasons, a brief overview of the seasonal conditions is first presented, followed by an explanation of the annual average results. The wave height (Hs) and wave power (P) along the Makran coast exhibit significant seasonal variations. In winter, the

eastern part faces higher H_S (up to 0.68 m) than the western part (less than 0.38 m), with coastal zones showing varying maximum H_S and P. Spring brings increased H_S and P, especially in the eastern regions, with H_S reaching up to 1.0 m and P up to 2.5 kW/m. Summer peaks with H_S up to 2.0 m in the east and maximum P reaching 13.5 kW/m in certain zones. Autumn sees a decline in H_S and P, resembling spring conditions, with H_S up to 1.0 m and P around 3.0 kW/m in the east. The direction of incoming waves shifts seasonally, primarily from the southwest in winter and spring, and from the south in summer and autumn (Table 3). Detailed illustrations and data for each season are provided in the appendix (A), with Fig. A1 to A4 depicting the averaged pattern of wave characteristics seasonally.

Table 3. Summary of seasonal variations in wave height (H_S) and wave power (P) along the makran coast

Season	Wave Height (H_S) (m)			Wave Power (P) (kW/m)			Wave Direction
	West	East	Notable Zones (Z)	West	East	Notable Zones (Z)	
Winter	< 0.38	0.68	Z 1-12: 0.36 m, Z 20-23: 0.4 m	Max: 0.45	Max: 1.0	Z 1-17: 0.45 kW/m, Z 17-28: 1.0 kW/m	Mainly SW, WSW in the west
Spring	< 0.48	1.0	Z 1-12: 0.52 m, Z 17-23: 0.78 m	Max: 0.65	Max: 2.5	Z 1-17: 0.65 kW/m, Z 17-28: 2.5 kW/m	Mainly SW, consistent with winter
Summer	2.0	< 0.80	Z 1-12: 0.84 m, Z 17-23: > 1.0 m	Max: 2.2	Max: 13.5	Z 1-10: 1.75 kW/m, Z 17-28: 13.5 kW/m	Mainly S, SW within the coastal zone
Autumn	< 0.5	1.0	Z 1-12: 0.60 m, Z 23-28: 0.94 m	Max: 1.0	Max: 3.0	Z 1-12: 1.0 kW/m, Z 19-28: 3.0 kW/m	Mainly S, similar to annual

Despite the existence of several studies on the Makran coast, a gap in detailed, region-specific data has remained. This study addresses this gap by focusing on coastal zones, analyzing H_S, P, and MWD data. The results illustrating the annual average wave pattern are presented in Fig. 6. In the eastern part, the maximal H_S reaches up to 1.2 m, while in the western part, it is under 0.6 m. Along the shoreline, from zone Bunji-ye Karbasi (1) to Gougsar (12), the maximum H_S is 0.60 m. Moving from zones Gougsar (12) to Kalāt (17), the maximal H_S increases to 0.78 m, and further east side from zone Kalāt (17) to Chahbahar (23) maximum H_S increases up to 0.87 m. Zones Chahbahar (23) to Pasabandar (28) encounter a maximal H_S of 1.0 m, whereas zones Pasabandar (28) to Khowr Bahokalat (30), situated in a deeper bay, experiences a maximal H_S of 0.8 m. The wave direction reveals two distinct zones, with the eastern part originating from the SbW direction and the western part from the SW direction. In coastal regions from zone Bunji-ye Karbasi (1) to Shahreni (8), the maximum P is 0.85 kW/m, escalating to 1.56 kW/m in zones Shahreni (8) to Khowr Galak (16), and peaking at 1.5 kW/m in zones Khowr Galak (16) to Pozm Bay (21). Zones Pozm Bay (21) to Chahbahar (23) exhibit a P surpassing 3.5 kW/m. Zones Chahbahar (23) to Beris (26) attain a maximal P of 4.5 kW/m, while zones Beris (26) to Pasabandar (28) reach a maximum of 5.2 kW/m. Finally, zones Pasabandar (28) to Khowr Bahokalat (30) register a P of less than 3.2 kW/m. These findings highlight a clear spatial variation in wave energy distribution along the Makran coast. This spatial heterogeneity suggests that coastal development and erosion mitigation strategies should be tailored to the specific wave dynamics of each region, particularly in the high-energy eastern zones where greater hydrodynamic forces pose increased risks to coastal

infrastructure. A notable example is the distinct hydrodynamic conditions at Beris Port, located in the eastern Makran region [12,13].

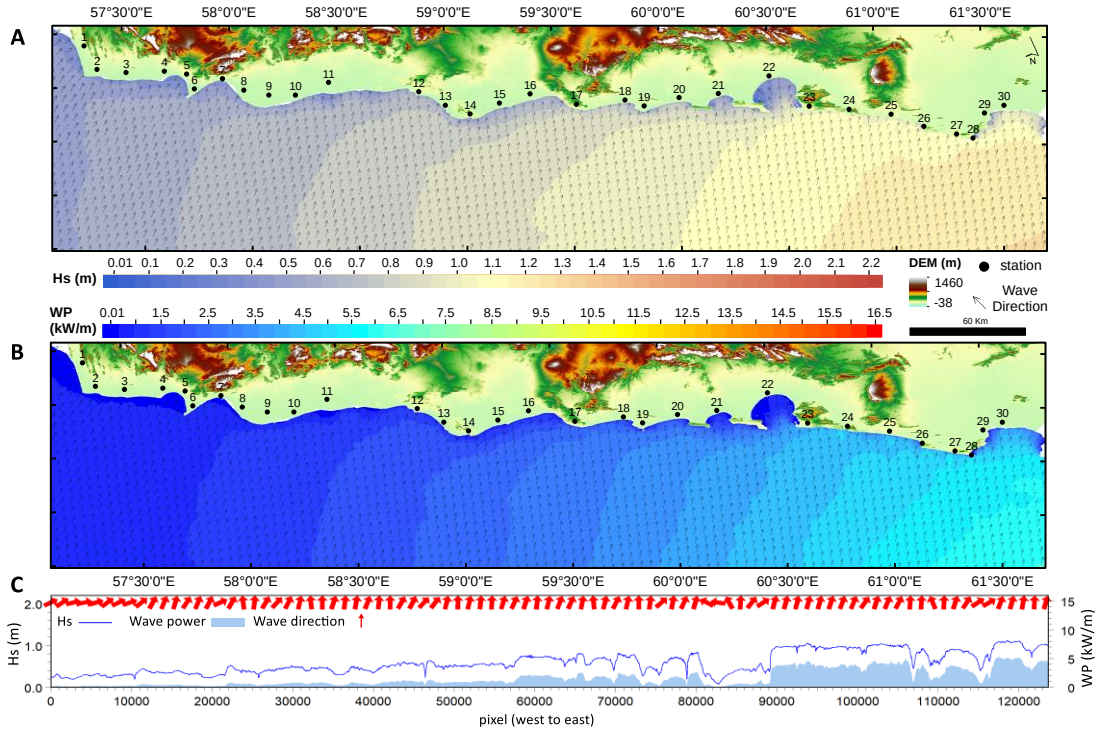


Figure 6. Annual pattern of A) averaged significant wave height, B) averaged wave power, and C) spatial variation diagram extracted from variables in a 1 km buffer from the Makran shoreline

To describe the temporal (seasonal and annual) variations of variables H_S, P, and MWD more specificly, box plots are used (Fig. 7 A-C). The spatial variations of H_S in the winter season are limited, ranging between 0.07 and 0.6 m, with an average of 0.4 m. During the spring season, H_S reached a maximum of 0.95 m with an average of 0.4 m, notably higher in the eastern half of the Makran region (Fig. A2, in Appendix). As the summer season commences, the most significant variations in H_S, up to 1.9 m with an average of 0.7 m, are observed throughout the entire area, with the eastern part experiencing higher H_S (Fig. A3, in Appendix). In the autumn season, H_S decreases, and the spatial variations in H_S resemble those in the spring season. The annual average spatial variations in H_S range from 0.08 to 1.1 m, with a mean of 0.5 m (Fig. 7A). The spatial and temporal variations in the variable P correspond to H_S (Fig. 7 B). The spatial variations of P in the spring season range from 0.0 to 1.08 kW/m, with a mean of 0.3 kW/m. In the summer season, spatial variations exceed 10.2 kW/m, with an average of 2.0 kW/m. The annual average spatial variations in P range from 0.02 to 5.3 kW/m, with a mean of 0.9 kW/m. Saket and Etemad-Shahidi, [62] conducted an investigation into the long-term wave power within zones Kalirak (14), Tang (19), Gurdim Bay (20), and Chabahar Bay (22), asserting that the monthly mean P fluctuates between 0.97 and 5.16 kW/m. Their findings are in concordance with the results of this study. In the spring season, the spatial variations of MWD range from 171 to 247 degrees, with an average of 208 degrees, and a similar pattern is observed in the spring, with the difference that directional dispersion increases. In the summer and autumn seasons, the pattern of spatial and temporal

variations in MWD is similar, with mean values of 191 and 189 degrees, respectively. Ghaderi and Rahbani's (2023) investigation also elucidates that the directional dispersion of waves along the coastal region exhibits greater diversity during the winter season in contrast to other temporal periods. The annual average spatial variations in MWD are within the range of 159 to 237 degrees, with a mean of 197 degrees (Fig. 7 C). The long-term analysis conducted by Saket and Etemad-Shahidi, [62] delineates the wave climate into three distinct temporal phases: the initial period spans from January to May, succeeded by a segment from June to August, and concluding with a phase spanning from September to December.

Since the area under investigation is faced with open ocean, the verity of winds are dominared in the area, which differes seasonally. At the onset of winter, wind speeds decrease, whereas during summer, the presence of the monsoon intensifies, leading to the formation of persistent southerly to southwesterly winds [19,62]. Consequently, the region's wave pattern is influenced by seasonal variations in wind, thus, the height, power and direction of waves are videly different season by season. These findings indicate that the distinct seasonal shifts in wave characteristics, particularly during the summer monsoon, can significantly affect sediment transport and coastal morphology. The variation in wave energy throughout the year suggests that coastal engineering solutions should be dynamic and flexible, taking into consideration not only the seasonal intensity of wave action but also the long-term impacts on shoreline stability and erosion patterns [63].

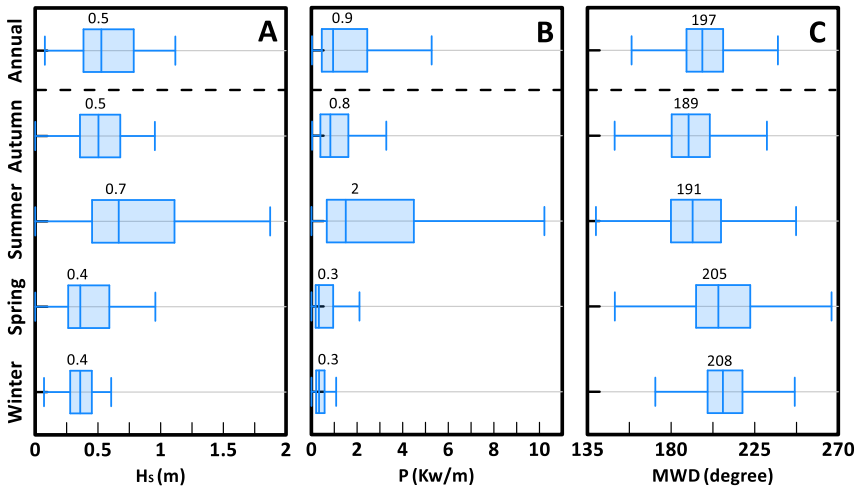


Figure 7. Box Plot of A) significant wave height, B) wave power, and C) mean wave direction (seasonally and annualy)

3.2. Overlaying variables

Overlaying three variables of H_S, P and MWD, the area were categorized and illustrated seasonally (Fig. 8 A-D), and annually (Fig. 8 E). During the spring season, the difference between the eastern and western regions is not pronounced, especially in coastal areas, which exhibit minimal conditions (Fig. 8 A). However, in the spring and summer seasons, the stark disparity and delineation of conditions between the eastern and western regions become highly evident (Fig. 8 B-C). This demarcation extends up to zone Kalāt (17) in the spring and penetrates up to zone 6 in the summer. In the autumn season, this demarcation reaches its maximum extent, up to zone Poshot (27) (Fig. 8 D). The results of overlaying the annual averages also indicate that this difference between the eastern and western sectors persists up to zone Kalāt (17). These findings highlight significant seasonal and spatial variations within the study area. Briefly, the eastern

region consistently exhibits higher scores compared to the western counterpart. The eastern region, adjacent to the Arabian Sea - Indian Ocean, is influenced by oceanic conditions and monsoon [11,19,64], while the western region is situated away from oceanic influences, there is a considerable reduction in depth, and the water body exhibits a semi-closed configuration.

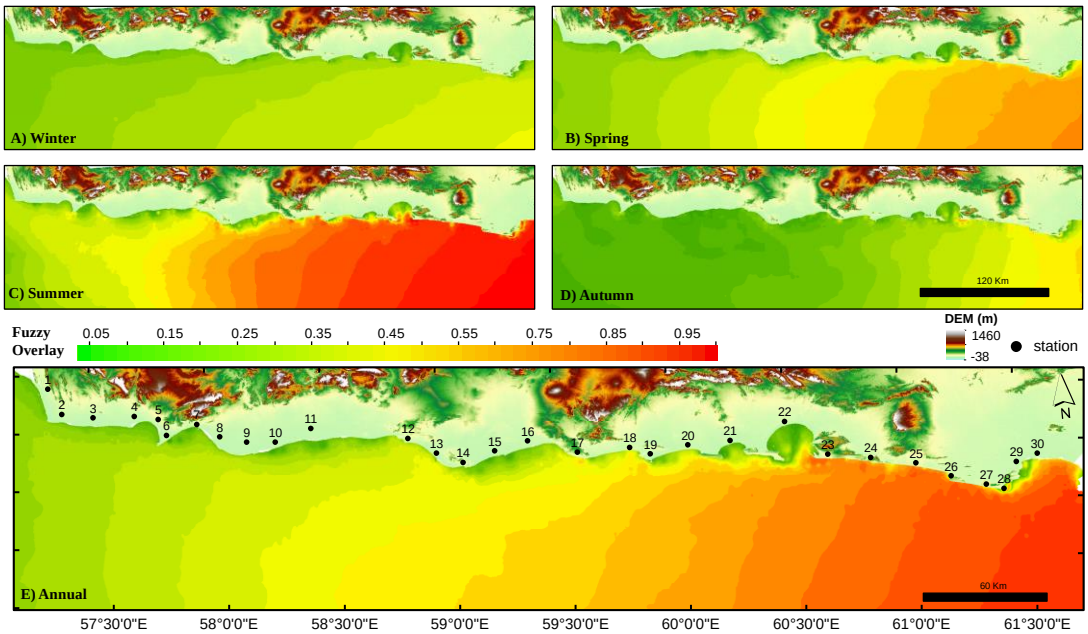


Figure 8. Overlaying outcomes of fuzzy layers (H_S, P, MWD) through the GAMMA method seasonally (A-D) and annually (E)

The seasonal and annual fluctuations of overlaying variables within a 1 km buffer from the shoreline are depicted in Fig. 9. The annual average overlaying variables score (black line in Fig. 9) reveals that zones Bunji-ye Karbasi (1) to Gougsar (12) exhibit scores below 0.4. Notably, from zone Kalirak (14) to Khowr Galak (16), intermediate zones Tang- Gurdim Bay (19-20), Gurdim Bay- Pozm Bay (20-21), zone Chabahar Bay (22), and zone Mangrove Gwadar (29) experience a discernible reduction attributed to the omega-shaped coast. Despite higher scores for the MWD variable in these regions, variables H_S and P register significantly lower scores (Fig. 9). Consequently, the overlayed variable indicate calm hydrodynamic conditions. In the western part, only a small segment of zones Lirak (13) and Kalāt (17) demonstrates overlaying variable scores surpassing 0.5. In these two areas, the wave enters with an oblique angle toward the shore (Fig. 6 C), resulting in a slight increase in the overall score of overlaying variables. In the eastern part, multiple regions exhibit annual average scores exceeding 0.5, such as zones Birdaf (18), Tang (19), Gurdim Bay (20), Pasabandar (28), and Khowr Bahokalat (30). Zones Birdaf, Gurdim Bay (20), and Khowr Bahokalat (30) represent open coastal areas, while zones Tang (19) and Pasabandar (29) constitute tombolo and capes, where waves with higher H_S and greater P exert influence. Between zones Chahbahar - Poshot (23-27), the overall score of annual average overlaying variables varies from 0.6 to 0.8. These coastal areas, characterized by highlands and rocky coasts, are fully exposed to oceanic conditions. Consequently, it is anticipated that the morphological response and coastal vulnerability in these regions to be significantly pronounced. In the study conducted by Siahsarani et al., [15], focusing on the investigation of the Gonu cyclone in the Gulf of Oman, it was articulated that a tropical cyclone has the potential to inflict damage,

both economic and environmental, to the coastal areas of Chabahar (the eastern zones in this study). Additionally, Ghaderi and Rahbani's [65] examination of the vulnerability of the eastern coast of Makran highlighted the susceptibility of these regions. These findings indicate that the high scores in eastern regions, influenced by oceanic conditions, may increase coastal vulnerability, highlighting the need for targeted management strategies to mitigate erosion and damage from extreme weather events.

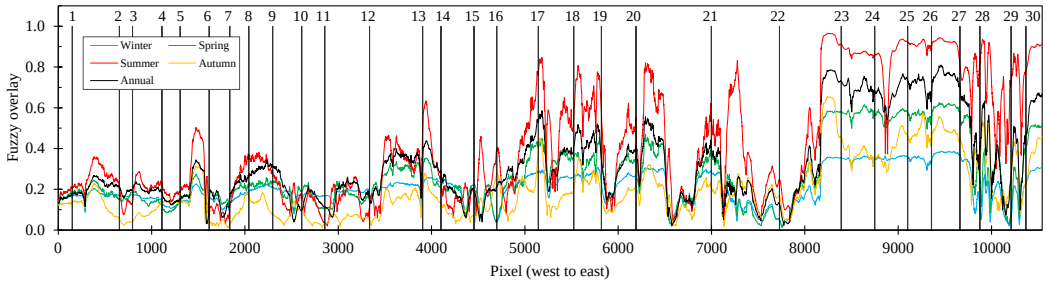


Figure 9. The results of overlaying fuzzy layers (H_S, P, MWD) using the GAMMA method, in a buffer of one km from Makran shore (The code for the indicator areas is provided at the top of the chart)

4. Conclusions

The primary objective of this study is to furnish detailed information on the wave patterns of the Makran coasts. Given the strategic importance of the Makran coasts for maritime development, a comprehensive understanding of their hydrodynamic conditions becomes essential. A numerical simulation was conducted to investigate the hydrodynamic conditions of the aera. The output results were utilized to analyze the seasonal and annual averages of wave height, wave power, and wave direction in the nearshore zone.For simultaneous analysis of variables, the data was subjected to Fuzzy Logic transformation using the fuzzy-GAMMA operator, and the values of all three variables were overlaid.

From a temporal perspective, the pattern of wave height and wave power can be categorized into three periods: winter and spring, characterized by minimal hydrodynamic conditions; summer, exhibiting maximum hydrodynamic conditions; and autumn, marking the onset of a decline in hydrodynamic conditions. The wave direction pattern in the nearshore zone falls into two periods: winter and spring, where the predominant wave direction is primarily south-southwest, and summer and autumn, where the waves are predominantly southern direction, besides the dispersion of directions within this timeframe is diverse. In terms of spatial variations, the hydrodynamic conditions are notably higher in the eastern section, particularly from the Kalāt zone to the Khowr Bahokalat zone, where both wave height and wave power are elevated, leading to increased coastal impact and erosion. Conversely, the western section generally exhibits lower hydrodynamic conditions, characterized by reduced wave height and wave power, resulting in less significant coastal effects. These variations are influenced by geographical features such as the coastline's orientation and bathymetric characteristics, which affect wave propagation and energy distribution. In the omega-shaped coast and bays, hydrodynamic conditions are generally minimal, except for the Gwadar Bay, which, due to its expansive entrance, experiences higher hydrodynamic conditions compared to other bays. The results of overlaying variable scores indicate that the hydrodynamic conditions in the coastal zone align with the analysis of temporal and spatial patterns of wave height and wave power. However, in certain locations such as

headlands, and capes, the hydrodynamic conditions have increased due to the oblique angle of waves in the nearshore zone.

Key findings include:

- **Wave Height (H_S):** Ranges from 0.07 to 1.9 m, peaking during summer with an average of 0.7 m. Winter and spring show calmer conditions with an average HS of 0.4 m. This parameter serves as an indicator of sea state and is crucial for understanding potential impacts on coastal infrastructure and erosion.
- **Wave Power (P):** Shows significant seasonal variation, with a marked increase in summer, reaching up to 10.2 kW/m, and an annual mean ranging from 0.02 to 5.3 kW/m. Increased wave power can lead to enhanced erosion and flooding risks, necessitating careful consideration in coastal development planning.
- **Wave Direction (MWD):** Exhibits seasonal variation, primarily ranging from 171° to 247° during winter and spring, and from 189° to 191° in summer and autumn. Waves approaching from the southern direction (180 degrees) exert minimal impact on the coastline, whereas oblique waves have a more pronounced effect, influencing coastal sediment transport and erosion patterns.

The findings of this study, along with similar studies, will assist planners and policymakers in developing management goals for coastal development. By integrating hydrodynamic dynamics into coastal planning, resilient strategies can be established for the sustainable utilization of the Makran region's resources, balancing maritime potential with risk mitigation.

Appendix

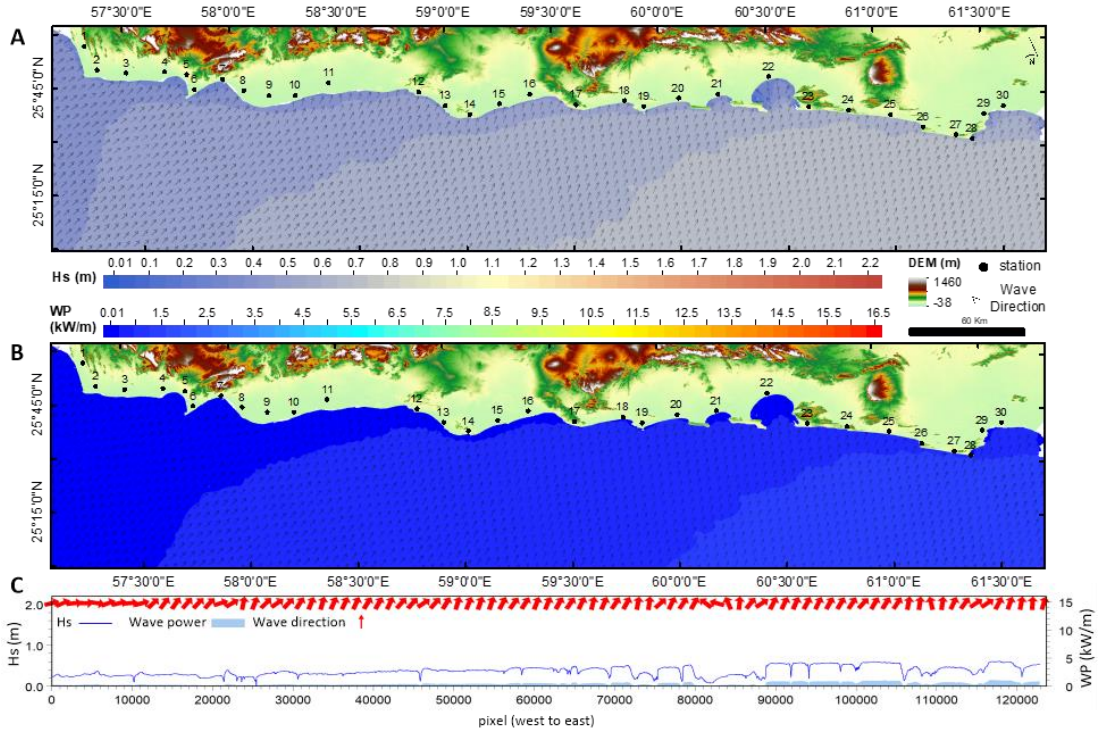


Figure A1: Winter season; Pattern of A) averaged significant wave height, B) averaged wave power, and C) spatial variation diagram extracted from variables in a 1 km buffer from the Makran shoreline

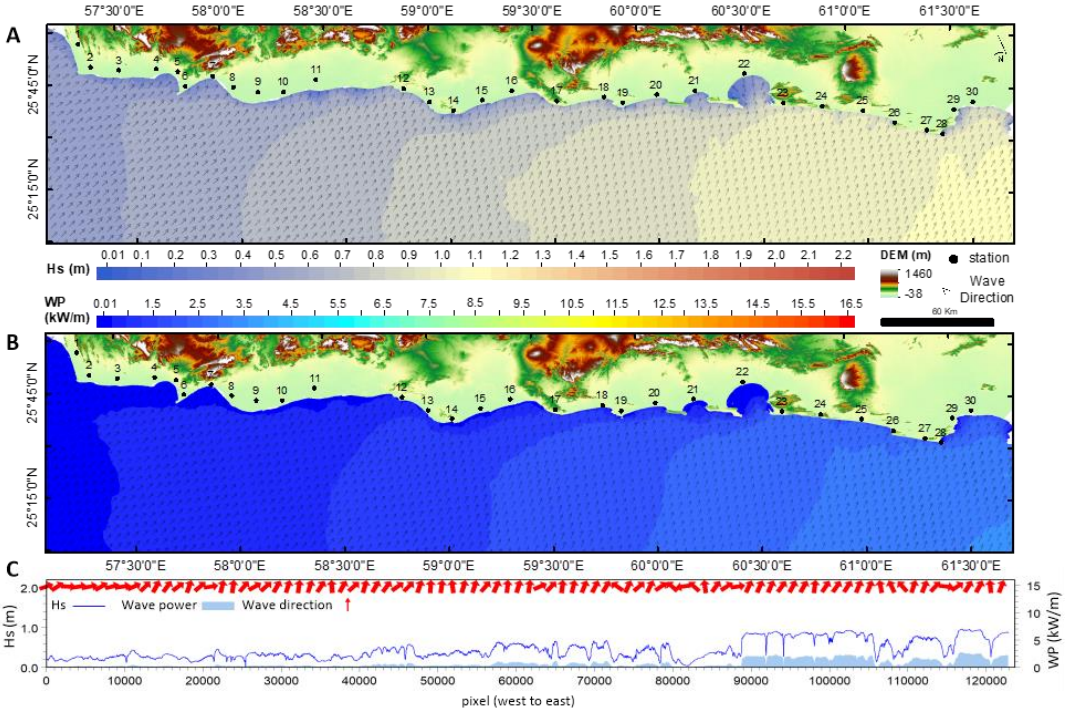


Figure A2: Spring season; Pattern of A) averaged significant wave height, B) averaged wave power, and C) spatial variation diagram extracted from variables in a 1 km buffer from the Makran shoreline

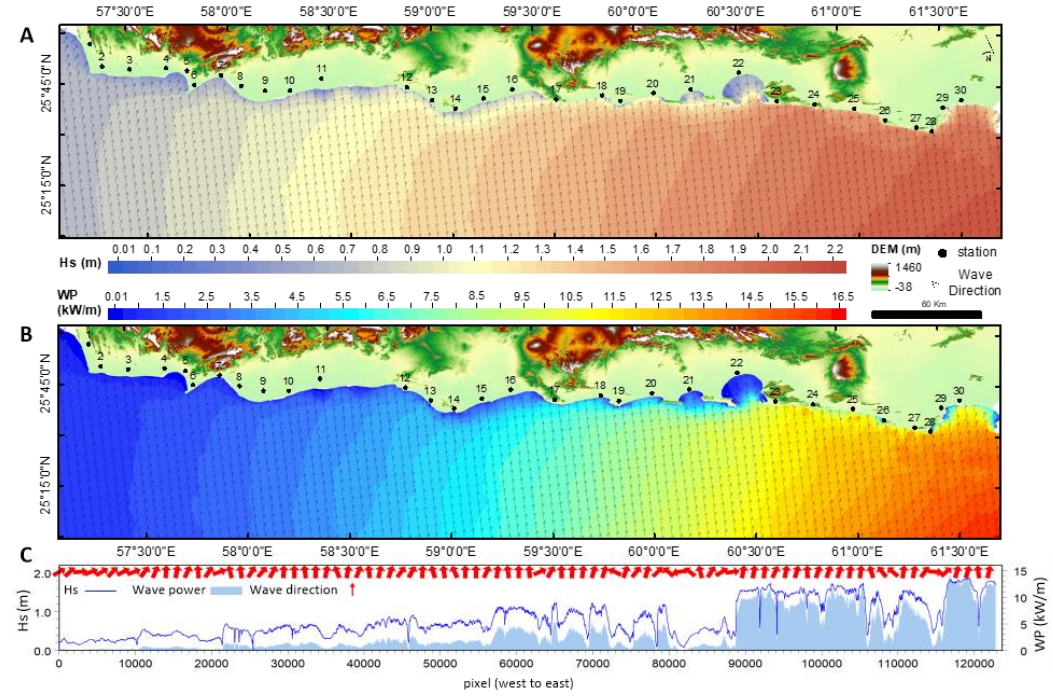


Figure A3: Summer season; Pattern of A) averaged significant wave height, B) averaged wave power, and C) spatial variation diagram extracted from variables in a 1 km buffer from the Makran shoreline

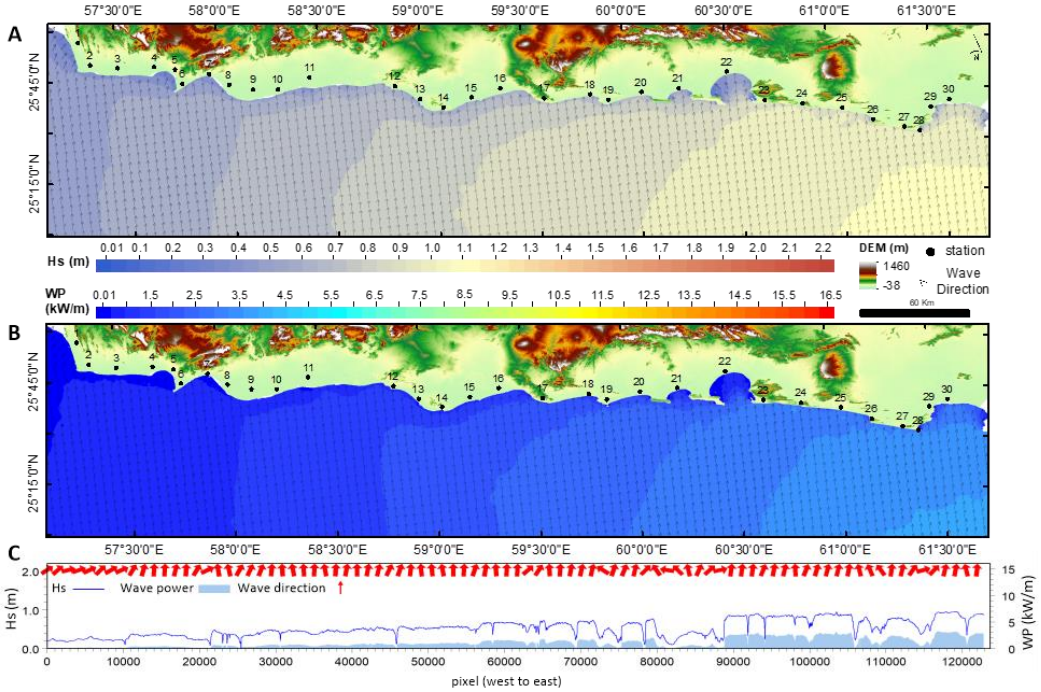


Figure A4: Autumn season; Pattern of A) averaged significant wave height, B) averaged wave power, and C) spatial variation diagram extracted from variables in a 1 km buffer from the Makran shoreline

References

1. United Nations. (2017). Factsheet: People and oceans. In Proceedings of the Ocean Conference (pp. 1–7).
2. Stewart, R. H., Introduction to physical oceanography, 2008.
3. Boye, C. B., Appeaning Addo, K., Wiafe, G., & Dzigbodi-Adjimah, K, (2018). Spatio-temporal analyses of shoreline change in the Western Region of Ghana. Journal of Coastal Conservation, 22(4), 769–776. DOI: 10.1007/s11852-018-0607-z
4. Church, J., Wilson, S., Woodworth, P., & Aarup, T, (2007). Understanding sea level rise and variability. Eos, Transactions American Geophysical Union, 88(4), 43–43. DOI: 10.1029/2007EO040008
5. Bird, E. C. F., Coastal geomorphology: an introduction. John Wiley Sons, 2008
6. Passeri, D. L., Hagen, S. C., Medeiros, S. C., Bilskie, M. V., Alizad, K., & Wang, D. (2015). The dynamic effects of sea level rise on low-gradient coastal landscapes: A review. Earth's Future, 3(6), 159–181. DOI: 10.1002/2015EF000298
7. Ye, X., & Niyogi, D, (2022). Resilience of human settlements to climate change needs the convergence of urban planning and urban climate science. Computational Urban Science, 2(1), 6. DOI: 10.1007/s43762-022-00035-0
8. Savastano S, Gomes da Silva P, Sánchez JM, Tort AG, Payo A, Pattle ME, Garcia-Mondéjar A, Castillo Y, Monteys X, (2024). Assessment of Shoreline Change from SAR Satellite Imagery in Three Tidally Controlled Coastal Environments. Journal of Marine Science and Engineering, 12(1), 163. DOI: 10.3390/jmse12010163.

9. Akbarian, M., & Khoorani, A, (2022). The impacts of climate variability on the wind erosion potentials: western region of Makran coastal plain, South of Iran. Theoretical and Applied Climatology, 149(3–4), 1209–1221. DOI:10.1007/s00704-022-04094-5
10. Allahdadi, M. N., Chaichitehrani, N., Allahyar, M., & McGee, L, (2017). Wave Spectral Patterns during a Historical Cyclone: A Numerical Model for Cyclone Gonu in the Northern Oman Sea. Open Journal of Fluid Dynamics, 07(02), 131–151. DOI:10.4236/ojfd.2017.72009
11. Moghaddam, E. I., Allahdadi, M. N., Hamedi, A., & Nasrollahi, A, (2018). Wave-induced currents in the northern Gulf of Oman: a numerical study for Ramin Port along the Iranian coast. American Journal of Fluid Dynamics, 8(1), 30–39. DOI:10.5923/j.ajfd.20180801.04
12. Sayehbani, M., Ghaderi, D, (2019). Numerical Modeling of Wave and Current Patterns of Beris Port in East of Chabahar-Iran. International Journal Of Coastal, Offshore And Environmental Engineering, 3(1), 21–29. DOI: 10.22034/ijcoe.2019.149314
13. Ghaderi, D., & Rahbani, M, (2023). Simultaneous employment of hydrodynamical simulation and RS imageries for analyzing the influence of an anthropogenic construction on shoreline transformation. Journal of Hydraulic Structures, 9(3), 14–31. DOI: 10.22055/jhs.2023.44699.1262
14. Armanfar, M., Goharnejad, H., Niri, M. Z., & Perrie, W, (2019). Assessment of coastal vulnerability in Chabahar Bay due to climate change scenarios. Oceanologia, 61(4), 412–426. DOI:10.1016/j.oceano.2019.03.001
15. Siahsarani, A., Karami Khaniki, A., Aliakbari Bidokhti, A.-A., & Azadi, M, (2021). Numerical Modeling of Tropical Cyclone-Induced Storm Surge in the Gulf of Oman Using a Storm Surge–Wave–Tide Coupled Model. Ocean Science Journal, 56(3), 225–240. DOI: 10.1007/s12601-021-00027-x
16. Foroutani, R., Rahbani, M., & Pakhirehzan, M, (2018). Investigating the Storm Surge Due to Tropical Cyclone Ashobaa in the Coastal Areas of Bushehr and Chabahar. Journal of Oceanography, 8(32), 9–19. DOI: 10.29252/joc.8.32.9
17. Ghanavati, E., Shah-Hosseini, M., Marriner, N. (2021). Analysis of the Makran Coastline of Iran's Vulnerability to Global Sea-Level Rise. Journal of Marine Science and Engineering, 9(8), 891. DOI: 10.3390/jmse9080891
18. Hafeznia M.R, Alamdar E., Rezaei Seke Ravani D, (2020). The Role of Developing the Makran Coast and Iran's Marine Orienteering Strategy on the Development of the Eastern Axis of the Country. Political Organizing of Space, 2(2).
19. Chaichitehrani, N., & Allahdadi, M. N. (2018). Overview of wind climatology for the Gulf of Oman and the northern Arabian Sea. American Journal of Fluid Dynamics, 8(1), 1–9. DOI: 10.5923/j.ajfd.20180801.01
20. Pous, S. P., Carton, X., & Lazure, P, (2004). Hydrology and circulation in the Strait of Hormuz and the Gulf of Oman—Results from the GOGP99 Experiment: 2. Gulf of Oman. Journal of Geophysical Research: Oceans, 109(C12). DOI: 10.1029/2003JC002146
21. Rashidi, A., Dutykh, D., Shomali, Z. H., Keshavarz Farajkhah, N., & Nouri, M. (2020). A Review of Tsunami Hazards in the Makran Subduction Zone. Geosciences, 10(9), 372. DOI: 10.3390/geosciences10090372

22. Salah, P., Sasaki, J., & Soltanpour, M, (2021). Comprehensive Probabilistic Tsunami Hazard Assessment in the Makran Subduction Zone. Pure and Applied Geophysics, 178(12), 5085–5107. DOI: 10.1007/s00024-021-02725-y
23. Pourkerman, M., Marriner, N., Hamzeh, M.-A., Lahijani, H., Morhange, C., Amjadi, S., et al. (2022). Socioeconomic impacts of environmental risks in the western Makran zone (Chabahar, Iran). Natural Hazards, 112(2), 1823–1849. DOI: 10.1007/s11069-022-05230-0
24. He, W., Liu, J., Huang, Y., & Cao, L, (2020). Sea Level Change Controlled the Sedimentary Processes at the Makran Continental Margin Over the Past 13,000 yr. Journal of Geophysical Research: Oceans, 125(3). DOI: 10.1029/2019JC015703
25. Group-DHI. (2017). MIKE 21 Spectral Wave Module, Scientific Documentation. Hørsholm, Denmark: DHI Water Environment Health.
26. Komen, G. J., Cavaleri, L., Donelan, M., Hasselmann, K., Hasselmann, S., & Janssen, P, Dynamics and modelling of ocean waves, 1996. DOI: 10.1017/CBO9780511628955
27. Tolman HL. (2009). User manual and system documentation of WAVEWATCH III TM version 3.14. Technical note, MMAB contribution.;276(220).
28. Delft, T. (2014). SWAN User Manual Cycle III version 41.01. Delft, Nederlands: Delft University of Technology Faculty of Civil Engineering and Geosciences Environmental Fluid Mechanics Section.
29. TOMAWAC. (2014). TOMAWAC wave model.
30. Moore, AM., Arango, HG., Broquet, G., Edwards, C., Veneziani, M., Powell, B., et al. (2011). The Regional Ocean Modeling System (ROMS) 4-dimensional variational data assimilation systems. Progress in Oceanography. 91(1):50–73. DOI: 10.1016/j.pocean.2011.05.004
31. Pakhirehzan, M., Rahbani, M., & Malakooti, H. (2018). Numerical Study of Winter Shamal Wind Forcing on the Surface Current and Wave Field in Bushehr's Offshore Using MIKE21. International Journal of coastal and offshore engineering, 2(2), 57–65. DOI: 10.29252/ijcoe.2.2.57
32. Wu, C., Wan, J., Wang, Y., Bi, Z., Wang, Y., Ren, X. (2024). Evaluation of water quality fluctuation in the tidal reach under the impact of on shore wastewater discharges based on MIKE 21 model in Dongguan, China. Physics and Chemistry of the Earth, Parts A/B/C. 103730. DOI: 10.1016/j.pce.2024.103730
33. Upadhyaya, S., Rao, S., Rao, M. (2024). Assessment of wind and wave energy potential along the Indian coast. Cogent Engineering. 31;11(1). DOI: 10.1080/23311916.2024.2316950
34. Djili, M., Mezouar, K., Benaissa, N. (2024). Wave Climate, Sediment Transport and Shoreline Evolution in the West Littoral of Algeria. Ocean Science Journal. 28;59(3):39. DOI: 10.1007/s12601-024-00165-y
35. Ghaderi, D. (2024). Mapping the shoreline risk assessment of oil spill in the eastern region of Qeshm channel. Marine Pollution Bulletin. 206:116714. DOI: 10.1016/j.marpolbul.2024.116714
36. Remya, P. G., Kumar, R., & Basu, S. (2014). An assessment of wind forcing impact on a spectral wave model for the Indian Ocean. Journal of Earth System Science, 123(5), 1075–1087. DOI: 10.1007/s12040-014-0450-z

37. Jadidoleslam, N., Özger, M., & Ağıralioğlu, N, (2016). Wave power potential assessment of Aegean Sea with an integrated 15-year data. Renewable Energy, 86, 1045–1059. DOI: 10.1016/j.renene.2015.09.022
38. Abdollahzadehmoradi, Y., Özger, M., & Altunkaynak, A, (2018). Long-Term Macro-Scale Assessment of Wave Power of Black Sea by an Optimized Numerical Model. Iranian Journal of Science and Technology, Transactions of Civil Engineering, 42(4), 391–414. DOI: 10.1007/s40996-018-0108-1
39. Uppala, S. M., KÅllberg, P. W., Simmons, A. J., Andrae, U., Bechtold, V. D. C., Fiorino, M., et al. (2005). The ERA-40 re-analysis. Quarterly Journal of the Royal Meteorological Society, 131(612), 2961–3012. DOI: 10.1256/qj.04.176
40. Anton, I. A., Rusu, L., Anton, C., Anton, Rusu, & Anton, (2019). Nearshore wave dynamics at Mangalia beach simulated by spectral models. Journal of Marine Science and Engineering, 7(7), 206. DOI:10.3390/jmse7070206
41. Mahmoodi, A., Lashteh Neshaei, M. A., Mansouri, A., & Shafai Bejestan, M, (2020). Study of Current- and Wave-Induced Sediment Transport in the Nowshahr Port Entrance Channel by Using Numerical Modeling and Field Measurements. Journal of Marine Science and Engineering, 8(4), 284. DOI: 10.3390/jmse8040284
42. Kalra, R., & Deo, M. C. (2007). Derivation of coastal wind and wave parameters from offshore measurements of TOPEX satellite using ANN. Coastal Engineering, 54(3), 187–196. DOI: 10.1016/j.coastaleng.2006.07.001
43. Cox, A. T., & Swail, V. R. (2001). A global wave hindcast over the period 1958--1997: Validation and climate assessment. Journal of Geophysical Research, 106(C2), 2313–2329. DOI: 10.1029/2001JC000301
44. Mahjoobi, J., Etemad-Shahidi, A., & Kazeminezhad, M. H, (2008). Hindcasting of wave parameters using different soft computing methods. Applied Ocean Research, 30(1), 28–36. DOI: 10.1016/j.apor.2008.03.002
45. Rusu, E. (2018). An analysis of the storm dynamics in the Black Sea. The Romanian Journal of Technical Sciences. Applied Mechanics, 63, 131–146.
46. Dávila-Lamas, AD., Carbajal-Hernández, JJ., Sánchez-Fernández, LP., Niebla-Zatarain, VB., Hoil-Rosas, CA. (2022). Assessment of Coastal Locations Safety Using a Fuzzy Analytical Hierarchy Process-Based Model. Sustainability. 14;14(10):5972. DOI: 10.3390/su14105972
47. Zadeh, L. A. (1996). FUZZY SETS (pp. 394–432). DOI: 10.1142/9789814261302_0021
48. Tabrizi, N., Taghvaei, M., & Varesi, H. R, (2012). A fuzzy application on MICE hosting: An Iranian case study for locating suitable areas based on P.L Indexes. Management Science Letters, 2(2), 503–510. DOI: 10.5267/j.msl.2011.12.024
49. Ghadamode, V., Srivastava, K., Singh, R. K., & Pandey, A. K, (2022). Spatial analysis techniques for tsunami vulnerability and inundation mapping of Andaman region using remote sensing, GIS, AHP, and Fuzzy logic methods. Environmental Earth Sciences, 81(17), 427. DOI: 10.1007/s12665-022-10548-w

50. Lee, S. (2007). Application and verification of fuzzy algebraic operators to landslide susceptibility mapping. Environmental Geology, 52(4), 615–623. DOI: 10.1007/s00254-006-0491-y
51. Obakrim, S., Ailliot, P., Monbet, V., & Raillard, N, (2023). Statistical modeling of the space–time relation between wind and significant wave height. Advances in Statistical Climatology, Meteorology and Oceanography, 9(1), 67–81. DOI: 10.5194/ascmo-9-67-2023
52. Falnes, J, (2007). A review of wave-energy extraction. Marine Structures, 20(4), 185–201. DOI: 10.1016/j.marstruc.2007.09.001
53. Ozkan, C., Perez, K., & Mayo, T. (2020). The impacts of wave energy conversion on coastal morphodynamics. Science of The Total Environment, 712, 136424. DOI: 10.1016/j.scitotenv.2019.136424
54. Ozkan, C., Mayo, T., & Passeri, D. L, (2022). The Potential of Wave Energy Conversion to Mitigate Coastal Erosion from Hurricanes. Journal of Marine Science and Engineering, 10(, 143. DOI: 10.3390/jmse10020143
55. Chaigneau, A. A., Law-Chune, S., Melet, A., Voldoire, A., Reffray, G., & Aouf, L, (2023). Impact of sea level changes on future wave conditions along the coasts of western Europe. Ocean Science, 19(4), 1123–1143. DOI: 10.5194/os-19-1123-2023
56. Falqués, A., Calvete, D., & Ribas, F, (2011). Shoreline Instability due to Very Oblique Wave Incidence: Some Remarks on the Physics. Journal of Coastal Research, 27(2), 291. DOI: 10.2112/JCOASTRES-D-09-00095.1
57. Ashton, A. D., & Murray, A. B, (2006). High-angle wave instability and emergent shoreline shapes: 2. Wave climate analysis and comparisons to nature. Journal of Geophysical Research: Earth Surface, 111(F4). DOI: 10.1029/2005JF000423
58. Bonham-Carter, G, Geographic information systems for geoscientists: modelling with GIS. Elsevier, 1994. DOI: 10.1016/C2013-0-03864-9
59. Moradpanah, M., Monavari, S. M., Shariat, S. M., Khan Mohammadi, M., & Ghajar, I, (2022). Evaluation of Ecological Vulnerability of Coasts of the Caspian Sea Based on Multi-criteria Decision Methods (Iran). Journal of the Indian Society of Remote Sensing, 50(12), 2479–2502. DOI: 10.1007/s12524-022-01612-w
60. Vafai, F., Hadipour, V., & Hadipour, A, (2013). Determination of shoreline sensitivity to oil spills by use of GIS and fuzzy model. Case study – The coastal areas of Caspian Sea in north of Iran. Ocean & Coastal Management, 71, 123–130. DOI: 10.1016/j.ocecoaman.2012.05.033
61. Sadeghi, B., & Khalajmasoumi, M. (2015). A futuristic review for evaluation of geothermal potentials using fuzzy logic and binary index overlay in GIS environment. Renewable and Sustainable Energy Reviews, 43, 818–831. DOI: 10.1016/j.rser.2014.11.079
62. Saket, A., Etemad-Shahidi, A, (2012). Wave energy potential along the northern coasts of the Gulf of Oman, Iran. Renewable Energy, 40(1), 90–97. DOI: 10.1016/j.renene.2011.09.024
63. Srinivas, G., Remya, PG., Malavika, S., Nair TMB. (2020). The influence of boreal summer intra-seasonal oscillations on Indo-western Pacific Ocean surface waves. Scientific Reports. 28;10(1):12631. DOI: 10.1038/s41598-020-69496-9

64. Chitrakar, P., Baawain, M. S., Sana, A., & Al-Mamun, A, (2020). Hydrodynamic measurements and modeling in the coastal regions of Northern Oman. Journal of Ocean Engineering and Marine Energy, 6(2), 99–119. DOI: 10.1007/s40722-020-00161-z
65. Ghaderi, D., & Rahbani, M, (2024). Evaluating the shoreline vulnerability of eastern coast of Makran employing geomorphological and hydrodynamic parameters. Journal of Earth System Science, 133(2), 48. DOI: 10.1007/s12040-024-02266-7

© 2025 by the authors. Licensee SCU, Ahvaz, Iran. This article is an open access article distributed under the terms and conditions of the Creative Commons Attribution 4.0 International (CC BY 4.0 license) (http://creativecommons.org/licenses/by/4.0/).

Journal of Hydraulic Structures

Volume 11 – Issue 1 – January 2025

Contents:

01 Optimizing the urban runoff collecting network using Harris Hawks single-objective optimization algorithm (a case study of the flood network in West Tehran)

Seyed Masoud Majidi; Hamed Reza Zarif Sanayei; Ali Raeisi Isa-Abadi

20 Enhancing the seismic performance of platforms in intermediate water depth using shape memory alloy dampers

Mohammad Jafari; Hamid Bayesteh; Reza Rasti Ardakani

41 Spiral Flow Measurement at Vertical Intakes Using PTV Method

ShahWali Hamidi; Hamed Sarkardeh; Ali Bashtani

51 Dimensionless Equations for Hydraulic Jump Stilling Basins Downstream of Gabion Stepped Chutes

André Luiz Andrade Simões; Thaise Ithana de Souza França; Luciano Matos Queiroz; Iran Eduardo Lima Neto; Harry Edmar Schulz; Daniel Castro Hora Fontes; Rodrigo de Melo Porto

65 Numerical Study of Permanent Deformations of Embankment dams under Seismic Loading, A case study of Kheyrabad Dam

Masoud Oulapour; Hossein Samani; Mohammad Amjadzadeh

89 Integrating Fuzzy Logic and Numerical Modeling for Analyzing Wave Patterns: A Study of the Makran Coastline

Maryam Rahbani; Danial Ghaderi

Shahid Chamran University of Ahvaz